UNIVERSITY OF OKLAHOMA

GRADUATE COLLEGE

NON-LOCAL THERMODYNAMIC EQUILIBRIUM SPECTRUM SYNTHESIS OF TYPE Ia SUPERNOVAE

A DISSERTATION

SUBMITTED TO THE GRADUATE FACULTY

in partial fulfillment of the requirements for the

degree of

DOCTOR OF PHILOSOPHY

By

PETER E. NUGENT
Norman, Oklahoma
1997

NON-LOCAL THERMODYNAMIC EQUILIBRIUM SPECTRUM SYNTHESIS OF TYPE Ia SUPERNOVAE

A DISSERTATION APPROVED FOR THE DEPARTMENT OF PHYSICS AND ASTRONOMY

BY

Edward Baron (Chair)

David Branch

John Cowan

William Romanishin

Susan Postawko

Acknowledgements

I have many people to thank for getting me to where I am today. Without their help this dissertation would have never been realized. First on the list are my parents, who showed me the importance of an education (though I don't think they had 24 years in mind when they sent me off to kindergarten) and gave me the freedom to pursue whatever I wanted to in school. I also want to thank my brother James for being there for me.

I wish to thank my grandfather for giving me my first lessons in electricity and magnetism. My curiosity in physics started in his basement workshop sifting through resistors and capacitors and playing with the oscilloscope. He also gave me my first telescope, something which started off as a hobby and led to my chosen profession of astronomy.

I thank Professors Thomas Bross and E.O. LaCasce. They saw me through high school and college physics respectively. The skills they taught me and the work ethic they instilled in me has served me well the past seven years of graduate school and will continue to do so for many years to come.

I thank Ed Baron and David Branch for introducing me to supernovae and advising me throughout graduate school. Their teaching, patience, generosity and friendship has been greatly appreciated. I look forward to many future collaborations.

Finally I wish to thank the two most important people in my life. Anya, whose cute little smile when I come home from a hard day at work makes it all worthwhile, and Deepa, whose unfailing love and encouragement these past seven years has meant everything to me. I wouldn't have made it this far without you.

Contents

List of Tables

List of Figures

Chapter 1

Introduction

1.1 NLTE Spectrum Synthesis and SNe Ia

It is perhaps fitting, but more likely absolutely necessary, to start off this thesis with a definition of the title – NLTE spectrum synthesis of Type Ia supernovae. NLTE stands for non-local thermodynamic equilibrium. It represents a step up from LTE by accurately solving the rate equations to determine the level populations for a selected set of ionic species. Non-local means that it incorporates effects beyond just that of the the local electron temperature in order to determine the level populations. Given a finite piece of the atmosphere, these effects include both non-thermal ionization due to the local γ-ray deposition and the effects of the impinging radiation field. Spectrum synthesis, in broad terms, is the numerical calculation of a spectrum given a particular model for an atmosphere. A model includes such information as abundances, radial, velocity and density gradients and the overall luminosity of the object. Type Ia supernovae (SNe Ia) are are among the brightest known objects in the universe. They form a nearly homogeneous class and given a simple selection criterion the observed dispersion in their overall luminosity is quite small. They occur in both spirals and ellipticals and the current prevailing wisdom is that they are the explosion of a Chandrasekhar-mass white dwarf. The classification of 'Ia' is a spectral one, based on the absence of hydrogen in the spectra and a prominent Si II feature near 6000Å.

SNe Ia can be thought of as one of the fundamental building blocks in astronomy. The elements they eject are are important for nucleosynthesis studies as they provide a large fraction of a galaxy's metals. In addition, they are valuable distance indicators for cosmology yielding some of the best measurements of both the Hubble constant and the deceleration parameter. The modeling of their atmospheres and spectra provides us with three tools to further our understanding of SNe Ia. First, in comparing synthetic and observed spectra, we are able to ascertain information on the temperature, density, velocity, and composition of the ejected matter. Second, by calculating the spectra of hydrodynamical models of SNe Ia, we are able to constrain both explosion mechanisms and progenitor types. Third, incorporating the spectral fitting expanding atmosphere method (SEAM) one can measure the luminosity of a SN Ia, yielding distances to individual events that are independent of distances based on the decay of ^{56}Ni in SNe Ia and of Cepheid variable stars in the parent galaxies.

This thesis is broken down into 4 major sections, each highlighting a different way with which to use spectrum synthesis to analyze SNe Ia. Chapters 2 and 3 look at normal SNe Ia and their potential use as distance indicators using SEAM. Chapter 4 examines spectral correlations with luminosity in SNe Ia and provides a plausible explanation for these correlations via spectrum synthesis. In Chapter 5 the spectra of various hydrodynamical models are calculated in an effort to answer the question of which current progenitor/explosion model is the most plausible for a SN Ia. Finally, we look at the importance of NLTE calculations and line identifications in Chapter 6. Also included are two appendices which contain more technical information concerning γ-ray deposition and the thermalization parameter.

1.2 Phoenix

All of the spectrum synthesis calculations shown in this thesis use the code PHOENIX to calculate the model atmospheres. The work compiled for this thesis was stretched out over a three year period. During this time PHOENIX has gone through several revisions. PHOENIX 4.8 was used for the work in Chapters 1-4 and in Chapters 5 and 6 PHOENIX 7.1 was incorporated. The following is a general description of the code and the differences between the two versions mentioned above.

PHOENIX 7.1 (Hauschildt, 1992a,b, 1993; Hauschildt, Baron, & Allard, 1996) is a generalized stellar atmosphere code which has been used successfully to produce spectra for novae, all types of SNe, red giants, cool stars and even AGNs. The code accurately solves the fully relativistic radiation transport equation along with the non-LTE rate equations while ensuring radiative equilibrium (energy conservation) (Baron et al., 1995; Hauschildt et al., 1995, 1996). The following ions have been treated in NLTE for type Ia supernovae calculations (the number of levels follows in parenthesis): He I (11), He II (10), Na I (3), Ne I (26), Ca II (87), Mg II (18), C I (228), O I (36), Fe II (617), Co II (255), Ti II (204), S II (85) and Si II (94). In addition, the code is now able to handle the treatment of nebular boundary conditions, as well as a stratified composition and a full γ-ray deposition calculation. This is the major difference between this version and version 4.8 along with putting the iron peak and CNO elements into NLTE.

Chapter 2

SNe Ia 1992A and 1981B

2.1 Abstract

We present NLTE synthetic spectra for the Type Ia supernovae SN 1992A and SN 1981B, near maximum light. At this epoch both supernovae were observed from the UV through the optical. This wide spectral coverage is essential for determining the density structure of a SN Ia. Our fits are in good agreement with observation and provide some insight as to the differences between these supernovae. We also discuss the application of the expanding photosphere method to SNe Ia which gives a distance that is independent of those based on the decay of ^{56}Ni and Cepheid variable stars.

2.2 Introduction

Type Ia supernovae (SNe Ia) are valuable distance indicators for cosmology and the elements they eject are are important for nucleosynthesis. They appear to be thermonuclear disruptions of carbon–oxygen white dwarfs that accrete from companion stars until they approach the Chandrasekhar mass, and there is a suspicion that the propagation of the nuclear burning front involves a transition from a deflagration to a detonation. (For a review of these issues see Branch & Khokhlov (1995, in press). Detailed modeling of the atmospheres and spectra of SNe Ia is needed to advance our understanding of SNe Ia. Comparison of synthetic and observed spectra provides information on the temperature, density, velocity, and composition of the ejected matter and thus constrain hydrodynamical models. In addition, the expanding photosphere method yields distances to individual events that are independent of distances based on the decay of ^{56}Ni in SNe Ia and of Cepheid variable stars in the parent galaxies.

2.3 Description of the Models

We use the computer code `PHOENIX 4.8` to compute our model atmospheres and synthetic spectra for SNe 1992A and 1981B (Hauschildt, 1993, 1992b,a). This code uses an accelerated Λ-iteration (ALI or operator splitting) method to solve the time independent, spherically symmetric, fully relativistic radiative transfer equation for lines and continua to all orders in v/c including the effects of relativistic Doppler shift, advection and aberration. The multi-level NLTE rate equations are solved self-consistently for Ca II, Mg II and Na I using an ALI method. Simultaneously we solve for the special relativistic condition of radiative equilibrium in the Lagrangian frame using a modified Unsöld-Lucy temperature correction scheme. Line transfer, including line blocking, is treated accurately.

The generalized NLTE equation of state (EOS) is solved for 40 elements and up to 6 ionization stages per element. The numerical solution of the EOS is based on Brent's method for the solution of non-linear equations which is very robust and fast (Brent, 1973). In addition to the NLTE lines, the models include, self consistently, line blanketing of the metal lines selected from the latest atomic and ionic line list of Kurucz (1993, CDROM No. 1 Atomic Data for Opacity Calculations, unpublished).

The continuous absorption and scattering coefficients are calculated using the cross sections as described by Hauschildt et al. (1992) and the thermalization parameter, α, is calculated according to the results of Appendix 2.

The effects of non-thermal collisional ionization by primary and secondary electrons produced by collisions with γ-rays due to the decay of ^{56}Ni and ^{56}Co are modeled using the continuous slowing down approximation (Swartz, 1991; Garvey & Green, 1976).

2.4 Comparison to Other Work

Past and present methods for computing synthetic spectra of SNe Ia near maximum light can be categorized by the physics used to treat the following : (1) atomic level populations, (2) continuum transfer and (3) radioactive decay of ^{56}Ni.

The simple models of Branch et al. (1985) and Kirshner et al. (1993) incorporate neither continuum transfer nor γ-ray deposition. The level populations for their models are parameterized and the ratio of the upper to lower level is governed by the assumption of resonance scattering. The advantage of these codes is that they require small amounts of CPU time while still producing very useful line identifications as well as providing information about ejection velocities and the composition of the supernova.

The Monte Carlo method of Mazzali & Lucy (1993) for the synthesis of early time SNe Ia spectra is based on a Schuster-Schwarzschild approximation. Their model has a sharp photosphere above which continuum transfer is neglected. The temperature structure is determined by assuming radiative equilibrium and the level occupation numbers are obtained through a modified version of the nebular approximation, neglecting the effects of the fast electrons produced by the decay of ^{56}Ni. Their code produces reasonable fits in the optical in a small amount of time while taking rough account of departures from LTE.

Branch et al. (1991) presented a full NLTE calculation of an SN Ia atmosphere. The synthetic spectrum produced in this paper was crude (none of the parameters were fine tuned for fitting purposes), but the overall agreement is not bad. More recent work by Miller et al. (1995, in preparation) has shown major improvements in the fits. The strength of these calculations is that they are based on a vast amount of atomic data and all species are treated in NLTE, however, they are non-physical in several ways. The radiative transfer is not calculated self-consistently and the continuum transfer assumes a static atmosphere in order to solve the rate equations. Line blocking is treated with a heuristic approximation and line transfer is accomplished assuming the Sobolev approximation. Energy conservation is not enforced and the change in the electron density due to the decay of ^{56}Ni is neglected. Finally, these calculations require a prohibitive amount of computer time.

Another recent NLTE calculation has been carried out by Höflich (1995). His focus is on the comparison of light curves and spectra of detailed hydrodynamic explosion models with observation. The synthetic spectra produced by his code are not adjusted by changing parameters such as the velocity at the photosphere or the temperature and density gradients, but rather are the results of a hydrodynamic calculation. The advantage of this type of calculation is that one can directly compare, through spectra and light curves, one hydrodynamic model to another. The disadvantages are that the fits rarely reproduce the correct strength or velocity placement of the observed lines, although good fits have been produced for SNe II (Hauschildt & Ensman, 1994). In contrast to our models much of the line transfer is performed assuming the Sobolev approximation and line blocking is approximated by a "quasi continuum" opacity. The relativistic terms in the radiative transfer equation are treated approximately and the thermalization parameter, α for each line considered in LTE is calibrated by a global fit to that produced by the ions treated in NLTE.

The calculations of Wheeler, Swartz, & Harkness (1993) are the most similar to ours in terms of the physics incorporated in the model atmosphere. Their calculations include both continuum transfer and the effects of ^{56}Ni decay. The major difference is that all of their atoms are treated in LTE whereas we include a number of important atoms in NLTE.

2.5 Model Parameters

The model atmospheres are characterized by the following parameters (Hauschildt et al., 1994; Baron, Hauschildt, & Branch, 1994; Baron et al., 1995; Allard et al., 1994): (1) the reference radius R_o, which is the radius where the continuum optical depth in extinction at 5000Å is unity, (2) the effective temperature $T_{\rm eff}$, which is defined by means of the co-moving luminosity, L, and R_o ($T_{\rm eff}^4 = L/4\pi R_o^2\sigma$), (3) the expansion velocity, v_o, at the reference radius, (4) the density, ρ_{out}, at the outer edge of the envelope, (5) the e-folding velocity, v_e, which defines the density by $\rho(r) = \rho_o e^{-v/v_e}$, or the power law index, N, which defines the density by $\rho(r) = \rho_o r^{-N}$, (6) the continuum thermalization parameter α, (7) a non-thermal ionization deposition function, (8) the element abundances. In all of our models of SNe Ia atmospheres the abundances were taken from the carbon deflagration model W7 (Nomoto, Thielemann, & Yokoi, 1984). To obtain our model abundances we homogenized the the zones in W7 with velocities greater than 8000 km s^{-1}. The value of α was assumed to be 0.1, the rise time, t_r, was taken to be 17 days (i.e. the reference radius at maximum light is $R_o^{\rm ML} = v_o\, t_r$), and the deposition function was local.

We ensured that our choice of outer density had no effect on the models, decreasing its value by an order of magnitude had no effect on the resultant spectrum.

2.6 Results

Figure 2.1 shows a comparison of SN 1992A, at 5 days after maximum light, with our best fit synthetic spectrum. The fit is a very reasonable one. It nicely follows the strong Fe peak line blanketing in the UV, the red edge of the Ca II H+K lines near 4000Å, the Mg II and Fe II troughs at 4500Å and 5000Å and the S II "W" between 5200Å and 5400Å. The noticeable discrepancies occur with the two Si II features at 3900Å and 5900Å and the O I feature at 7500Å. We believe that these features are due to NLTE effects and that the fit will improve once these species are calculated in NLTE. Included in this figure is a LTE synthetic spectrum to illustrate the importance of NLTE for our models.

Figure 2.2 shows our fit to SN 1981B at maximum light. Once again the overall fit is good, although there are still the discrepancies with the O I and Si II features. The advantage of fitting this observed spectrum is that it goes far enough into the red to show the Ca II infrared triplet near 8400Å. This feature really helps in the determination of the structure of the supernova. Unlike some of the other LTE features, the Ca II infrared triplet, which is treated in NLTE, is sensitive in different ways to changes in the velocity, temperature and density gradients. This makes it an invaluable part of the spectrum to have in order to obtain a good and meaningful fit. This is in contradistinction to atmospheres of SNe II, which are dominated by hydrogen, where the infrared triplet is rather insensitive to such changes.

Since SN 1992A was observed by both the HST, in the UV, and by CTIO, in the optical, with good signal to noise, we were able to constrain our models using

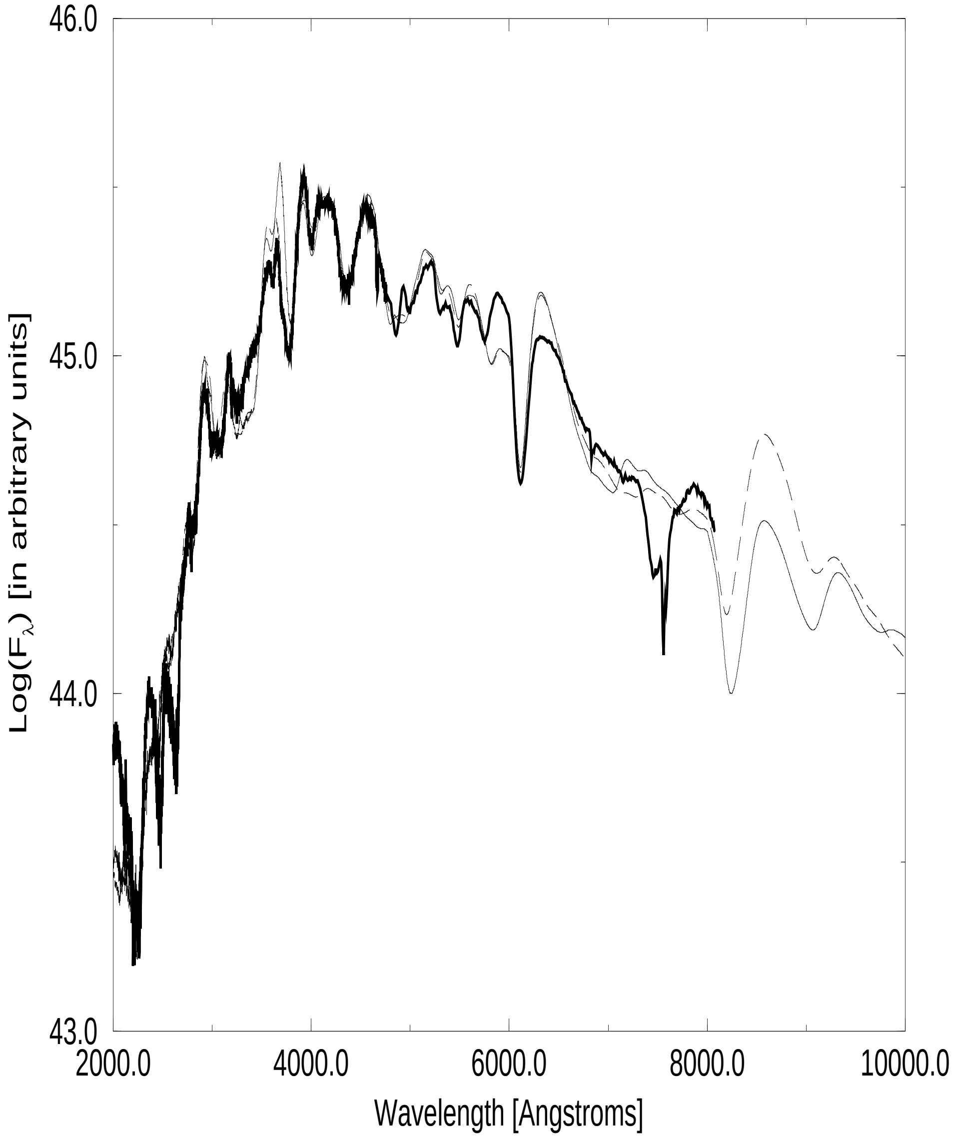

Figure 2.1: NLTE synthetic spectrum, thin line, LTE synthetic spectrum, dashed line, vs. the spectrum of SN 1992A, thick line, at 5 days after maximum blue light (Kirshner et al., 1993). While the LTE spectrum fits the Ca II H+K feature well the IR triplet absorption is weak and the emission is strong, in contrast to SN 1981B at a similar time. The NLTE H+K absorption feature appears too narrow, however, we believe that the observed width is produced by NLTE Si II.

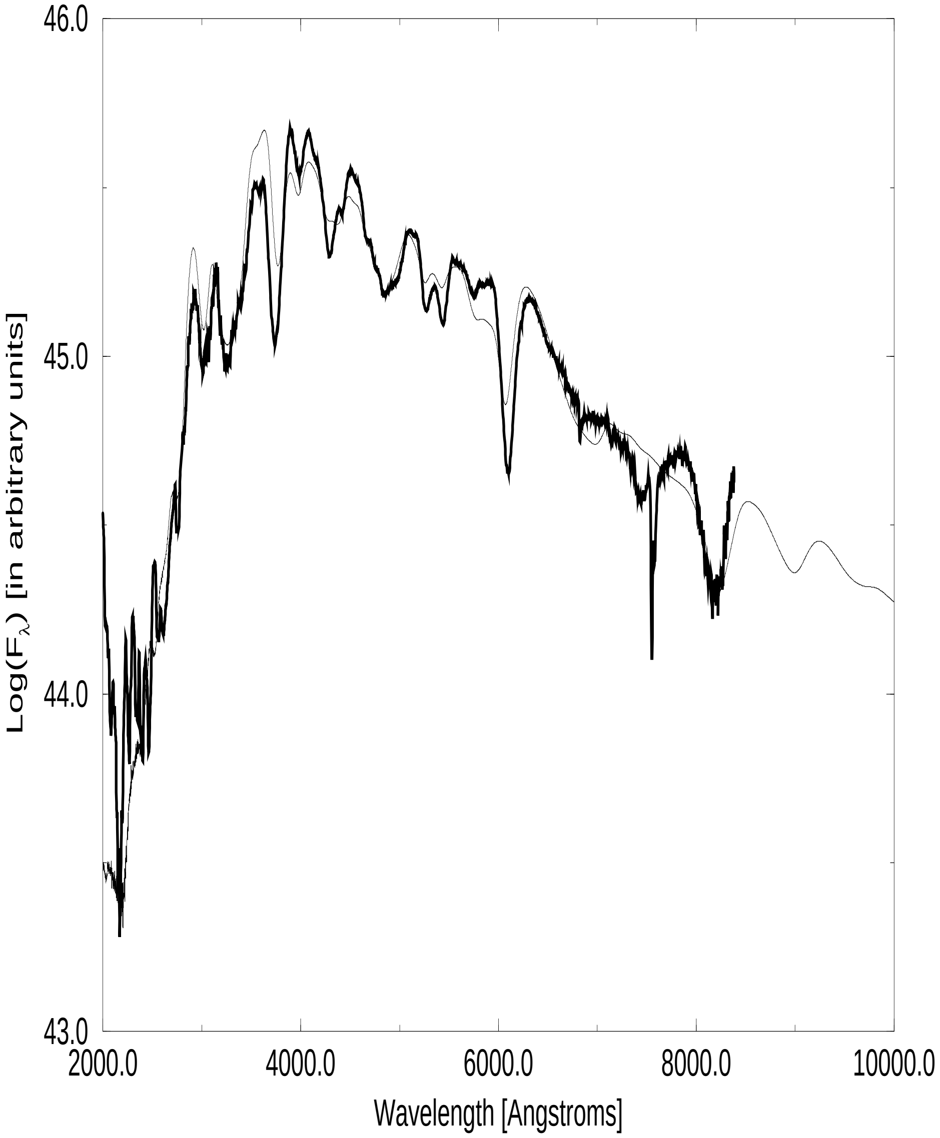

Figure 2.2: Synthetic spectrum, thin line, vs. the spectrum of SN 1981B, thick line, at maximum blue light (Branch et al., 1983).

this "full" spectral coverage. (The data obtained by the IUE for SN 1981B is rather noisy.) The UV provides crucial information for the understanding of the model atmosphere's density and temperature gradients. Figure 2.3 shows the problems inherent in fitting an observed spectrum solely in the optical by comparing our best fit to SN 1992A incorporating exponential and power law density gradients. In the optical it is a toss up as to which one fits the observed spectrum better; however, one can easily see that blueward of 3750Å the power law atmosphere has an extreme excess of of flux. This difference in flux is due to the different temperature gradients created by each density profile. One should therefore treat models which fit only a part of the "full" spectrum with some suspicion (Pistinner et al., 1995, in preparation).

2.7 Discussion

The input parameters as well as the results of our fits to these SNe Ia are listed in Table 2.1. Making the well founded assumption of homologous expansion, the reference radius is determined by $R_o = v_o t$ and hence our models predict the total emitted flux. Thus, we can convolve our flux with standard filters to predict absolute magnitudes. The absolute magnitudes were obtained using filter functions of Hamuy et al. (1992) as described in Baron et al. (1995)

Model	v_o(km s^{-1})	t(days)	$T_{\rm eff}$(K)	v_e(km s^{-1})	$\mathrm{M_{bol}}$	M_B	$B-V$
1981B	11400	17	9200	1500	-19.31	-19.42	0.08
1992A	8000	22	8900	1400	-18.99	-19.07	0.16

Table 2.1: The parameters used to fit SN 1992A and 1981B with the resulting absolute magnitudes and colors. Note that since SNe Ia have a large UV deficit the bolometric correction is positive.

To estimate our errors we conservatively assume errors of 0.2^m in the velocity,

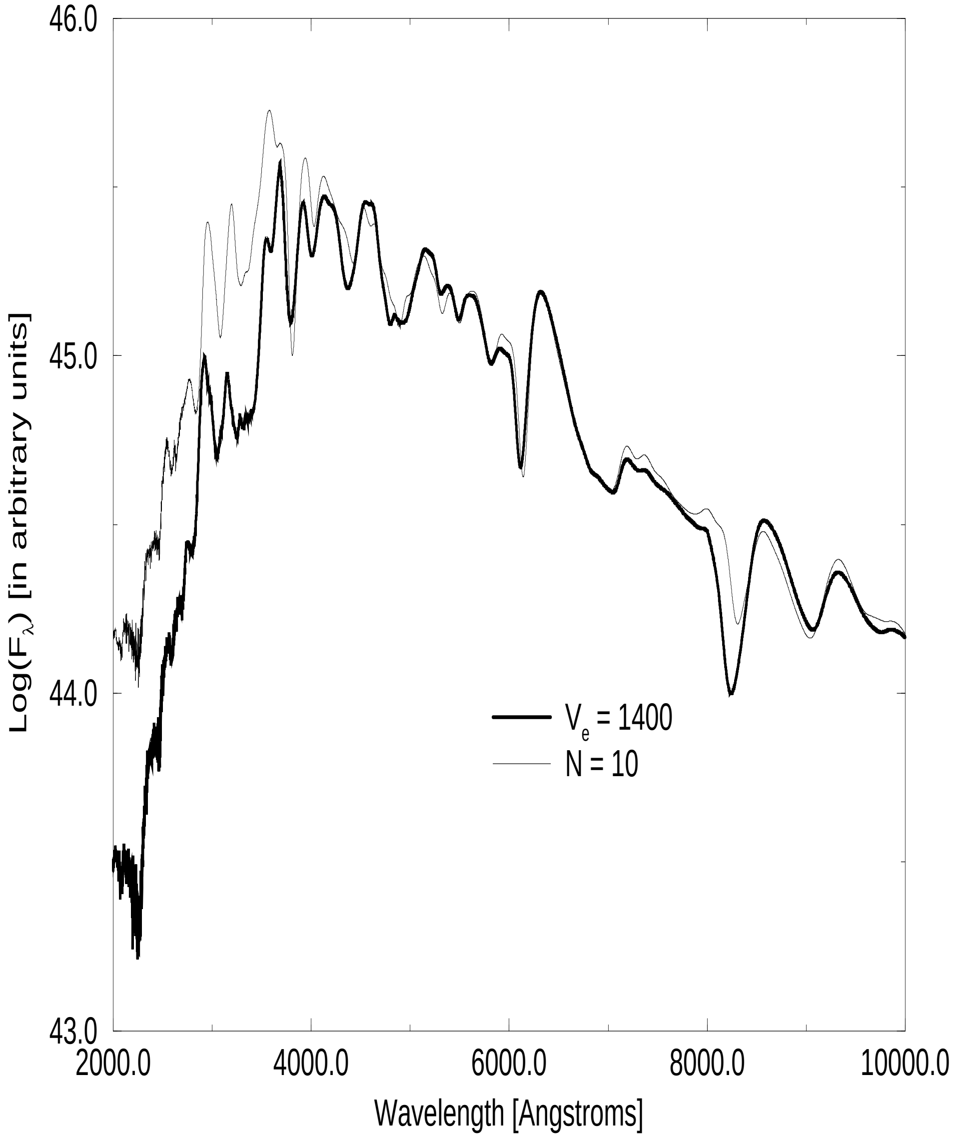

Figure 2.3: Two synthetic spectra. An $N = 10$ power law density gradient, thin line, vs. a $v_e = 1400$ exponential density gradient, thick line.

0.2^m for discrepancies in the composition and 0.25^m for the thermalization parameter α which compensates the lack of species considered in NLTE. We are presently implementing an Fe II model atom with 472 levels and 4505 NLTE transitions (Hauschildt et al., in preparation) which will lower the error due to α. Adding these in quadrature we arrive at error bars of $\pm$ 0.38^m for the absolute magnitudes.

With reasonable fits to two SNe Ia we can address the differences between them (Phillips, 1993a; Branch, Fisher, & Nugent, 1993a; Branch et al., 1994). A comparison of these SNe Ia would only be straightforward if performed at a similar time in their evolution (i.e. at maximum light). The spectra of SN 1992A was taken at 5 days after maximum light when it had already decreased 0.3^m in the blue from its peak (Suntzeff, 1992, in preparation). This would then make it almost the same magnitude as SN 1981B when it was at maximum light (M_B = -19.4^m). Yet this assumes that both these SNe Ia had a rise time of 17 days and there is some evidence that this is not the case.

If the light curves of these SNe Ia are compared to the light curve of SN 1990N (which has a well observed pre-maximum light curve) one notices that SN 1981B has a similar shape to SN 1990N while the light curve of SN 1992A rises and falls faster than both of them. This implies that SN 1992A had a shorter rise time. How much shorter should be resolved when a full EPM analysis of these SNe Ia are performed over a wide range in time around maximum light. For now we can estimate the rise time for these supernovae by making the simple assumption that the width of a light curve directly corresponds to its rise time. We use SN 1990N as a baseline light curve and fix its rise time at 20 days. The 20 days is arrived at by adding the 2.5 days it took the PDD3 model of SN 1990N (Khokhlov, Müller, & Höflich, 1992) to reach the first observed data point to the 17.5 days it then took for the supernova to reach maximum light (Khokhlov, Müller, & Höflich, 1992). To obtain the rise-time of SN 1981B and SN 1992A we linearly interpolate the width of the light curve 0.7^m below maximum from SN 1990N. The width of SN 1981B was 90% that of SN 1990N and SN 1992A was only 70% of SN 1990N giving rise times of 18 and 14 days, respectively. Given our peak blue magnitudes of $M_{B_{92A}} = -19.4^m$ and $M_{B_{81B}} = -19.4^m$, and using our derived rise times we may write the absolute magnitudes as:

$$M_{B_{92A}} = -18.9 - 5\log(t_r/14) \pm 0.4^m \tag{2.1}$$

$$M_{B_{81B}} = -19.5 - 5\log(t_r/18) \pm 0.4^m. \tag{2.2}$$

Note that the difference between the absolute magnitudes of these two SNe Ia is the same as implied by the Tully–Fisher (Pierce, 1994) and surface–brightness–fluctuations (Tonry, 1994, private communication) distances to their parent galaxies, Phillips (1993a) and Vaughan et al. (1995, in press), but arrived at in a very different manner. The two absolute magnitudes given above, together with the observational Hubble diagram for SNe Ia (Vaughan et al. 1995), give $H_0 \simeq 57 \pm 12$ km s^{-1} Mpc^{-1}. With apparent magnitudes B = 12.0 ± 0.1 for SN 1981B (Leibundgut et al., 1991) and 12.6 ± 0.1 for SN 1992A (Suntzeff, 1992, in preparation) the distance moduli are:

$$\mu_{92A} = 31.5 + 5\log(t_r/14) \pm 0.4^m \tag{2.3}$$

$$\mu_{81B} = 31.5 + 5\log(t_r/18) \pm 0.4^m. \tag{2.4}$$

2.8 Conclusions

We have presented spectral fits to SN 1981B and 1992A near maximum light which match the observed spectra well. It is apparent that we need to add Si II and O I to our list of NLTE species. Our models have shown the necessity of having both optical and UV coverage of an SNe Ia to constrain the density and temperature structures. Finally, we have demonstrated the ability to carry out an EPM analysis that provides a distance to SNe Ia independent of those based on the radioactive decay of ^{56}Ni and Cepheid variable stars.

Chapter 3

Physics and the Hubble Constant

3.1 Abstract

Two physical methods for determining luminosities and distances of Type Ia supernovae, the spectral fitting expanding atmosphere method and the ^{56}Ni radioactivity method, depend on the interval between the times of explosion and maximum brightness, but in differing ways. By requiring consistency between the two methods we derive blue and visual absolute magnitudes $M_B \simeq M_V \simeq -19.47 \pm 0.45$ mag which, together with the ridge line of Type Ia supernovae in the magnitude–redshift diagram, constrain the Hubble constant to be 57 ± 11 km s^{-1} Mpc^{-1}.

3.2 Introduction

Determining the value of the Hubble constant (H_0) by means of Type Ia supernovae (SNe Ia) is currently a topic of great interest. The attractive features of SNe Ia for this purpose include (1) that nearly homogeneous subsamples of them can be isolated; (2) that they are luminous and therefore can be observed to large distances; and (3) that they are reasonably well understood physical events which can be modeled.

To compare the results of theoretical models to observations, it is necessary to account for the response of detectors. It is convenient to work in the standard astronomical convention of magnitudes. The apparent magnitude in a particular band (m_x) is defined as

$$m_x = -2.5 \log \int_0^\infty S_x(\lambda)\, F_\lambda\, d\lambda + C_x \tag{3.1}$$

where $S_x(\lambda)$ is the filter response function for band x at wavelength λ, F_λ is the observed photon flux per unit wavelength, and C_x is a normalization constant which in practice is determined by observing comparison stars whose magnitudes are known. The absolute magnitude in band x, M_x, is defined as the apparent magnitude the object would have if it were observed at a distance of 10 pc. The bolometric magnitude, $M_{\rm Bol}$, can be defined in terms of the luminosity of the sun:

$$M_{\rm Bol} = -2.5 \log \left(\frac{L}{L_\odot} \right) + M_{{\rm Bol}_\odot}, \tag{3.2}$$

where $L_\odot = 3.85 \times 10^{33}$ ergs s^{-1} is the luminosity of the sun, and $M_{{\rm Bol}_\odot} = 4.72$ mag is the absolute bolometric magnitude of the sun.

Normal SNe Ia, e.g., those which at maximum brightness have broad–band blue–minus–visual color index $|m_B - m_V| < 0.25$ mag, have intrinsic absolute magnitude dispersions $\sigma(M_B) \simeq \sigma(M_V) < 0.2$ mag Sandage & Tammann (1993); Vaughan et al. (1995, in press); Hamuy et al. (1995); Sandage & Tammann (1995, in press); Vaughan, Branch, & Perlmutter (1995, in preparation). In the magnitude–redshift diagram, normal SNe Ia form a ridge line Hamuy et al. (1995); Sandage & Tammann (1995, in press); Vaughan, Branch, & Perlmutter (1995, in preparation) which corresponds to

$$\begin{aligned} M_B &\simeq M_V \\ &\simeq -19.75 \pm 0.10 \\ &\quad + 5 \log \left(\frac{H_0}{50 \text{ km s}^{-1} \text{ Mpc}^{-1}} \right) \text{ mag.} \end{aligned} \tag{3.3}$$

Thus, the determination of the absolute magnitude of a normal SN Ia provides the value of H_0. Furthermore, because our present understanding of SNe Ia Branch & Khokhlov (1995, in press) allows them to be modeled and their absolute magnitudes to be calculated, SNe Ia provide a determination of H_0 which is independent of all other distance determinations in astronomy.

3.3 Theory

In this chapter we combine two ways to calculate the luminosity of SNe Ia: (1) the spectral fitting expanding atmosphere method (SEAM), which is based on modeling the optical–ultraviolet spectrum, and (2) the ^{56}Ni radioactivity method, which is based on the theory that the SN Ia light curve is powered by the radioactive decay of ^{56}Ni through ^{56}Co to ^{56}Fe. These two methods depend on the rise-time $t_{\rm R}$, the interval between the times of explosion and maximum brightness, in different ways. This then allows us to write down two equations involving the unknowns t_R and L and solve for them.

Given the assumptions that radioactivity powers the light curve and that near the time of maximum light most of the energy released by radioactivity is still being trapped and thermalized, the peak radiated luminosity is expected to be comparable to the instantaneous rate of energy release by radioactivity Arnett (1982); Arnett, Branch, & Wheeler (1985); Branch (1992). Thus the peak luminosity can be expressed as

$$L_{\rm Ni} = \alpha \dot{S}(t_R) M_{\rm Ni} \tag{3.4}$$

where $\dot{S}$ is the radioactivity luminosity per unit nickel mass, evaluated at time t_R, $M_{\rm Ni}$ is the mass of ^{56}Ni synthesized in the explosion, and α, the ratio of bolometric to radioactivity luminosities, is near unity. Using e-folding decay times for ^{56}Ni and

^{56}Co of 8.8 and 111 days, and mean energy releases per decay of 1.71 and 3.76 MeV, the radioactivity luminosity per solar mass of ^{56}Ni becomes Branch (1992):

$$\begin{aligned}\dot{S} = \quad & 6.31 \times 10^{43}\, e^{-t_{\rm R}/(8.8\,{\rm days})} \\ & +1.43 \times 10^{43}\, e^{-t_{\rm R}/(111\,{\rm days})} \quad {\rm ergs\ s^{-1}\ M_\odot^{-1}}.\end{aligned} \tag{3.5}$$

3.4 Hydrodynamical Models

In order to constrain the value of $M_{\rm Ni}$, we focus on hydrodynamical models for SNe Ia that include calculations of light curves and spectra. Höflich's Höflich (1995) work on the normal SN Ia 1994D combines detailed hydrodynamical explosion models with spectrum synthesis. This approach proves extremely useful in rejecting certain models for SNe Ia. Not only do his models have to replicate the light curve but they must also synthesize the proper elements which make up the SN Ia's atmosphere in order to properly fit the spectrum. His acceptable models for SN 1994D are M35, M36 and M37. These show a range of $0.51 \leq M_{\rm Ni} \leq 0.67\ M_\odot$. In addition to this work, Harkness Harkness (1991a); Wheeler, Harkness, & Khokhlov (1995) shows that for the normal SN Ia 1989B, model W7 of Nomoto et al. Nomoto, Thielemann, & Yokoi (1984) ($M_{\rm Ni}$=0.58 $M_\odot$) provides good fits to the series of spectra. Further he states that there are no acceptable models with $M_{\rm Ni} \leq 0.5\ M_\odot$. The light curves and spectra are sensitive to the nickel mass not only because the composition of the ejected matter directly affects the spectral lines, but also because the nickel mass determines the temperature of the ejected matter. Thus we adopt for the nickel mass the value,

$$M_{\rm Ni} = 0.6 \pm 0.2 \pm 0.1\ M_\odot, \tag{3.6}$$

where the first range covers the acceptable values found by Harkness Harkness (1991a) and Höflich Höflich (1995) and the second allows for any possible systematic effects.

For simple illustrative assumptions, including that of constant gas opacity, the value of α can be shown to be unityBranch & Khokhlov (1995, in press); Arnett (1982). Our estimate of α is based on the hydrodynamical work and light curve calculations such as presented by Khokhlov, Müller, and Höflich Khokhlov, Müller, & Höflich (1994) They find that in detailed calculations which take into account the dependence of the opacity on the temperature, α exceeds unity for models which have a sufficiently long rise time to be compatible with observation. This is due to the dependence of opacity on temperature; as the temperature falls toward 10^4 K the opacity also falls, internal energy is released rapidly, and the light curve peaks at a luminosity that exceeds the instantaneous radioactivity luminosity. For acceptable models for normal SNe Ia Branch & Khokhlov (1995, in press); Khokhlov (1995, private communication):

$$\alpha = 1.2 \pm 0.2. \tag{3.7}$$

Combining this with our $M_{\rm Ni}$ estimate we obtain:

$$\alpha M_{\rm Ni} = 0.72 \pm 0.29 \ M_{\odot}. \tag{3.8}$$

The values of α and $M_{\rm Ni}$ may be anti-correlated (e.g., for a high value of $M_{\rm Ni}$, radioactivity energy released near the surface of the explosion tends to escape directly rather than to be trapped and contribute to the thermalized luminosity). By ignoring any such anti-correlation in our error estimate our range for $\alpha M_{\rm Ni}$ should be conservative.

3.5 Spectrum Synthesis

We now turn our attention to the the spectrum synthesis models of Nugent et al. Nugent et al. (1995a) (seen in Chapter 2). Accurately solving the fully relativistic radiation transport equation along with the non-LTE rate equations (for some ions) and ensuring radiative equilibrium (energy conservation) led to quality fits to the near-maximum-light spectra of SN 1992A and SN 1981B. These models allowed them to predict the supernova luminosity with the following assumptions: (1) Homologous expansion, $v \propto r$, from which it follows that the velocity of a given matter element is constant and hence that the position of a reference radius is given by $v_0 t_\mathrm{R}$, where v_0 is determined by the spectral fit. (2) The density gradient for the atmosphere follows a decaying exponential. (3) A high-quality fit to the spectrum implies that the model parameters were accurately determined. This method is in the spirit of the Baade method Baade (1926); Kirshner & Kwan (1974); Branch et al. (1981b) and the more detailed expanding photosphere method of Eastman and collaborators Eastman & Kirshner (1989); Schmidt, Kirshner, & Eastman (1992). To avoid confusion with photospheric based methods we refer to our present method, which entails fitting the spectrum of individual supernovae, as the Spectral-fitting Expanding Atmosphere Method (SEAM).

Clearly the luminosity depends on the rise-time through assumption (1). The fits to the normal SNe Ia 1981B and 1992A are good; thus we assume that the model parameters are determined reasonably well. From the models we find that the peak luminosity for SNe 1981B and 1992A is:

$$L_\mathrm{SEAM} = 1.60 \pm 0.7 \times 10^{43} \left(\frac{t_\mathrm{R}}{17\ \mathrm{days}}\right)^2 \ \mathrm{ergs\ s^{-1}}. \tag{3.9}$$

3.6 Results

In Figure 3.1 we display the rise-time dependence of the two methods to determine the peak luminosity of normal SNe Ia. From this figure we find that L is in the range $1.0 - 2.3 \times 10^{43}$ ergs s^{-1}, which corresponds to $M_\mathrm{Bol} = -19.25 \pm 0.45$ mag. In order

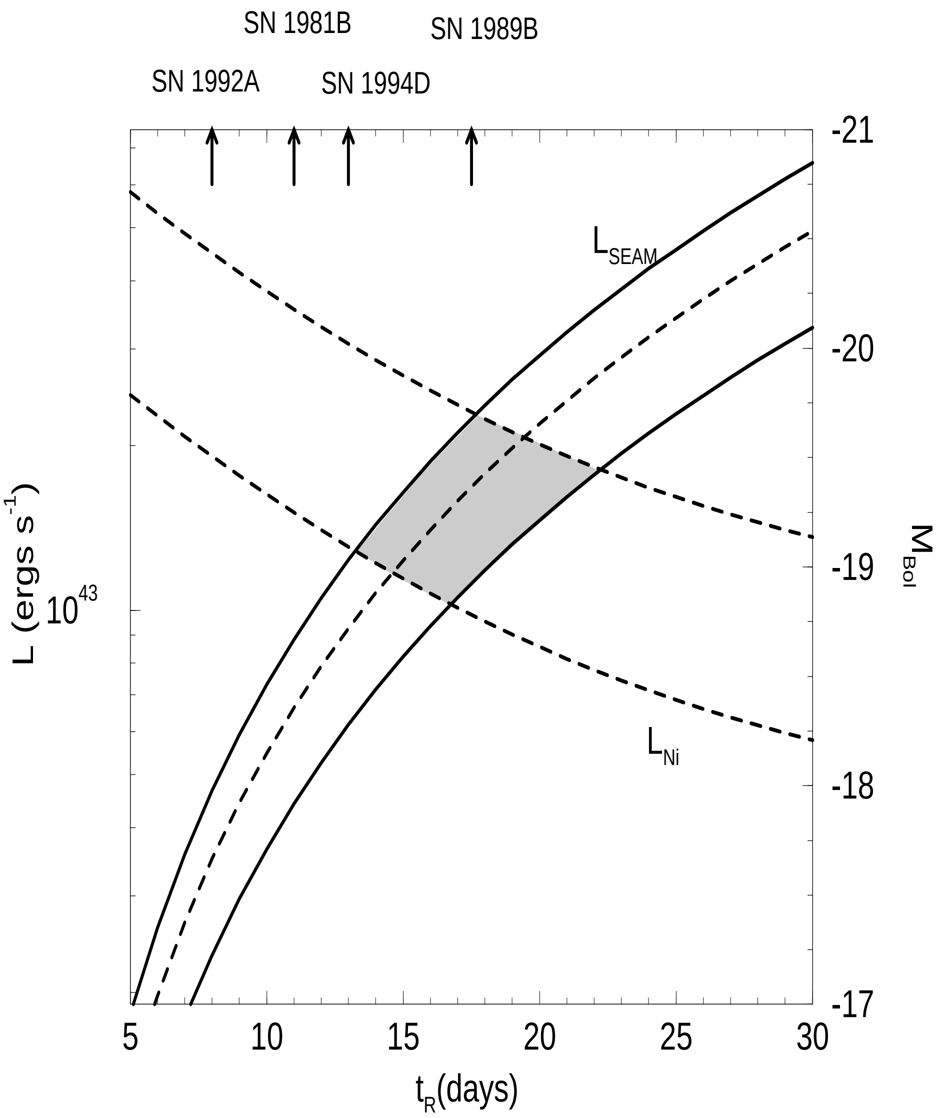

Figure 3.1: The luminosity of Type Ia supernovae as a function of rise-time. The band labeled L_{Ni} is the range of luminosity allowed by nickel radioactivity and the band labeled L_{SEAM} is the range of luminosity allowed by the spectral fitting expanding atmosphere method. The intersection is the allowed range of rise-times and luminosities. The arrows denote the minimum possible rise-times allowed by observation for the indicated supernovaeKirshner et al. (1993); Branch et al. (1983a); Marvin & Perlmutter (1989); Richmond et al. (1995).

to compare to observations we must apply a bolometric correction to convert from M_{Bol} to the observationally accessible quantity, M_B. This quantity is a prediction of the models of Nugent et al. Nugent et al. (1995a), where the synthetic photometry is performed as described in Baron et al. Baron et al. (1995), however we have corrected an error that appeared in both those publications and will be described in detail elsewhere. We find $M_{\mathrm{Bol}} - M_B = 0.23$ mag. The bolometric correction is positive due to the fact that the flux from SNe Ia is highly non-Planckian; there is a large UV deficit due to line blanketing. Thus, the B-band is significantly brighter than it would be for a more nearly Planckian stellar spectral energy distribution of the same luminosity. Since the spectral energy distribution is the primary result of our modeling we are able to calculate the flux in any given filter band without additional error.

Applying this correction we find:

$$M_B = -19.47 \pm 0.45 \text{ mag.} \tag{3.10}$$

If we make the assumption that the normal SNe Ia that were used to derive this result (SNe 1981B, 1989B, 1992A and 1994D) are similar to the normal SNe Ia found on the ridge-line of the Hubble diagram for SNe Ia Vaughan et al. (1995, in press) we can apply Eq. 3.4 to obtain the Hubble constant:

$$H_0 = 57 \pm 11 \text{ km s}^{-1} \text{ Mpc}^{-1}. \tag{3.11}$$

3.7 Conclusions

Even normal SNe Ia are not entirely homogeneous, as demonstrated by observed correlations between absolute magnitude and photometric Hamuy et al. (1995); Sandage & Tammann (1995, in press); Riess, Press, & Kirshner (1995) or spectroscopic Fisher et al. (1995) properties of SNe Ia. Direct application of the methods discussed in this *Letter* to more distant SNe Ia would obviate the "standard candle" assumption and reduce the uncertainty in the value of H_0.

Our result for H_0 agrees with that of Höflich and collaboratorsHöflich et al. (1995); Höflich & Khokhlov (1996) and other SN Ia based methods Hamuy et al. (1995); Riess, Press, & Kirshner (1995) within the quoted errors, and indeed SNe Ia based methods are nearly converged.

Many astronomers find observational evidence that the value of the Hubble constant is high (≈ 80 km^{-1} s^{-1} Mpc^{-1}), which leads to the possibility of a cosmic "age problem" Hogan (1994); Pierce et al. (1994); Jacoby (1994); Freedman et al. (1994) and the need for a remedy such as a cosmological constant. On the other hand, SN Ia absolute magnitudes determined by means of Cepheid variables in the SN Ia parent galaxies Saha et al. (1994, 1995, in press) are consistent with our physically based estimate of the SN Ia absolute magnitude. Other physically based determinations of the value of the Hubble constant by techniques that are independent of local astronomical distance calibrations — time delay in a gravitationally lensed "double quasar" Dahle, Maddox, & Lilje (1994) and the Sunyaev–Zel'dovich effect in clusters of galaxies Jones et al. (1993); Birkinshaw & Hughes (1994) — also require low values of H_0.

We conclude that our present physical understanding of SNe Ia requires that the value of H_0 be low — and that the expansion age of the universe is not necessarily inconsistent with the ages of the oldest stars.

Chapter 4

A Spectroscopic Sequence Among SNe Ia

4.1 Abstract

In this chapter we present evidence for a spectral sequence among Type Ia supernovae (SNe Ia). The sequence is based on the systematic variation of several features seen in the near-maximum light spectrum. This sequence is analogous to the recently noted photometric sequence among SNe Ia which shows a relationship between the peak brightness of a SN Ia and the shape of its light curve. In addition to the observational evidence we present a partial theoretical explanation for the sequence. This has been achieved by producing a series of non-LTE synthetic spectra in which only the effective temperature is varied. The synthetic sequence nicely reproduces most of the differences seen in the observed one and presumably corresponds to the amount of ^{56}Ni produced in the explosion.

4.2 Introduction

Much of the recent work on SNe Ia has focused on the photometric differences between individual events. Correlations have been found between the absolute magnitudes at maximum light and the light curve decline rates. Relationships such as $\Delta m_{15}(B)$[1] vs. M_B (Phillips, 1993b; Hamuy et al., 1995) and the Light Curve Shape analysis (Riess, Press, & Kirshner, 1995) highlight this work. A explanation for these photometric correlations has been provided by Höflich (1995) and Höflich & Khokhlov (1996) in which detailed hydrodynamic modeling has shown that SNe Ia which produce more ^{56}Ni are brighter and have light curves which decay more slowly.

Spectroscopic correlations with absolute magnitude (or light curve decline rate) have also been searched for, but with mixed success to date. Pskovskii (1977, 1984) and Branch et al. (1981a) found evidence that the velocity of the minimum of the Si II λ6355 absorption near maximum light was correlated with decline rate, but modern data do not appear to support this claim (Wells et al., 1994). Wells et al. (1994) suggested that the velocity of the minimum of the Ca II H&K absorption at maximum light may be correlated with decline rate, while Fisher et al. (1995) showed that the visual absolute magnitude is correlated with the minimum ejection velocity of calcium as measured from the H&K lines in moderately late-time spectra. Several authors have also called attention to general trends in the relative strengths of certain lines (e.g., Si II and Ti II) in the spectra of SNe Ia suggesting that these are correlated with decline rate (Phillips, 1993b; Hamuy et al., 1995; Branch, Fisher, & Nugent, 1993b). Nevertheless, a robust numerical analysis of these trends has not yet been performed. In this *Letter* we discuss the evidence for such a spectroscopic sequence, presenting specific relationships between M_B and 1) the ratio of the strength of the Si II absorption features found near 5800 and 6150 Å, and 2) the flux difference across the Ca II H&K absorption blend. Through the use of detailed non-LTE calculations of the spectra of SNe Ia we provide partial explanations for

[1] The parameter $\Delta m_{15}(B)$ is defined as the amount in magnitudes that the B light curve declines during the first 15 days following maximum light.

these correlations. Additionally, we make note of several other trends seen in both the observed and synthetic spectral sequences.

4.3 Observations

Figure 4.1 presents a spectroscopic series of SNe Ia near maximum light. The observational sequence is placed in order of decreasing luminosity (increasing $\Delta m_{15}(B)$) as found in citephilm15 with the flux scaled arbitrarily for easier viewing. (The synthetic spectral sequence will be discussed in the following section). By placing the spectra in this order several trends become readily apparent along the observed sequence:

1. A pronounced difference occurs with the Ti II feature near 4200 Å. This is the most distinctive feature in the blue part of the spectrum of SN 1991bg. One can also see this absorption feature in SN 1986G, and perhaps a hint of it in SN 1992A. It is not present in SNe 1981B, 1990N and 1991T. However, these SNe show a more subtle change at these wavelengths as the Fe II lines in SN 1981B give way to the Fe III features seen in SNe 1990N and 1991T.

2. Two features which decrease in strength as one moves up the sequence are the absorption troughs at 7500 and 8200 Å. These features are associated with O I, Mg II and Ca II.

3. The relative strengths of the two absorption features which form the distinctive "W" absorption feature at ∼5400 Å normally ascribed to S II are observed to vary in strength along the sequence. The red line is stronger than the blue in the faster-declining (lower-luminosity) SNe, but as one moves up the sequence the two lines become nearly equal in strength in SNe 1981B and 1990N, whereas

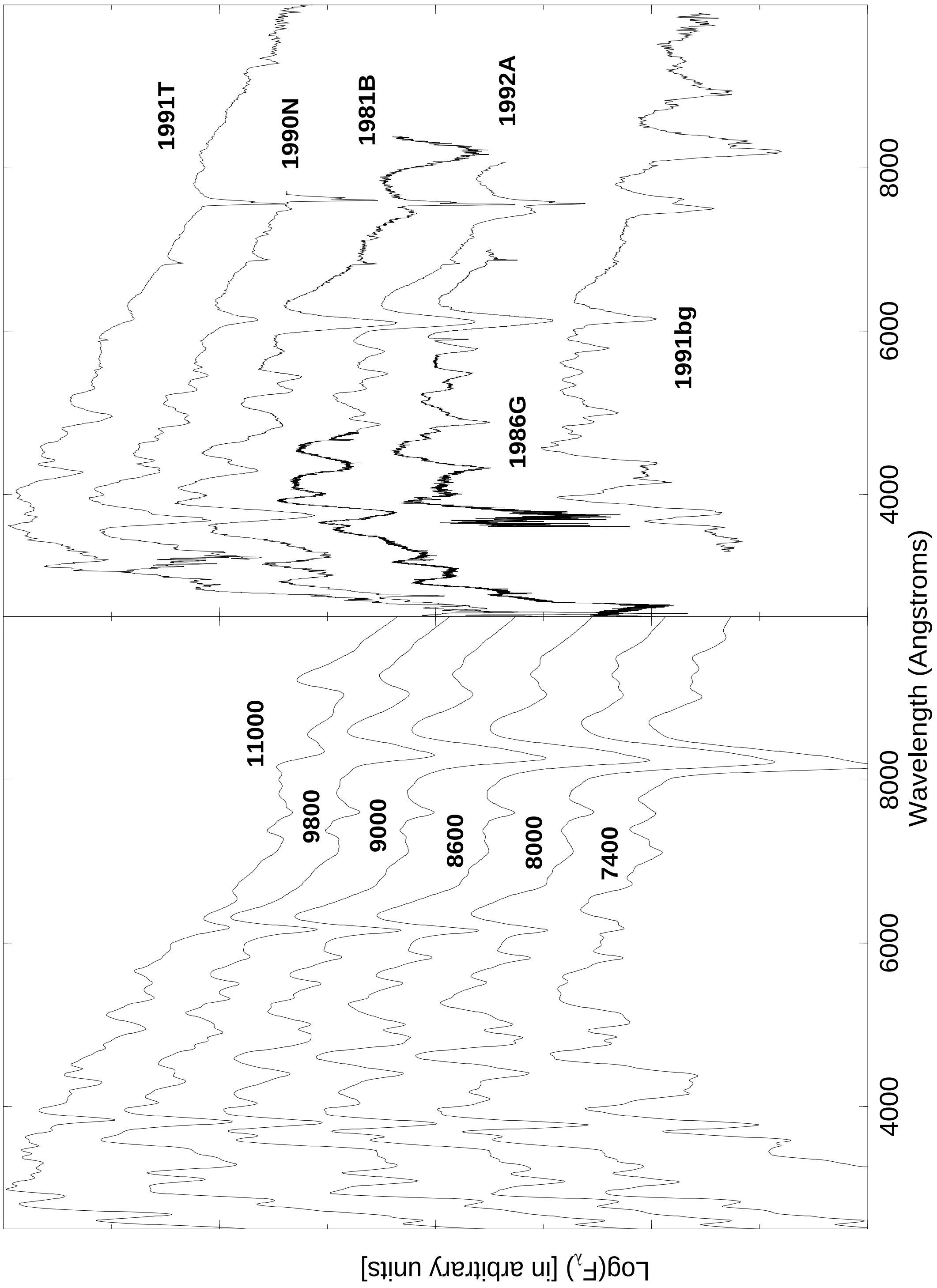

Figure 4.1: A plot of the synthetic (left) and observed (right) spectral sequences. Note the evolution in each graph of the following spectral features: Ca II at 3800 and 8200 Å, Ti II at 4200 Å and Si II at 5800 and 6150 Å.

the blue line finally grows stronger than the red in the spectrum of SN 1991T.

4. Another interesting trend is observed in the relative strengths of the apparent emission features located just to the blue and red of the 3800 Å Ca II H&K absorption trough. This ratio becomes increasingly stronger as one moves up the sequence until the "jump" across the absorption essentially disappears in SN 1991T.

5. The Si II absorption troughs at 5800 and 6150 Å are perhaps the most striking features to evolve in this sequence. Proceeding up the sequence, the strength of the absorption at 5800 Å decreases with respect to the one at 6150 Å.

SN	B	μ	E_{B-V}	M_B	$\mathcal{R}$(Si II)	$\mathcal{R}$(Ca II)	References [a]
1991T	11.69(03)	30.60(30)	0.13(05)	-19.44(36)	0.14(05)	0.94(11)	1,2,3
1981B	12.03(05)	30.50(30)	0.10(05)	-18.88(37)	0.16(05)	1.42(11)	4,2,3
1994D	11.86(03)	30.68(13)	0.00(02)	-18.82(16)	0.29(05)	1.38(11)	5-6,7,8
1990N	12.73(03)	31.40(30)	0.00(02)	-18.67(31)	0.16(05)	1.14(11)	9,2,3
1989B	12.34(05)	29.40(30)	0.37(03)	-18.58(33)	0.29(05)	1.29(11)	10,2,3
1992A	12.57(03)	30.65(11)	0.00(02)	-18.08(14)	0.38(05)	1.58(11)	11,2,3
1986G	12.45(05)	27.71(08)	0.65(10)	-17.92(42)	0.53(05)	2.07(11)	12,2,3
1991bg	14.76(10)	31.08(08)	0.00(02)	-16.32(15)	0.62(05)	2.56(11)	13,2,3

Table 4.1: Observed $\mathcal{R}$(Si II) and $\mathcal{R}$(Ca II).

[a](spectra, μ, B & E_{B-V}) (1) Phillips & other (1992), (2) Phillips (1993b), (3) Hamuy et al. (1996, in preparation), (4) Branch et al. (1983b), (5) Meikle et al. (1996a), (6) Patat et al. (1996), (7) Tonry (1996, in press), (8) Richmond et al. (1995), (9) Mazzali et al. (1993), (10) Wells et al. (1994), (11) Kirshner et al. (1993), (12) Phillips & other (1987), (13) Filippenko et al. (1992a).

Figure 4.2 illustrates the latter two correlations. The ratio of the two Si II absorption features was measured via the following procedure. First, the spectrum is put onto an F_λ vs. wavelength scale and then de-redshifted to correct for the radial velocity of the host galaxy. Second, the narrow Na I D interstellar lines (if present) are removed from the spectrum. Third, three "continuum" points are chosen to perform the analysis of the relative strengths. These points are the maxima in the

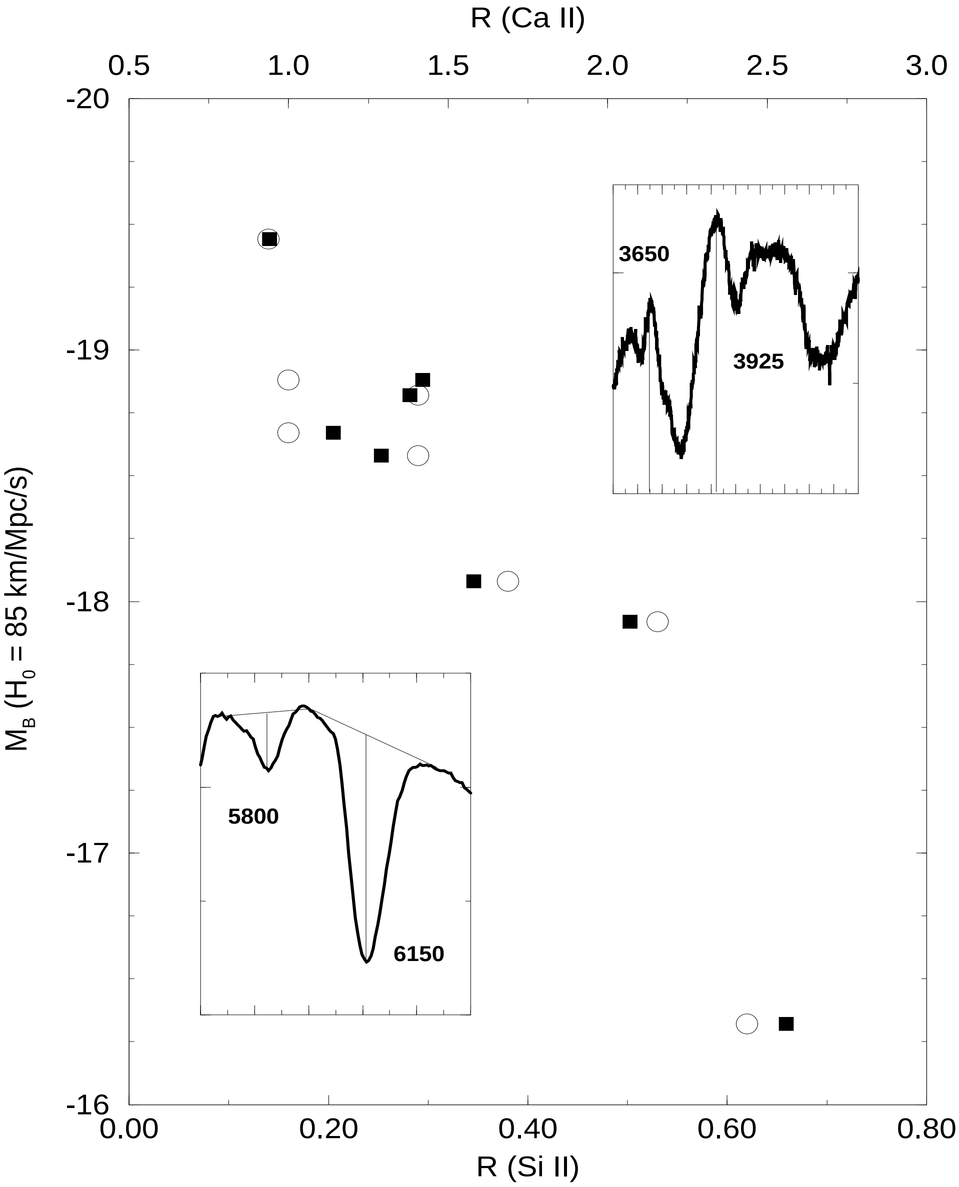

Figure 4.2: Observed M_B vs. $\mathcal{R}$(Si II) (open circles) and $\mathcal{R}$(Ca II) (filled squares) The inset graphs illustrate how the ratios were measured. Error estimates can be found in Table 4.1.

emission features found just blue of the 5800 Å trough, between the two Si II troughs and to the red of the 6150 Å trough. Line segments are drawn between adjacent continuum points and then the difference in flux between the corresponding line and the minimum for each trough is calculated. Figure 4.2 displays the absolute blue magnitude M_B vs. the ratio of the fractional depth of the bluer absorption trough to the redder one (which we refer to as the Si II ratio, $\mathcal{R}$(Si II)). Table 4.1 lists these values and their references. Note that the absolute luminosities were derived using the Surface Brightness Fluctuations and IR Tully-Fisher distance moduli listed by Phillips (1993b) and Richmond et al. (1995), and therefore reflect the "short" distance scale ($H_0 \simeq 85$ km s^{-1} Mpc^{-1}). The errors quoted for each ratio are rough estimates based on uncertainties in the reddening (which produce an almost negligible difference) and the night to night evolution of the spectrum. For the latter we examined the change in the ratios over a 10 day period centered on maximum light. The errors do not include the effects of poorly calibrated spectra. One might be tempted to assume a linear correlation between M_B and $\mathcal{R}$(Si II), but as will be shown in the next section the reason behind this relationship is rather complex and can not be easily broken down into a simple correlation.

The flux ratio across the Ca II H&K absorption trough was measured in a similar fashion. After placing the SN spectrum on an F_λ vs. wavelength scale and de-redshifting to correct for the host galaxy radial velocity, the flux is measured at two wavelengths, the maxima of the emission features which straddle the Ca II absorption. The Ca II ratio, $\mathcal{R}$(Ca II), is then defined as the ratio of the flux of the redder feature to the flux of the bluer feature. Figure 4.2 shows this ratio plotted vs. M_B. As is clearly seen, the relationship is remarkably similar to that observed for the Si II ratio; indeed, a plot of $\mathcal{R}$(Ca II) vs. $\mathcal{R}$(Si II) reveals a high degree of correlation between the two measurements.

4.4 Theory

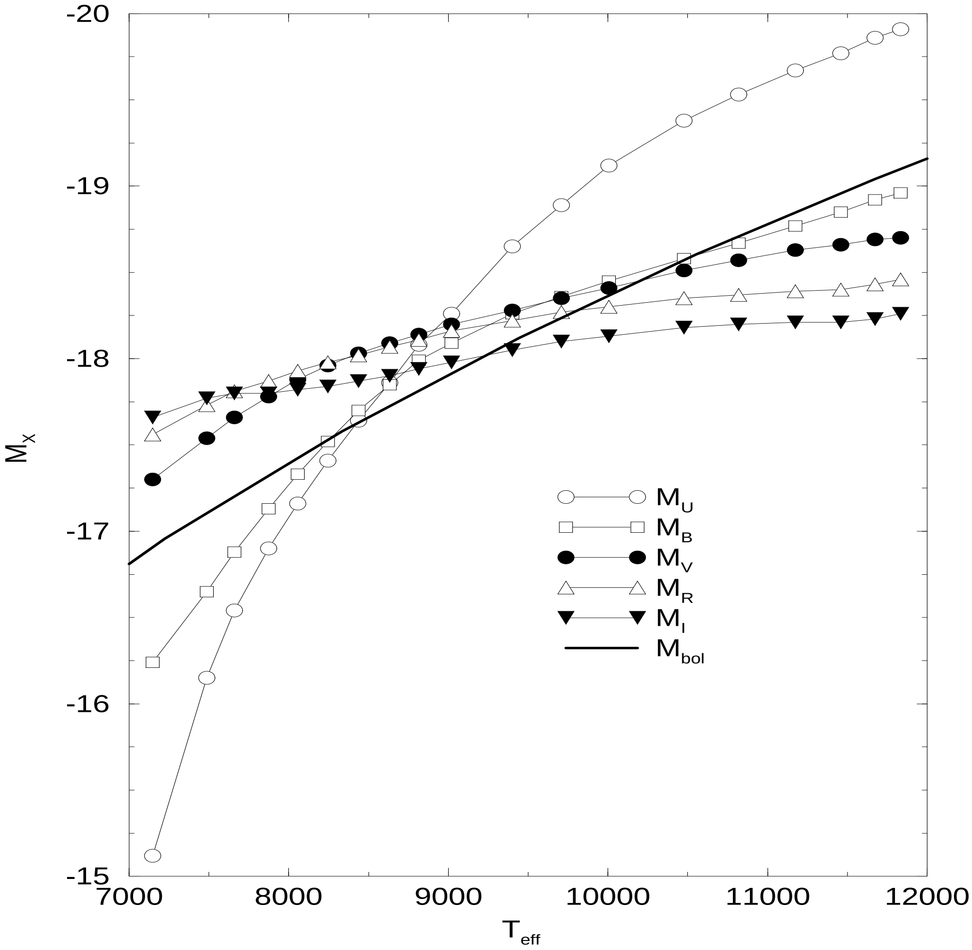

Figure 4.3: Photometry in U, B, V, R and I for the synthetic spectra.

In addition to the observed spectra shown in Figure 4.1 are six synthetic spectra. These spectra were produced with the code `PHOENIX` 4.8 (Hauschildt, 1992a,b, 1993;

Hauschildt et al., 1995; Baron et al., 1995; Hauschildt & Baron, 1995; Hauschildt et al., 1996). This code accurately solves the fully relativistic radiation transport equation along with the non-LTE rate equations (for some ions) while ensuring radiative equilibrium (energy conservation). The following ions were treated in non-LTE: Na I (3 levels), Ca II (5 levels), Mg II (18 levels), O I (36 levels) and Fe II (617 levels). All of the spectra are based on the same model parameters (one which produced a reasonable fit to SN 1991bg). The models have the following parameters: $t_{\rm rise} = 15$ days (number of days since explosion), $V_R = 7500$ km/s (the velocity at the reference radius) and $V_e = 900$ km/s (the e-folding velocity which defines the density profile by $\rho(r) = \rho_o e^{-V/V_e}$). The reference radius, R, is the radius where the continuum optical depth at 5000 Å is unity. The abundances are taken from model W7 (Nomoto, Thielemann, & Yokoi, 1984), homogenized for $v \geq 8000$ km s^{-1}, except that the titanium abundance has been increased by a factor of 10. The synthetic sequence was generated by varying *only* the observed luminosity of the SN, L. For easy reference to the spectra, we define the effective temperature, $T_{\rm eff}$, as follows: $T_{\rm eff}^4 = L/(4\pi R_o^2 \sigma)$. This is an input parameter of our models but our analysis makes no assumption about the existence of a photosphere. The models are all in radiative equilibrium so of course the temperature structures differ between them.

This synthetic sequence ranges in $T_{\rm eff}$ from 7400 to 11,000 K. With only this change the synthetic spectra are able to reproduce most of the differences seen in the observed spectra. It must be noted that a particular synthetic spectrum does not correlate one to one with an observed spectrum (better fits can be obtained by adjusting the parameters), rather the values for $T_{\rm eff}$ were chosen such that the trends seen in the observed sequence would be highlighted in the synthetic spectra.

The synthetic sequence reproduces the Ti II feature and its vanishing evolution as one increases $T_{\rm eff}$. The increase in $T_{\rm eff}$ causes the ionization of Ti II and the loss of its strong optical signature. Also of note is the effect the temperature change has on Ca II. One can easily see the decrease in strength of the infrared triplet as one moves up the sequence. This is once again caused by ionization. While observed data are sparse in this region SNe 1991bg, 1981B and 1991T definitely show this effect. Also, the emission feature blue-ward of the 3800 Å Ca II H&K blend shows the same increase in flux as is found in the observed spectra. This is due both to the increase in overall flux in the blue and to the ionization of Fe II and Co II, which decreases the line blanketing in this region of the spectrum, as $T_{\rm eff}$ is raised.

Even though Si II is treated in LTE, the synthetic sequence is able to reproduce a similar correlation as seen in the observed M_B vs $\mathcal{R}$(Si II). At first thought this correlation makes little sense. The trough at 5800 Å is due to a 4P-5S transition while the one at 6150 Å comes from the 4S-4P transition. Since they share the 4P level, and the line at 5800 Å line is produced by a transition with a higher excitation energy, it would be natural to think that this line should increase in strength relative to the 6150 Å line as $T_{\rm eff}$ is increased. The reason behind its decrease in strength as one moves up the sequence is due to a rather complex interaction of the lines with line blanketing from Fe II and Co II which increases the apparent strength of the 5800 Å line at lower $T_{\rm eff}$ while at higher $T_{\rm eff}$ Fe III and Co III line blanketing helps to wash out the feature. Note the nice correlation seen in the synthetic spectra for $\mathcal{R}$(Si II) and $\mathcal{R}$(Ca II) as the luminosity is increased (see Figure 4.1).$\mathcal{R}$(Si II) and M_B for each of the synthetic models is listed in Table 4.2 (for an assumed $H_0 \simeq 85$ km s^{-1} Mpc^{-1}).

Turning our attention towards the photometry of the synthetic models we can further explore the similarities between the models and observations. Figure 4.3

$T_{\rm eff}$	M_B	$\mathcal{R}$(Si II)	$\mathcal{R}$(Ca II)
12000	-18.96	-0.44	0.89
11700	-18.92	-0.82	0.88
11400	-18.85	0.01	0.87
11000	-18.77	0.00	0.87
10700	-18.67	0.02	0.83
10400	-18.58	0.03	0.77
10000	-18.45	0.23	0.74
9700	-18.36	0.28	0.79
9400	-18.26	0.33	0.86
9000	-18.09	0.41	1.01
8800	-17.99	0.45	1.08
8600	-17.85	0.49	1.10
8400	-17.70	0.54	1.13
8200	-17.52	0.61	1.18
8000	-17.33	0.70	1.26
7800	-17.13	0.82	1.36
7600	-16.88	0.93	1.56
7400	-16.65	0.95	2.14

Table 4.2: Synthetic $\mathcal{R}$(Si II) and $\mathcal{R}$(Ca II).

contains a graph of the absolute magnitude, in various bands, vs. $T_{\rm eff}$ for all of the models used to create the synthetic sequence. The most striking feature in this graph is the almost 5 magnitude change in M_U from the coolest to hottest model. (Note that in a more realistic sequence, where the more luminous models would have a longer risetime and hence a larger radius; these differences would only be enhanced.) Since previous fits to SNe 1981B and 1992A have been good in the UV (Nugent et al., 1995a), it is not unreasonable to think that this is representative of what happens in the observed spectral sequence. Unfortunately, the number of quality observations in U are rather limited. What we do have (Schaefer, 1995) does indicate such a trend (Branch et al., 1995a). One should also note that the range in absolute magnitude for all of the models decreases as one moves to redder photometric bands. This effect has manifested itself in Phillips (1993b) where the slope of the correlation between $\Delta m_{15}(B)$ and M_B is seen to be steeper than between $\Delta m_{15}(B)$ and M_I.

Figure 4.4 displays the maximum-light colors of the synthetic models vs. $T_{\rm eff}$. This figure shows that the U band is a powerful tool for discriminating the differences among SNe Ia. $U-B$ changes almost 2 magnitudes over this range of $T_{\rm eff}$ while the color differences seen in $V-R$ and $R-I$ barely span 0.5 magnitude. Also of note are the derived bolometric corrections for these models. [Note that we have corrected an error in our synthetic photometry that appeared in Baron et al. (1995) and Nugent et al. (1995a,b); see Nugent et al. (1995c)]. Models whose colors correspond to typical SNe Ia [$|B-V| < 0.2$ (Vaughan et al., 1995, in press)], correspond to models with $T_{\rm eff} \gtrsim 9000$ K.

In an effort to find a more direct connection between these models and the various light curve relationships we examined the Rosseland mean opacity, κ, at the center of each model (the center corresponding to an optical depth of $\tau \simeq 13$). It is well known that κ is proportional to $t^2_{\rm rise}$ (Arnett (1982); Baron, Young, & Branch (1993)). We found that in our hotter models $sqrt\kappa$ was 1.4 times greater than in our cooler models (see Fig 4.5. This is very near to what one would expect, given the available photometric data, for the ratio of $t_{\rm rise}$ between the extremes of SN 1991T and SN 1991bg.

4.5 Discussion and Conclusions

We have shown that the observed photometric sequence of SNe Ia (Phillips, 1993b; Hamuy et al., 1995; Riess, Press, & Kirshner, 1995) manifests itself equally clearly as a spectral sequence. This fact may prove to be extremely useful to current attempts to measure the deceleration parameter, q_o, through the discovery and observation of $z \sim 0.3$–0.5 SNe Ia. The problem facing these programs is to correct for the expected luminosity spread of the individual SNe. Until now, the only tool for doing this was

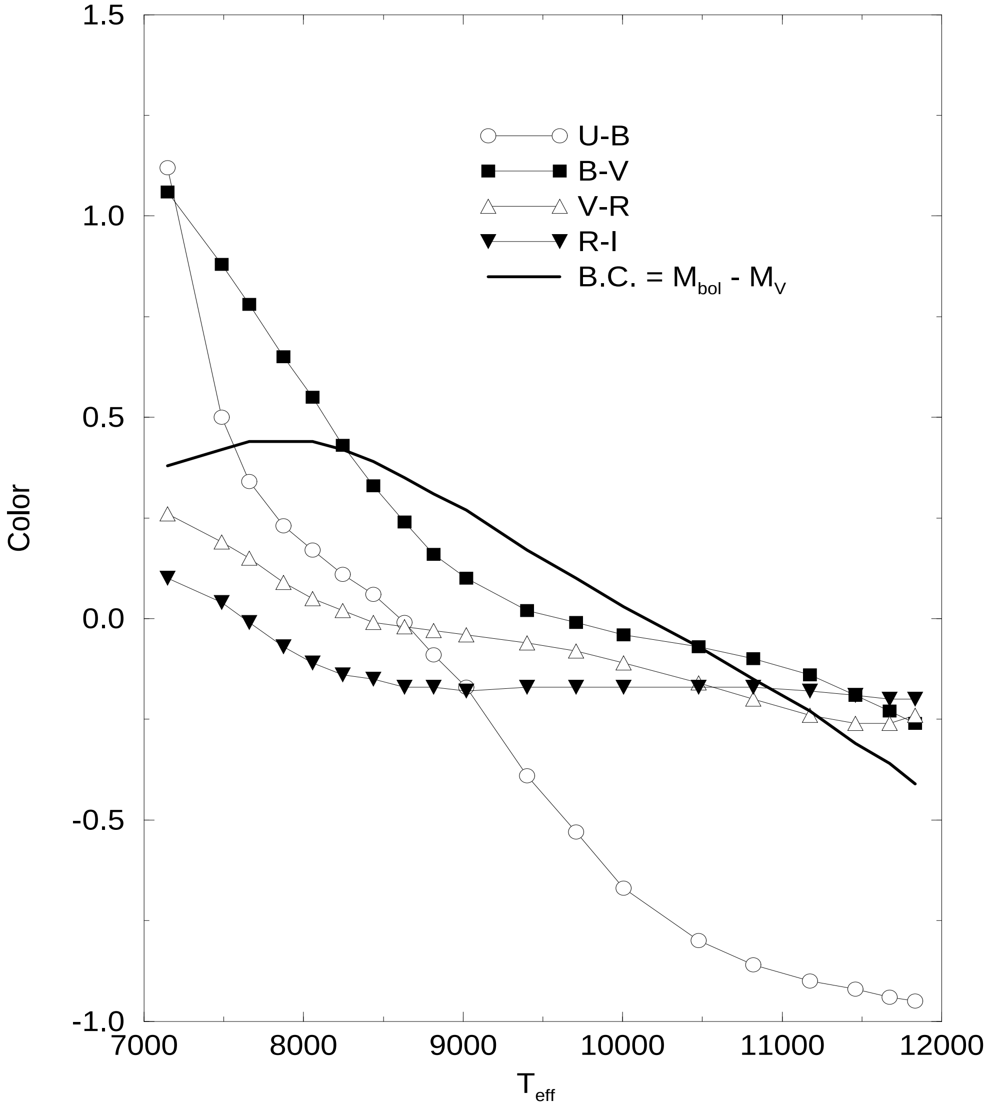

Figure 4.4: The colors for the synthetic spectra.

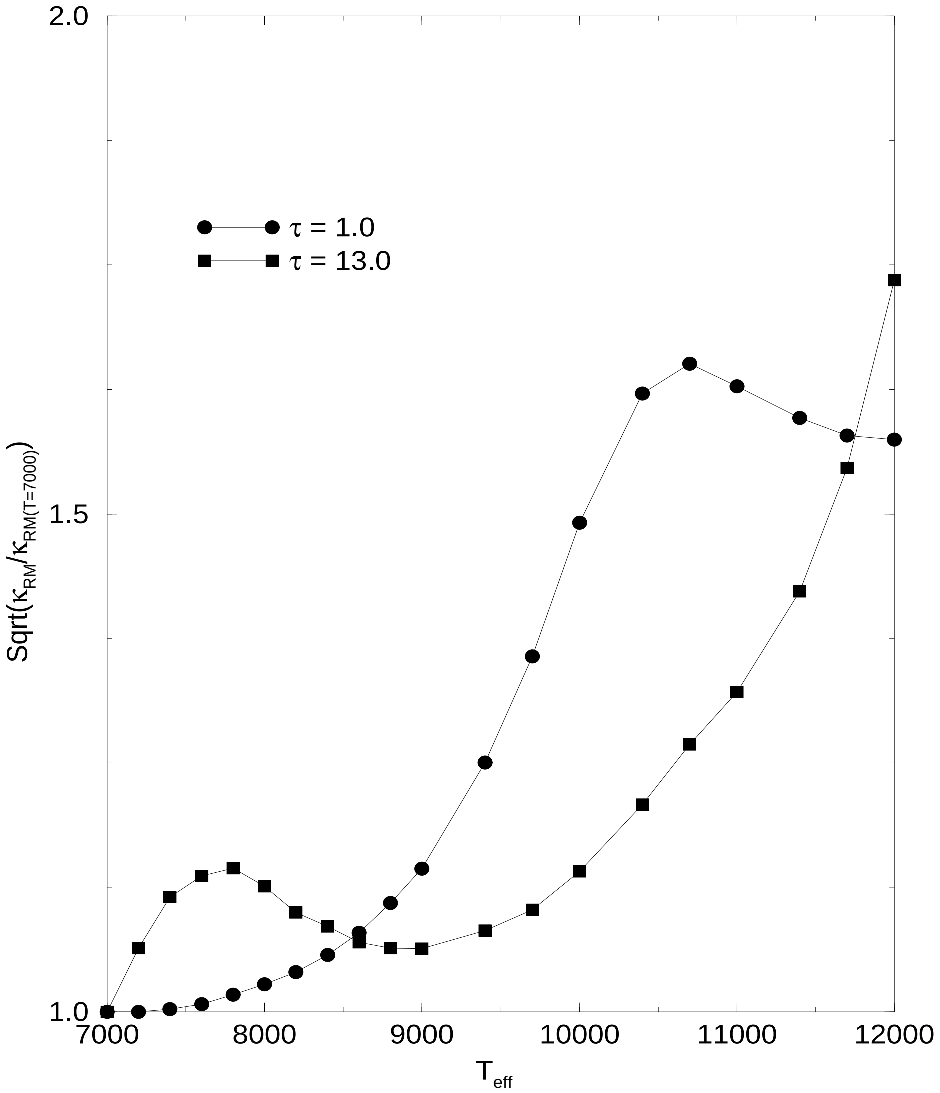

Figure 4.5: $\sqrt{\kappa_{RM}}$ for all the models at two different values of τ.

to measure the initial decline rate of the light curve [One could perform a color cut and eliminate peculiar SNe Ia (Vaughan et al., 1995, in press), but this could further deplete an already small, high z, sample of data]. However, if a spectrum is obtained at maximum light (which is required to verify that the SN is actually type Ia event), a measurement of either $\mathcal{R}$(Ca II) or $\mathcal{R}$(Si II) should, in principle, provide an independent estimate of the luminosity of the event. Of these two ratios, $\mathcal{R}$(Ca II) may prove to be the easier one to measure, particularly in the highest redshift SNe.

From our synthetic spectra, we conclude that the observed spectroscopic and photometric sequences of SNe Ia are due primarily to temperature differences. Since the supernova is almost entirely powered by the radioactive decay of ^{56}Ni, the temperature differences are likely to be due to the total amount of ^{56}Ni produced in the explosion. Undoubtedly abundance and velocity differences also play a role, but their effects are of secondary importance. We know, for example, that the titanium overabundance that we have used for the models in this paper is probably unique to underluminous SNe Ia such as SN 1991bg (Filippenko et al., 1992a). Nevertheless, in our temperature sequence the effects of the titanium overabundance are masked by the ionization of Ti II as one moves to higher temperatures. Similarly, while our hot model bears a strong resemblance to the maximum light spectrum of SN 1991T, the features produced by intermediate mass elements are too strong, since these elements were underabundant in this supernova (Jeffery et al., 1992). Further progress in understanding this spectroscopic sequence more fully is likely to come from a more detailed study of the two extremes observed so far in the sequence, SN 1991bg and SN 1991T. This will be the subject of further work.

Chapter 5

Hydrodynamic Models of SNe Ia

5.1 Abstract

We present detailed NLTE synthetic spectra of hydrodynamic SNe Ia models. We make no assumptions about the form of the spectrum at the inner boundary. We calculate both Chandrasekhar-mass deflagration models and sub-Chandrasekhar "helium detonators." γ-ray deposition is handled in a simple, accurate manner. We have parameterized the storage of energy that arises from the time dependent deposition of radioactive decay energy in a reasonable manner, that spans the expected range. We find that the Chandrasekhar-mass deflagration model W7 of Nomoto et al. shows good agreement with the observed spectra of SN 1992A and SN 1994D, particularly in the UV, where our models are expected to be most accurate. The sub-Chandrasekhar models do not reproduce the UV deficit observed in normal SNe Ia. They do bear some resemblance to sub-luminous SNe Ia, but the shape of the spectra (i.e. the colors) are opposite to that of the observed ones and the intermediate mass element lines such as Si II, and Ca II are extremely weak, which seems to be a generic difficulty of the models. Although the sub-Chandrasekhar models have a significant helium abundance (unlike Chandrasekhar-mass models), helium lines are not prominent in the spectra near maximum light and thus do not act as a spectral

signature for the progenitor.

5.2 Introduction

Type Ia supernovae (SNe Ia) are among the brightest known objects in the universe. Since they form a nearly homogeneous class and simple selection criteria can make the observed dispersion quite small, they are natural cosmological probes (Vaughan et al., 1995, in press). The observed homogeneity has led to a search for a homogeneous progenitor, that would satisfy the requirement of lacking hydrogen. This has led to the assumption that the SNe Ia progenitor involves the explosion of a Chandrasekhar-mass white dwarf. The current status of the search for the identification of the SNe Ia progenitor is reviewed in Branch et al. (1995b). Hydrodynamic explosion models have included deflagration models such as the "W7" model of Nomoto, Thielemann, & Yokoi (1984). While this model is somewhat hand-crafted to fit the observed spectra and suffers from an overproduction of neutron rich species, it remains the standard in the field. The "DD" (delayed detonation, Khokhlov, 1991a; Woosley, 1991) and "PDD" models (Pulsating Delayed Detonation, Khokhlov, 1991b) improve the predicted nucleosynthetic yield and gives qualitative agreement with the observed spectra and light curves (Höflich & Khokhlov, 1996).

The observation of the super-luminous SN 1991T (Jeffery et al., 1992) and the very sub-luminous SN 1991bg (Filippenko et al., 1992b) convincingly showed that the class of SNe Ia is not entirely homogeneous. In attempting to model SNe Ib, Livne & Glasner (1990, 1991) examined a "helium-igniter" where a sub-Chandrasekhar or a Chandrasekhar-mass C/O white dwarf with an accreted helium shell detonates near the center following the detonation of the helium shell. Motivated by observations of SN 1991T and 1991bg as well as other claims for evidence that SNe Ia form a sequence (Phillips, 1993b; Hamuy et al., 1995) Woosley & Weaver (1994) and Livne & Arnett (1995) investigated the helium-igniter as a realistic model for SNe Ia.

On the face of it helium-igniters have much to recommend them as a plausible progenitor model of SNe Ia. By varying the initial white dwarf mass such models can produce a range of nickel mass $M_{\rm Ni} \approx 0.2 - 1.0$ $M_{\odot}$, naturally leading to a sequence of supernovae. Sub-Chandrasekhar models do not suffer from the same neutronization problem that occurs in the C/O deflagration models, and population synthesis studies may produce the progenitors in the requisite quantities (Tutukov, Yungelson, & Iben, 1992), although not in old populations (Branch et al., 1995b).

On the negative side, the models produce an outer shell of the products of explosive helium burning: helium and ^{56}Ni; elements not typically associated with the outer layers of SNe Ia. In addition the light curves are extremely fast (Woosley & Weaver, 1994; Höflich & Khokhlov, 1996), so in particular, it is not clear that the observed photometric diversity can be reproduced by such models.

Since one of the primary goals of synthetic spectral synthesis is the confrontation of theoretical models with observations, we present the results of synthetic spectrum calculations of the helium igniter models of Woosley & Weaver (1994) and Livne & Arnett (1995). Since this is our first application of our program of synthetic spectral synthesis to hydrodynamical SNe Ia models, we also present the results of the spectral synthesis of the W7 model (Nomoto, Thielemann, & Yokoi, 1984).

5.3 Calculations

The calculations are performed using the generalized stellar atmosphere program `PHOENIX 7.1` (Hauschildt, 1992a,b, 1993; Hauschildt, Baron, & Allard, 1996) in generally the same way we have applied it previously to SNe Ia (Nugent et al., 1995a,d), although we have modified the code to allow the treatment of nebular boundary conditions, as well as stratified composition and a full *gamma*-ray deposition calculation. Our *gamma*-ray deposition calculation is based on a solution of the grey transfer equation as described in Sutherland & Wheeler (1984), modified in Young, Baron, & Branch (1993, 1995); Young (1994) and further modified in Nugent (1996). We have compared the results of our γ-ray deposition with more detailed calculations and the agreement is excellent (Young & Kumagai 1995, private communication), similar results have been found by e.g. Swartz, Sutherland, & Harkness (1995). The boundary conditions make no assumptions about the form of the flux at the inner boundary, but rather impose continuity requirements on the intensity (with correct Lorentz transformations). Thus all of the flux comes from the atmosphere itself, there is no "light bulb" at the center. The inner boundary is a small hole, through which radiation freely passes. We have performed extensive test calculations to ensure the the position of the inner boundary condition does not affect our results. `PHOENIX` accurately solves the fully relativistic radiation transport equation along with the non-LTE rate equations (for some ions) while ensuring radiative equilibrium (energy conservation). The following ions were treated in non-LTE in the calculations reported here (the number of levels follows in parenthesis): He I (11), He II (10), Na I (3), Ne I (26), Ca II (87), Mg II (18), C I (228), O I (36), Fe II (617), Co II (255), Ti II (204), S II (85) and Si II (94).

The hydrodynamical models were evolved in time by assuming that the expansion is homologous, i.e. the velocity of any given mass point was held constant. The models were rezoned into 50 mass zones, with roughly a logarithmic spacing in $\tau_{\rm std}$, where $\tau_{\rm std}$ is the total extinction optical depth in the continuum at 5000 Å. Care was taken to resolve the density profiles.

In theory, once we choose a time since explosion the model is completely determined. The density structure is specified by the homology transformation, the compositions are fixed in velocity by the hydrodynamical model (once decay of the radioactive species has been accounted for) and, since we use observed bolometric luminosity as an input parameter, the temperature structure is then completely determined by imposing the condition of radiative equilibrium. We parameterize the luminosity as:

$$L_{\rm bol} = \eta L_\gamma^{\rm abs}, \tag{5.1}$$

where $L_\gamma^{\rm abs}$ is the total instantaneous γ-ray luminosity *deposited in the material* and η is a parameter that measures the net amount of energy stored over time by the material. Note that η differs from the parameter α defined by Arnett and co-workers (Arnett, 1982; Arnett, Branch, & Wheeler, 1985) since α refers to the *total* instantaneous γ-ray luminosity, and instead corresponds to the parameter $\tilde{Q}$ of Höflich & Khokhlov (1996). [NB: While the definition of $Q \equiv \alpha$ in Höflich & Khokhlov (1996), in previous papers in their series Q corresponds to η]. Höflich & Khokhlov (1996) found η in the range $0.7 < \eta < 1.8$ for a wide variety of models that they examined, and we have varied η from approximately $0.5-2.0$. Actually η should be a function of radius, but an accurate calculation of η will require a NLTE, multi-group radiation-hydrodynamical calculation. This procedure accounts for the time-dependent nature of the deposition of radioactive energy in an accurate manner. Given an input luminosity the temperature structure of the models is determined by demanding the modified radiative equilibrium condition:

$$\int \kappa_\lambda (B_\lambda - J_\lambda)\, d\lambda - \dot{S} = 0, \tag{5.2}$$

where $\dot{S}$ is the local instantaneous rate at which γ-ray energy is deposited.

5.4 Results

5.4.1 Model W7

Figure 5.1 displays our synthetic spectrum for the W7 model at 20 d past explosion for three choices of η. This is several days after the time of bolometric maximum $t_{\rm bol} = 14$ d found by Höflich & Khokhlov (1996) and Khokhlov, Müller, & Höflich (1993) who found $\eta = 1.3$ at this time. The magnitudes and colors of these models are listed in Table 5.1. The model strongly resembles observed SNe Ia spectra, showing the defining Si II $\lambda6355$ line as well as the $\lambda5972$ line, and lines from Ca II, S II, O I, and Fe II. Also, there is the strong UV deficit that is characteristic of SNe Ia spectra. The colors for the $\eta = 1.0$ 20 d model are very similar (on average) to the colors found for normal SNe Ia. The $\eta = 2.0$ colors are too blue and the $\eta = 0.8$ are too red, suggesting that the value of $\eta = 1.3$, found by Höflich and collaborators is reasonable.

Time	η	$M_{\rm Bol}$	M_B	M_V	$B-V$	$U-B$
16 d	0.6	-18.48	-18.64	-18.60	-0.04	-0.35
16 d	0.9	-18.85	-18.95	-18.78	-0.18	-0.64
16 d	1.1	-19.10	-19.11	-18.92	-0.19	-0.79
16 d	1.7	-19.61	-19.44	-19.26	-0.17	-0.91
18 d	0.9	-18.70	-18.93	-18.83	-0.10	-0.37
20 d	0.8	-18.51	-18.71	-18.81	0.10	-0.09
20 d	0.9	-18.55	-18.77	-18.83	0.07	-0.12
20 d	1.0	-18.69	-18.93	-18.93	0.00	-0.17
20 d	2.0	-19.45	-19.54	-19.24	-0.30	-0.82
23 d	1.3	-18.75	-18.93	-19.04	0.10	-0.14
25 d	1.5	-18.81	-19.11	-19.08	-0.04	-0.20

Table 5.1: Magnitudes and Colors of W7 Models. $M_{\rm Bol}$, M_B, and M_V are the bolometric, B and V absolute magnitudes of the models respectively. $B-V$ and $U-B$ are the associated colors.

In addition to the NLTE lines that we treat directly, we must also include $\approx$

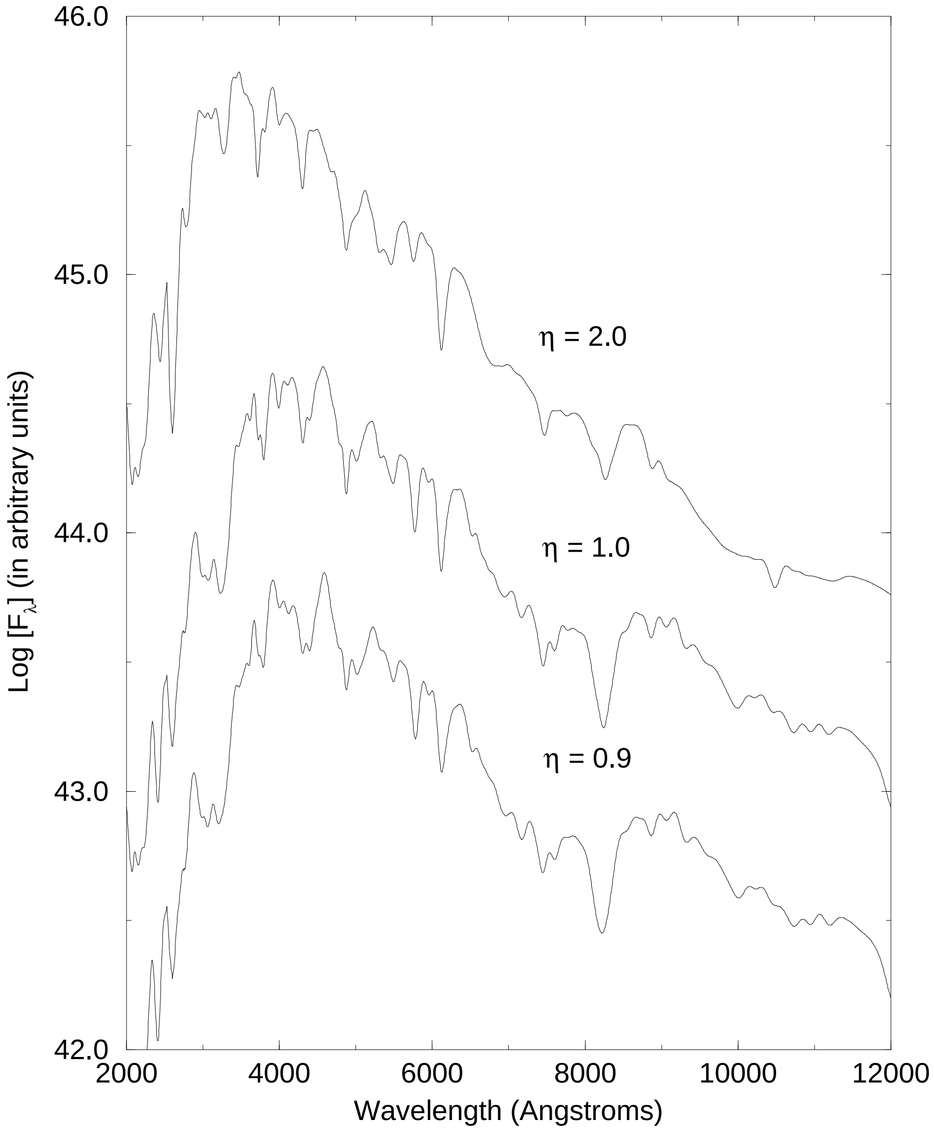

Figure 5.1: The synthetic spectrum for the W7 model at 20 d past explosion for three choices of η. The main effect of increasing η is to increase the effective temperature and hence for higher values of η the spectrum becomes more blue (see Table 5.1. Also the dominant ionization stage of iron moves from II to III, which reduces the line blocking in the UV and changes many of the optical lines. At the highest value of η Ca II becomes ionized and the IR triplet become much weaker.

2 million additional lines in LTE. The shape of the spectrum is somewhat sensitive to the constant scattering albedo α (the thermalization parameter $\epsilon = 1 - \alpha$) that we choose (Nugent et al., 1995a; Baron et al., 1996), where α is defined by the source function for LTE metal lines,

$$S_l = (1 - \alpha) \int \phi_\nu J_\nu d\nu + \alpha B_\nu(T). \tag{5.3}$$

Based on the results found in Appendix 2 we choose $\epsilon = 0.05 - 0.1$ as our standard range. All the models discussed below have $\alpha = 0.1$.

Figure 5.2 shows the W7 model at 23 d ($\eta = 1.3$) with an observed spectrum of SN 1992A [taken at 5 days after maximum light (Kirshner et al., 1993)] and at 20 d ($\eta = 1.0$) with an observed spectrum of SN 1994D [at maximum light in the optical and 3 days before maximum in the IR (Meikle et al., 1996b)]. The agreement is quite good across the entire range of observed wavelength for each supernova with all of the major (and most of the minor) features present in the synthetic spectra. This result agrees well with the LTE spectra of W7 calculated by Harkness (1991a,b). While fine tuning could no doubt improve the fits, that is not our purpose in this paper. An interesting feature in Figure 5.2, is that both the observed spectrum for SN 1994D and the synthetic spectra of W7 show a “split” just blueward of the Ca II H&K feature. This is likely due to a blend of Ca II H&K and Si II λ3858. Kirshner et al. (1993) also noted that the two lines are of nearly equal strength. While the split is prominent in the observed spectrum of SN 1994D, it is clearly absent in the observed spectrum of SN 1992A. We suspect that the absence of the split is due to having more calcium at higher velocity in SN 1992A than in SN 1994D, which strengthens the blending. The W7 model does not contain any pre-existing metals, which are likely to have been produced prior to the formation of the SN Ia progenitor by several generations of SNe II. Thus, it would be premature to speculate as to whether the

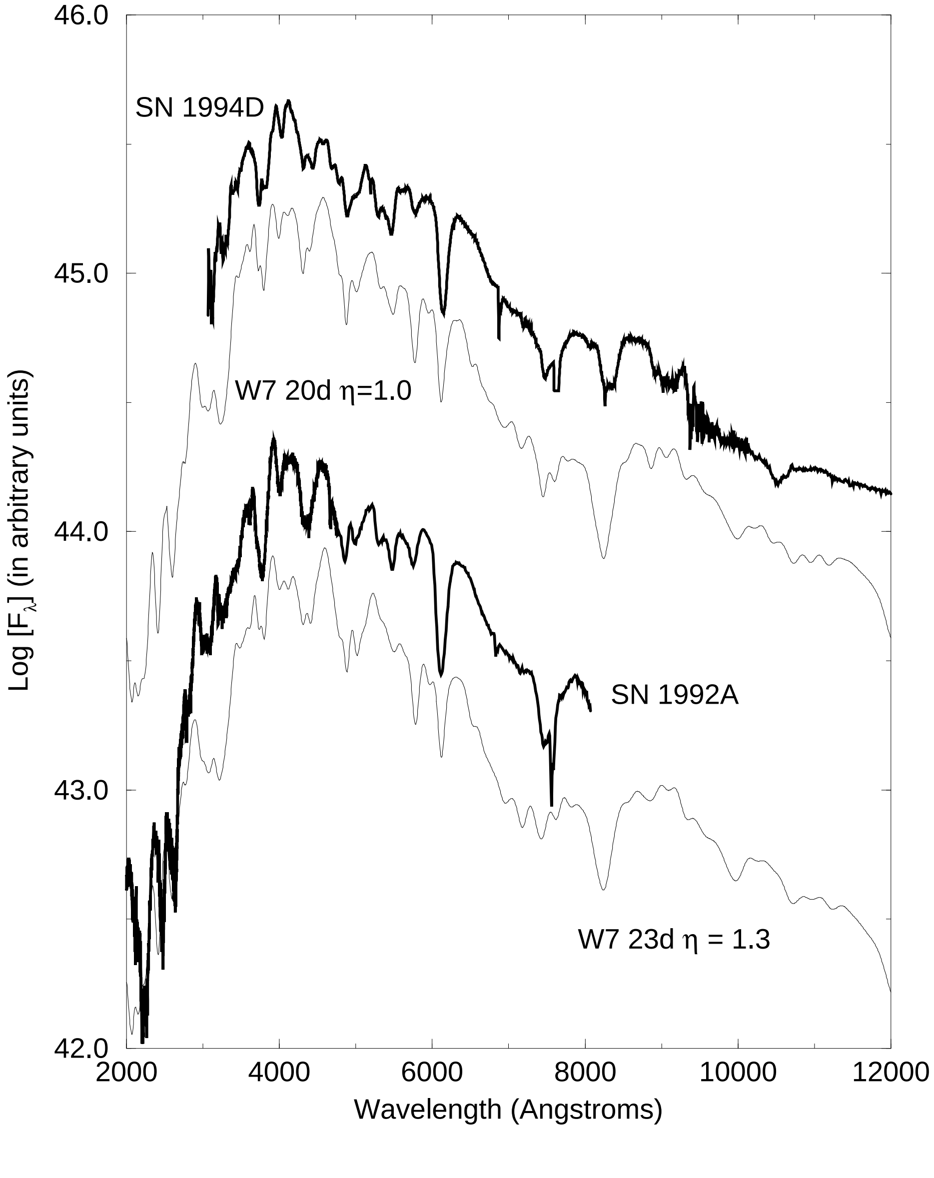

Figure 5.2: ,
The W7 model at 23 d ($\eta = 1.3$) compared with an observed spectrum of SN 1992A 5 days after maximum light (Kirshner et al., 1993), and at 20 d ($\eta = 1.0$) compared with an observed spectrum of SN 1994D, at maximum light (Meikle et al., 1996b).

spectrum of SN 1992A requires the nucleosynthesis of more calcium, or is due to differences in the pre-existing metallicity of the progenitors. We will return to this issue in future work.

Figure 5.3 shows the time evolution of the W7 model near maximum light. The bolometric magnitudes and colors of the 16 d, $\eta = 1.1$ and $\eta = 1.7$ models (see Table 5.1) should be compared with the results of Höflich & Khokhlov (1996) who found $M_{\rm bol} = -19.56$ and $B - V = 0.11$ (for $\eta = 1.3$). The bolometric magnitudes bracket the results of Höflich & Khokhlov (1996), while both of the models are somewhat bluer than they found. This is likely due to differences in the treatment of radiation transport (NLTE, 82,000 wavelength points and full line profiles, versus LTE grey transport) and serves as an estimate of the theoretical uncertainty of such calculations.

5.4.2 Sub-Chandrasekhar Models

Figure 5.4 displays Model 2 of Woosley & Weaver (1994) (WW2) 15 d after explosion for three choices of η. This model is the explosion of an 0.7 $M_\odot$ white dwarf that has accreted 0.2 $M_\odot$ of helium. Since these models are significantly less massive than W7, they peak earlier and hence it is sensible to examine them at earlier times. Figure 5.5 is similar to Figure 5.4, but for Model 4 of Livne & Arnett (1995) (LA4), which is a 0.7 $M_\odot$ white dwarf that has accreted 0.17 $M_\odot$ of helium. The magnitude and color data for these models can be found in Table 5.2. The synthetic spectra have less line-blanketing and hence more flux in the UV, than does the W7 model. There is no strong evidence of either He I or He II lines.

Although we do not use the Sobolev approximation at all in our calculations, we calculate the Sobolev optical depth of each NLTE line as a convenient diagnostic.

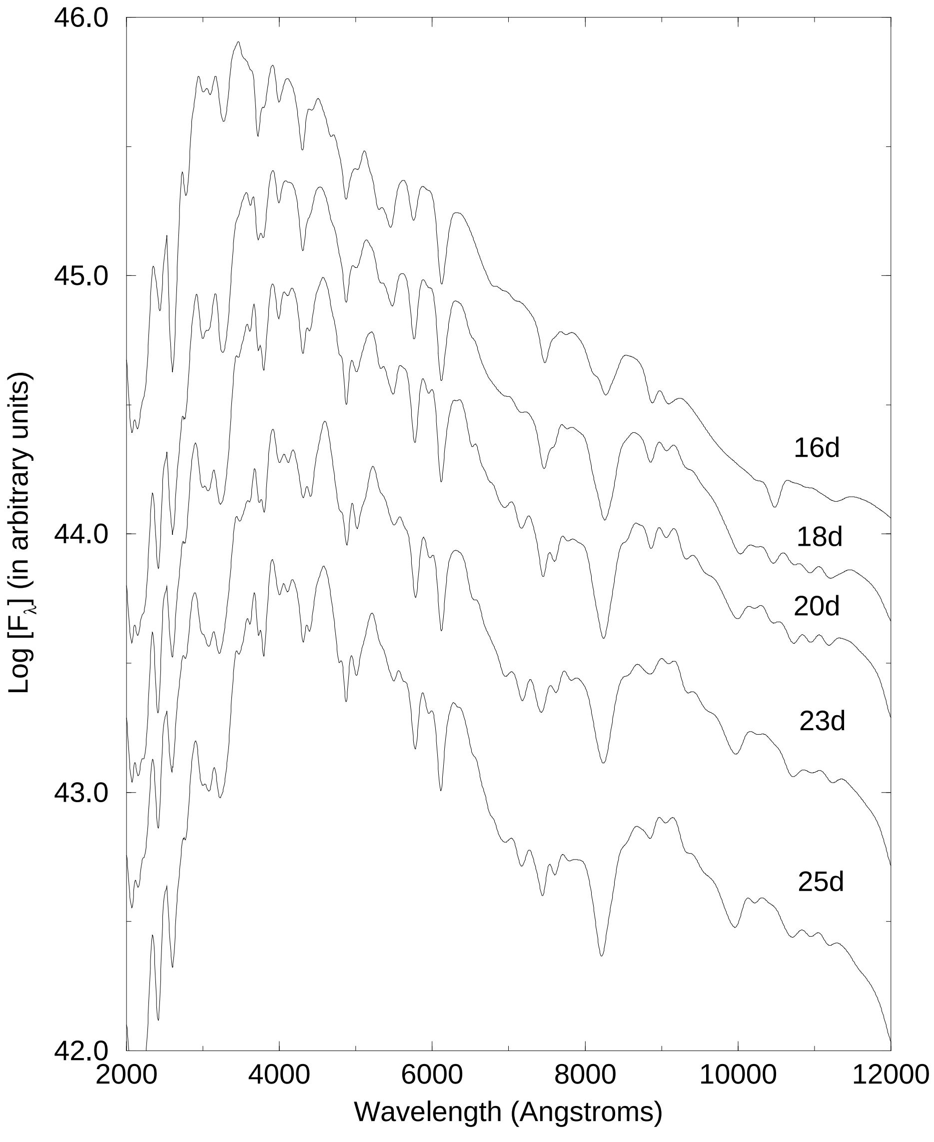

Figure 5.3: The time evolution of the W7 model near maximum light ($\eta = 1.1, 0.9, 1.0, 1.3, 1.5$ at $t = 16, 18, 20, 23, 25$ d, respectively) .

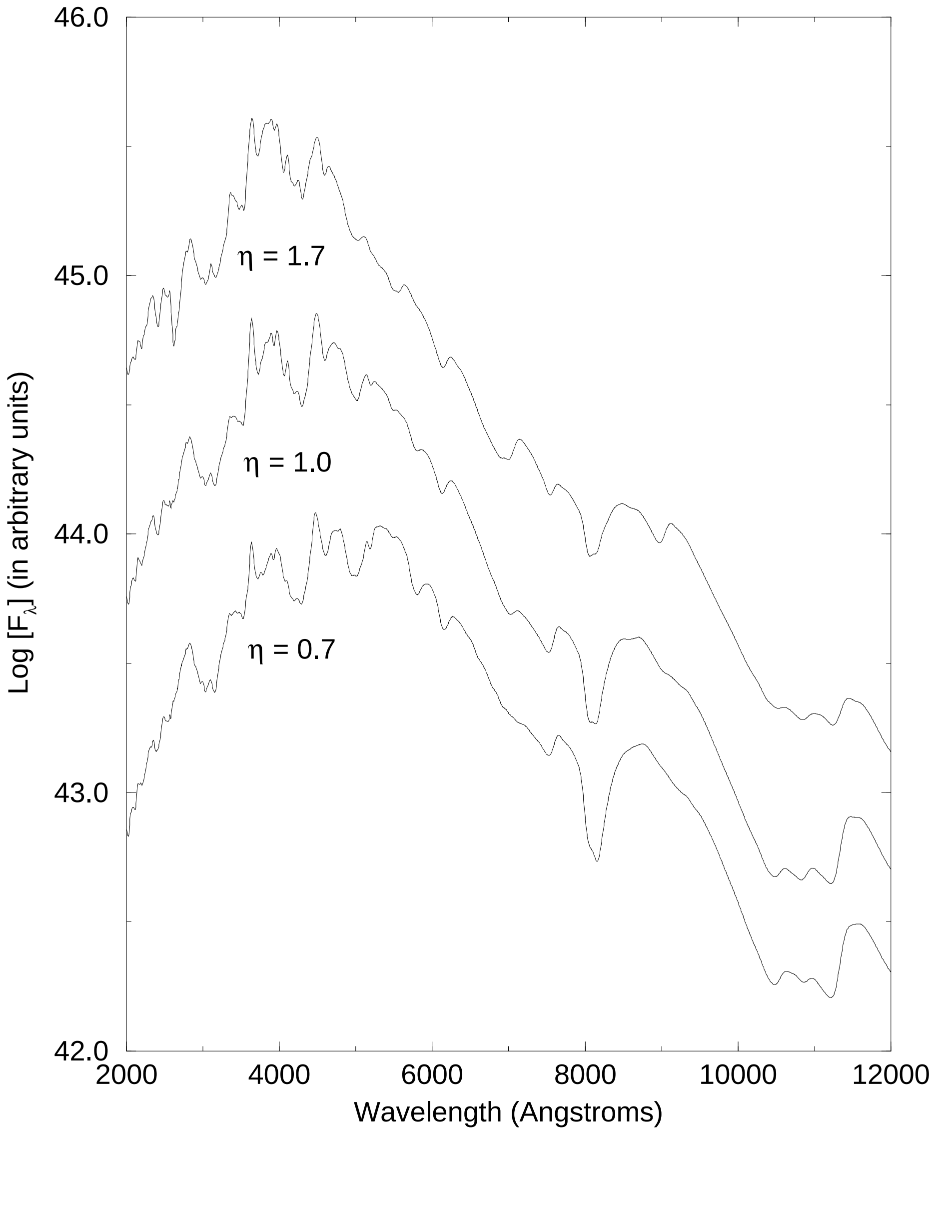

Figure 5.4: Model WW2 15 d after explosion for three choices of η.

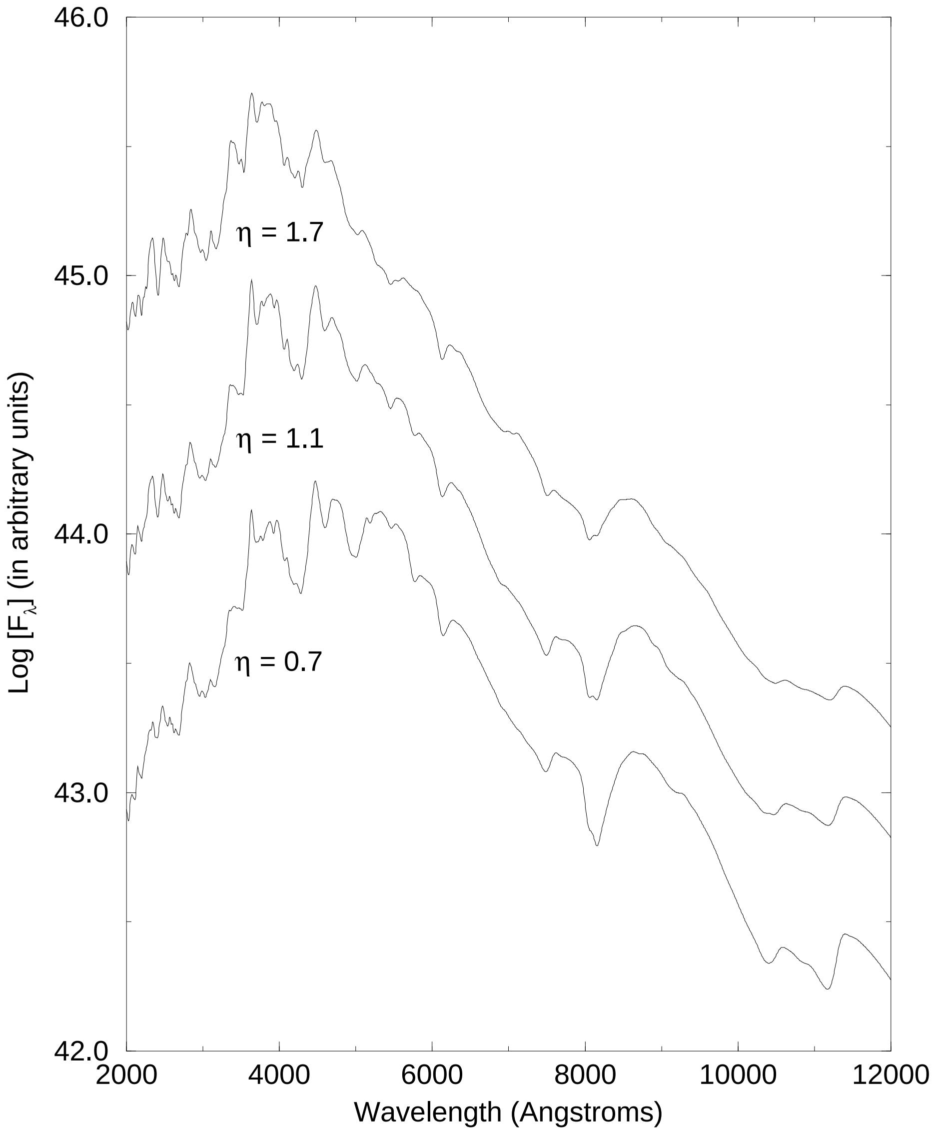

Figure 5.5: Model LA4 15 d after explosion for three choices of η.

Model	Time	η	$M_{\rm Bol}$	M_B	M_V	$B-V$	$U-B$
WW2	15 d	0.7	-18.08	-18.04	-18.68	0.64	-0.18
WW2	15 d	1.0	-18.49	-18.72	-18.82	0.10	-0.31
WW2	15 d	1.3	-18.78	-19.13	-18.83	-0.30	-0.46
WW2	15 d	1.6	-18.98	-19.33	-18.85	-0.48	-0.55
WW2	20 d	1.1	-18.22	-18.21	-18.95	0.74	-0.16
WW2	20 d	1.5	-18.51	-18.78	-18.97	0.19	-0.34
WW2	20 d	1.9	-18.80	-19.17	-18.82	-0.36	-0.65
LA4	15 d	0.7	-18.20	-18.30	-18.81	0.52	-0.17
LA4	15 d	1.1	-18.69	-18.99	-18.90	-0.08	-0.43
LA4	15 d	1.7	-19.17	-19.41	-18.91	-0.50	-0.76
LA4	20 d	1.5	-18.60	-18.96	-18.97	0.01	-0.39
LA4	20 d	1.6	-18.66	-19.03	-18.97	-0.07	-0.43
LA4	20 d	2.0	-18.89	-19.29	-18.91	-0.37	-0.60

Table 5.2: Magnitudes and Colors of the Sub-Chandrasekhar Models. $M_{\rm Bol}$, M_B, and M_V are the bolometric, B and V absolute magnitudes of the models respectively. $B-V$ and $U-B$ are the associated colors.

The Sobolev optical depth of the He I λ5876 lines is approximately $3-4$ orders of magnitude weaker than that of the Si II λ6355 line in both sets of models, thus these models are effective at "hiding helium." It is somewhat surprising that in a model with nearly 0.2 $M_\odot$ helium on the outside that no evidence of helium should appear. This seems to be due to the very strong non-thermal ionization and the high UV flux which tends to keep the helium ionized, and/or highly excited, suppressing the strong He I lines. Optical He II lines, particularly P_α λ4687.8 and P_β λ3204.5, are also not prominent. Figure 5.6 displays the Sobolev optical depths of the helium lines *throughout* the atmosphere as long as the electron scattering optical depth is larger than 0.1.

As expected the strongest lines are in the far UV. Focusing on the He I λ5876 line Figure 5.6 shows that at a few points in the atmosphere the Sobolev optical depth is significant. However, as illustrated in Figure 5.7 this line is blended with

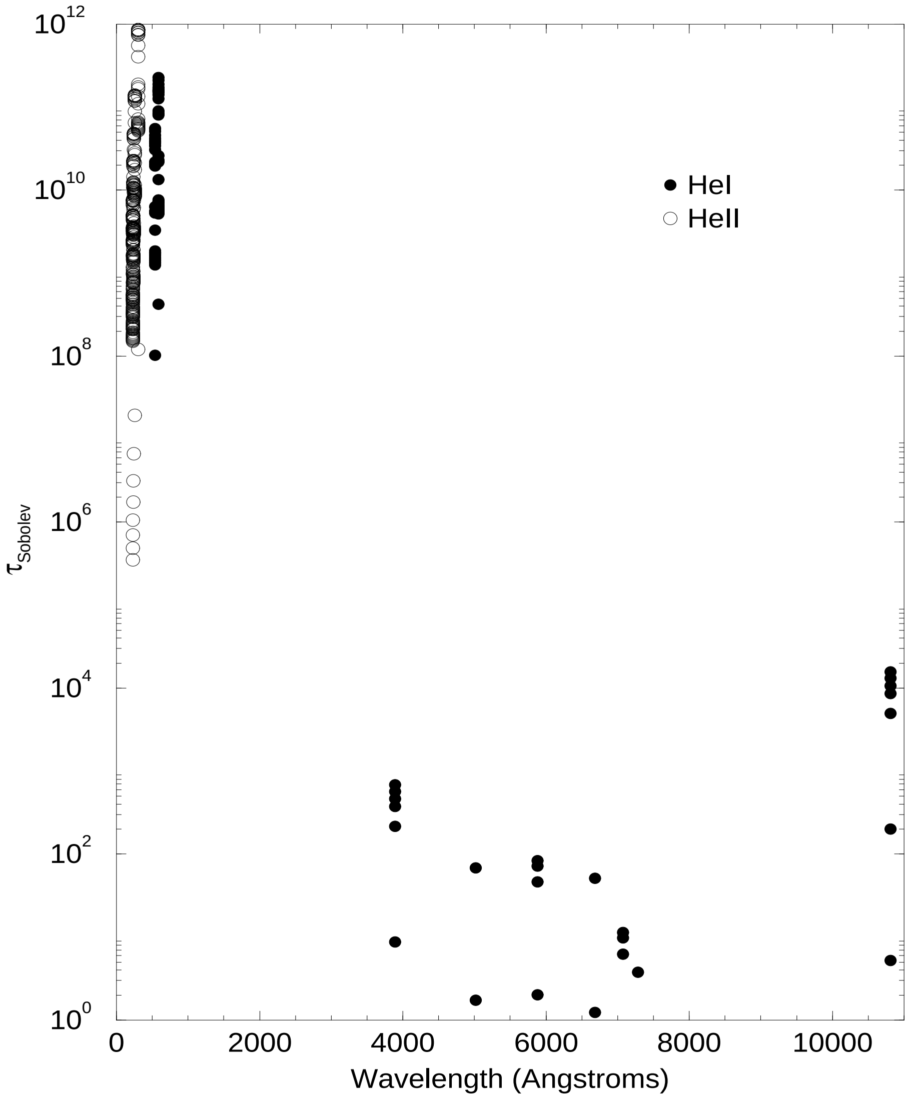

Figure 5.6: The Sobolev optical depths of the helium lines throughout the atmosphere of Model WW2, 20 d after explosion, with $\eta = 1.1$, for regions where the electron scattering optical depth is larger than 0.1.

strong Si and S lines and show isn't a clean signature for the presence of helium. At earlier times, with higher densities recombination may populate the He I – II levels, but since the models will also be hotter at those times, it is not clear *a priori* that optical He I – II lines will ever be strong in these models. Understanding the exact suppression mechanism of helium lines will be the subject of future work.

Figure 5.8 shows the synthetic spectra of the models of WW2 ($\eta = 1.1$) and LA4 ($\eta = 1.5$) at 20 d, compared with the observed spectrum of SN 1994D. Clearly the synthetic spectra bear little resemblance to the observed SN Ia spectrum. The Si II $\lambda 6355$ line is quite weak and may not extend to high enough velocity. This is a generic problem with sub-Chandrasekhar models. The 15-d WW2 model of Figure 5.4 does however reproduce the boxy shape of the Ca IR triplet seen in SN 1994D, which may indicate that the calcium is confined to the correct velocity range in the model.

Sub-Chandrasekhar models have been suggested as attractive models for low luminosity SNe Ia such as SN 1991bg. The spectra of this SN Ia [at maximum (Filippenko et al., 1992b) in the optical and IUE data in the UV (Cappellaro, Turatto, & Fernley, 1995)] along with the spectra of the 20 d models of WW2 ($\eta = 1.1$) and LA4 ($\eta = 1.5$) can be seen in Fig. 5.9. These models show some resemblance to the observed SN 1991bg spectrum, however, the shape of the spectra from these models is counter to that observed. This behavior is exemplified by the WW2 20 d model with $\eta = 1.1$ in Table 5.2 where $B - V$ is extremely red (0.74), but $U - B$ is negative (-0.16). The flat spectrum in the UV for these models (signified by a negative $U - B$) is observationally associated with bright SNe Ia such as SN 1991T and SN 1994D, rather than with dim supernovae such as SN 1991bg. In the spectrum of SN 1991bg, the trough near 4000 Å is due to Ti II (Filippenko et al., 1992b; Nugent

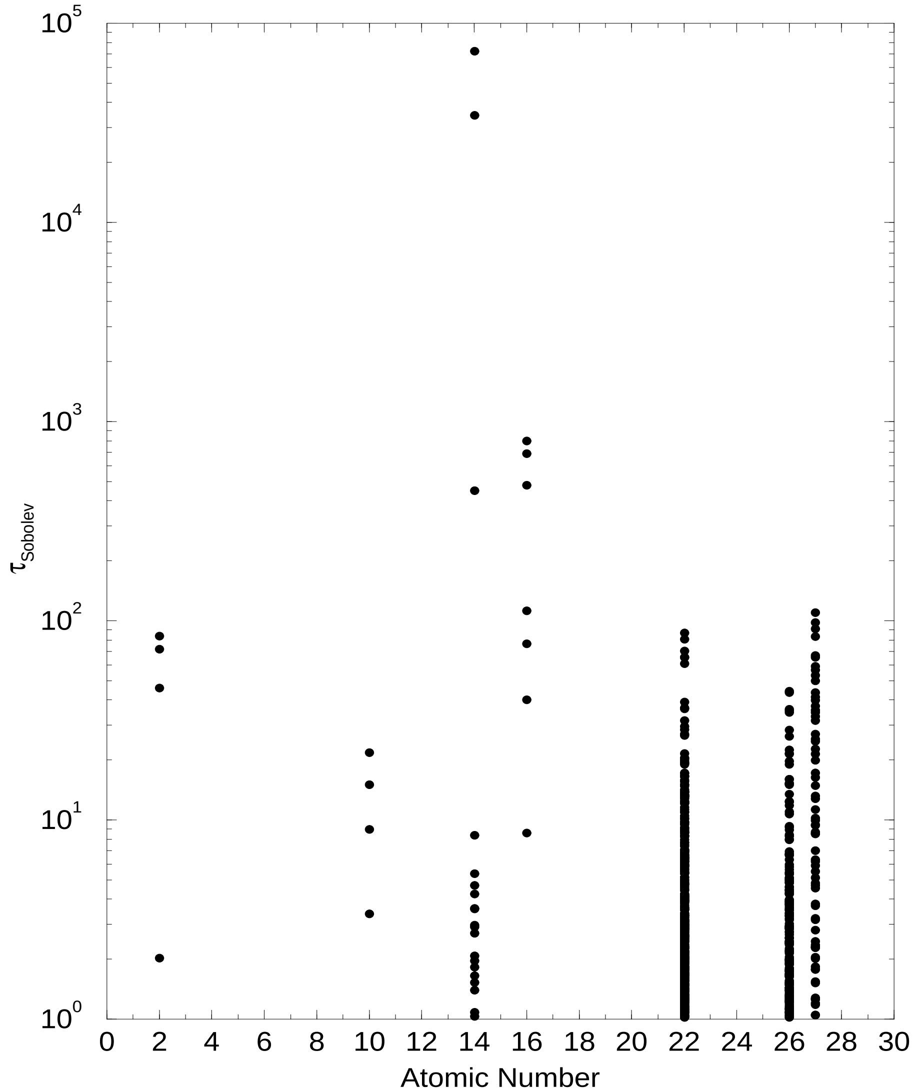

Figure 5.7: The Sobolev optical depths throughout the atmosphere of Model WW2, 20 d after explosion, with $\eta = 1.1$, as a function of atomic number for transitions in the wavelength range $5700 - 6000$ Å.

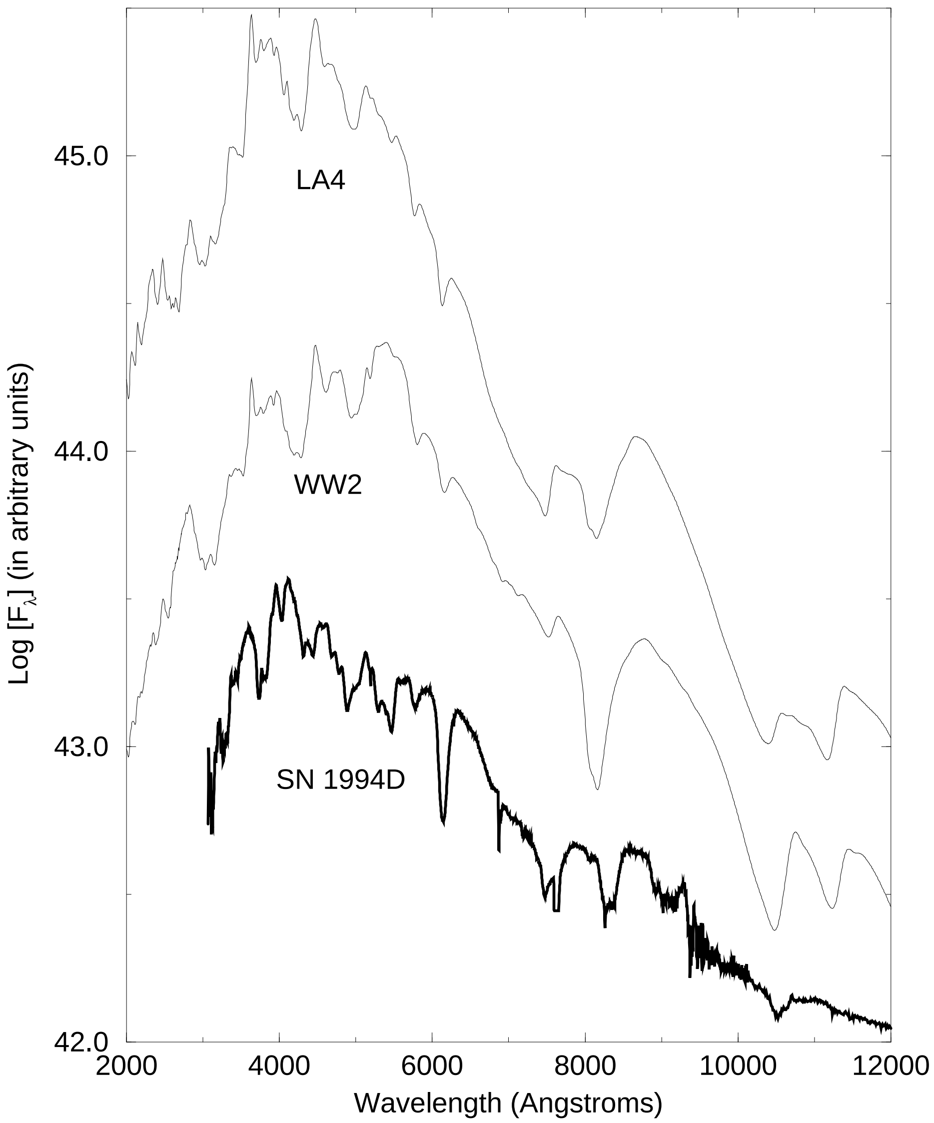

Figure 5.8: The synthetic spectra of WW2 (η = 1.1) and LA4 (η = 1.5) at 20 d compared with the observed spectrum of SN 1994D [at maximum light (Meikle et al., 1996b)].

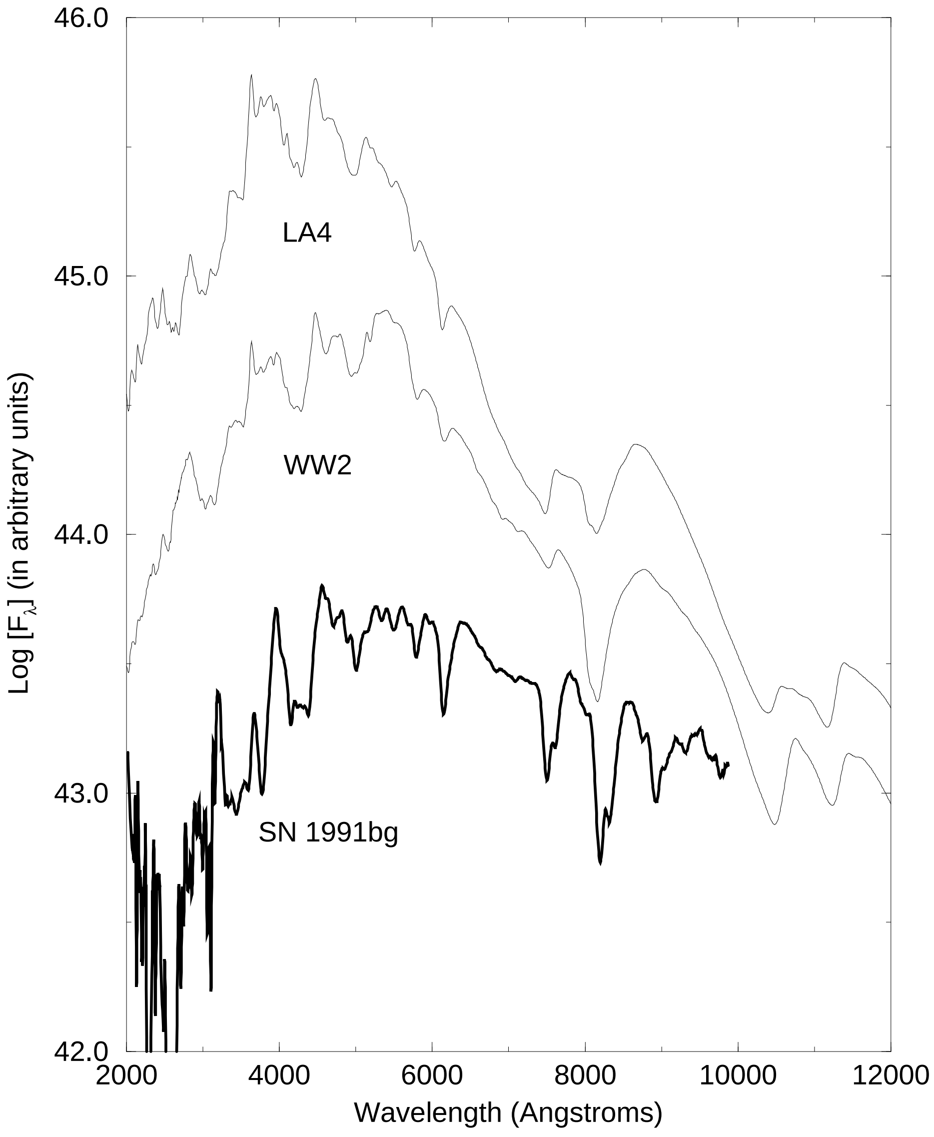

Figure 5.9: The synthetic spectra of WW2 (η = 1.1) and LA4 (η = 1.5) at 20 d compared with the observed spectrum of SN 1991bg at maximum light (Filippenko et al., 1992b; Cappellaro, Turatto, & Fernley, 1995).

et al., 1995d). In the synthetic spectra this trough is not flat enough to reproduce the observed spectrum of SN 1991bg, most likely because Ti II is confined to a small region in velocity in these models. Also, the calculated Si II and Ca II lines are very weak even at this epoch. The strength of these lines correlates inversely with the luminosity of the supernova (Nugent et al., 1995d). Weak, dim supernova like SN 1991bg have strong Si II and Ca II lines, whereas powerful, bright SNe such as 1991T, have weak lines, thus a model that hopes to fit SN 1991bg should show prominent Si II and Ca II lines.

Table 5.3 lists the relative concentration of the four most abundant species at three different velocities for each of the three models that we have examined (the models W7, WW2, and LA4 have $\eta = 1.0, 1.0, 1.5$, respectively) at 20 days after explosion. The models have very similar compositions at low velocity, a mixture of highly ionized iron-peak elements and He II. The detonation models have somewhat more He II than does the deflagration W7. In the outer parts, the composition is different. Whereas W7 has singly and doubly ionized intermediate mass elements, the helium igniters have mixtures of neutral and singly ionized helium, and doubly ionized elements just below the iron-peak (calcium and titanium). At very high velocity ($v > 20000$ km s^{-1}), the composition of W7 is mostly a mixture of C–O, while the WW2, and LA4 models are dominated by He I – II. As we have already noted the presence of intermediate mass elements at high velocity is required to fit the observed spectra.

In order to further elucidate the differences between W7 and the helium-igniters, Figure 5.10 compares the temperature and density profiles of W7 ($\eta = 1.0$) to WW2 ($\eta = 1.1$) at 20 d. The more massive W7 model has a much steeper density profile, and it is cooler on the outside. Figure 5.11 displays the Sobolev optical depth of the

Model	Velocity ($\mathrm{km\ s^{-1}}$)	Relative Concentration (ppm)			
W7	20,000	C I (2×10^5)	O II (2×10^5)	Ne II (2×10^4)	O I (1×10^4)
LA4	20,000	He II (4×10^5)	He I (9×10^4)	Ti III (6×10^3)	Ca III (4×10^3)
WW2	20,000	He II (4×10^5)	He I (2×10^5)	Ti III (7×10^3)	Ca III (6×10^3)
W7	10,000	Si III (1×10^5)	Co III (7×10^4)	S III (6×10^4)	Ca III (3×10^4)
LA4	10,000	Si III (1×10^5)	Co III (1×10^5)	S III (5×10^4)	Ni III (1×10^4)
WW2	10,000	Si III (2×10^5)	S III (1×10^5)	Ar II (1×10^4)	Ca III (1×10^4)
W7	5,000	Co IV (2×10^5)	Ni IV (7×10^4)	Fe IV (2×10^4)	He II (2×10^3)
LA4	5,000	Co IV (2×10^5)	He II (7×10^4)	Ni IV (2×10^4)	Fe IV (2×10^4)
WW2	5,000	Co IV (2×10^5)	He II (3×10^4)	Ni IV (2×10^4)	Fe IV (2×10^4)

Table 5.3: 4 Most Abundant Species for Each Model at 20 Days After Explosion. The relative concentrations by number of the four most abundant species (in parts per million) for a particular zone (labeled by its velocity). The models W7, WW2, and LA4 have $\eta = 1.0, 1.1, 1.4$, respectively.

Co II $^1D -^3 G^o$ $\lambda 2605.2$ line as a function of $\tau_{\rm std}$ for the 3 models. While W7 and WW2 display similar Sobolev optical depths in this line at depth, LA4 only has a very small region where this line is optically thick, and, near the surface where the spectrum forms, both WW2 and LA4 are transparent in this line. This is typical for the iron-peak UV lines and it makes it very difficult for the helium-detonation models to display the proper line blanketing in the UV. It is not that the iron-peak elements are not present, but rather that they are not in the proper ionization/electronic states to create strong line blanketing.

5.5 Conclusions

We have calculated very detailed NLTE synthetic spectra of hydrodynamical models for SNe Ia. We have used only symmetry considerations at the inner boundary and thus have not had to make any assumptions about the form of the flux there, the spectrum is calculated *ab-initio*. We have used a simple but accurate γ-ray transport algorithm and we have developed a reasonable parameterization of the time dependence of the γ-ray heating that can be compared with and calibrated to sophisticated radiation hydrodynamical calculations as they become available.

The Chandrasekhar-mass deflagration model W7 shows good agreement with observed normal SNe Ia and it is likely that other Chandrasekhar-mass models such as DD or PDD (Khokhlov, Müller, & Höflich, 1993) will also show reasonable agreement. While the sub-Chandrasekhar mass "helium igniter" models bear some resemblance to the sub-luminous SNe Ia typified by SN 1991bg the weakness of lines of the intermediate mass elements and the lack of the UV deficit will have to be addressed if these models are to remain as viable contenders for at least some SNe Ia.

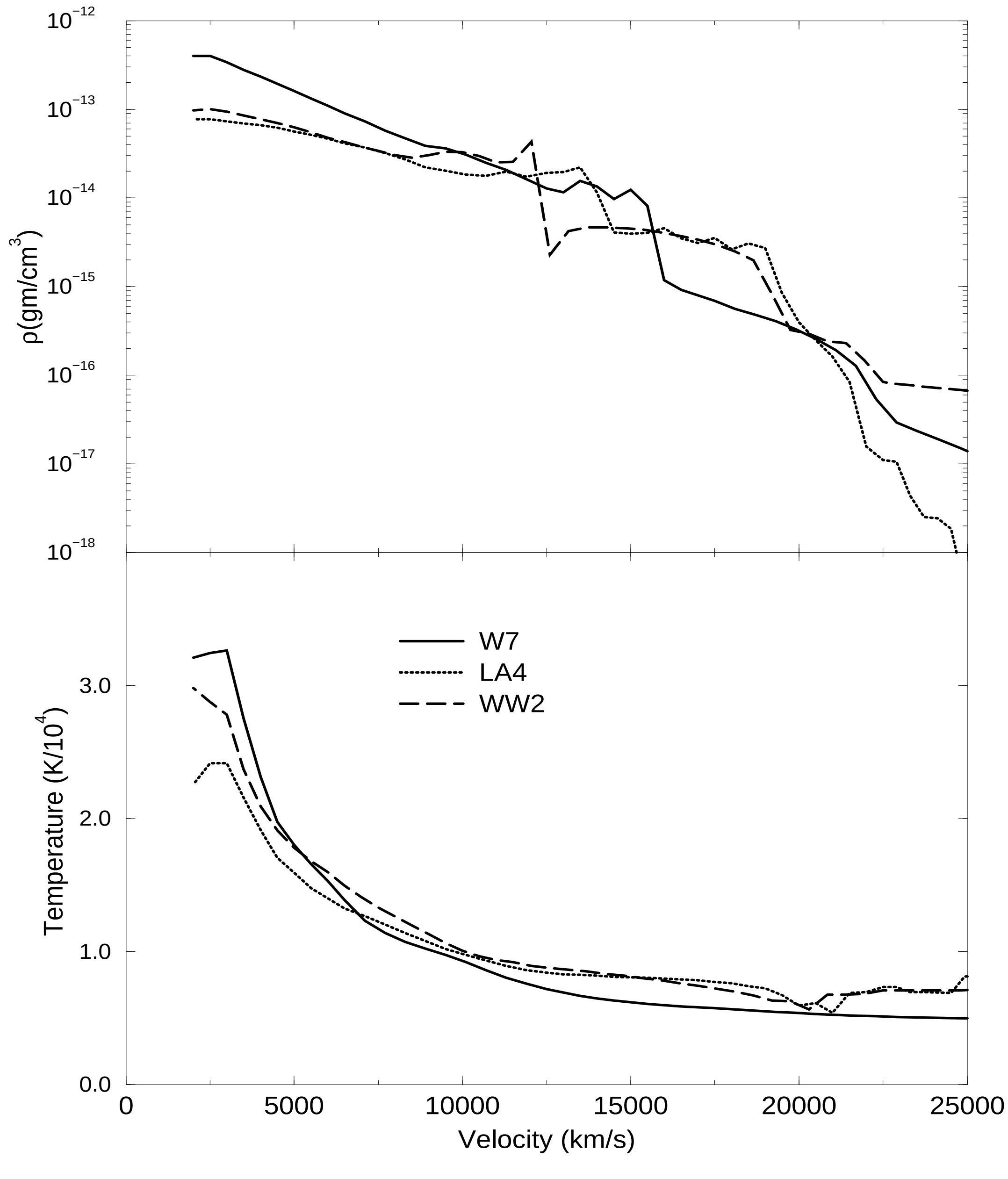

Figure 5.10: The density and temperature profiles for WW2 and W7 at 20 d, with $\eta = 1.1, 1.0$ respectively. The "glitches" in the density and temperature occur at the edge of the burning fronts and represent real changes in model structure.

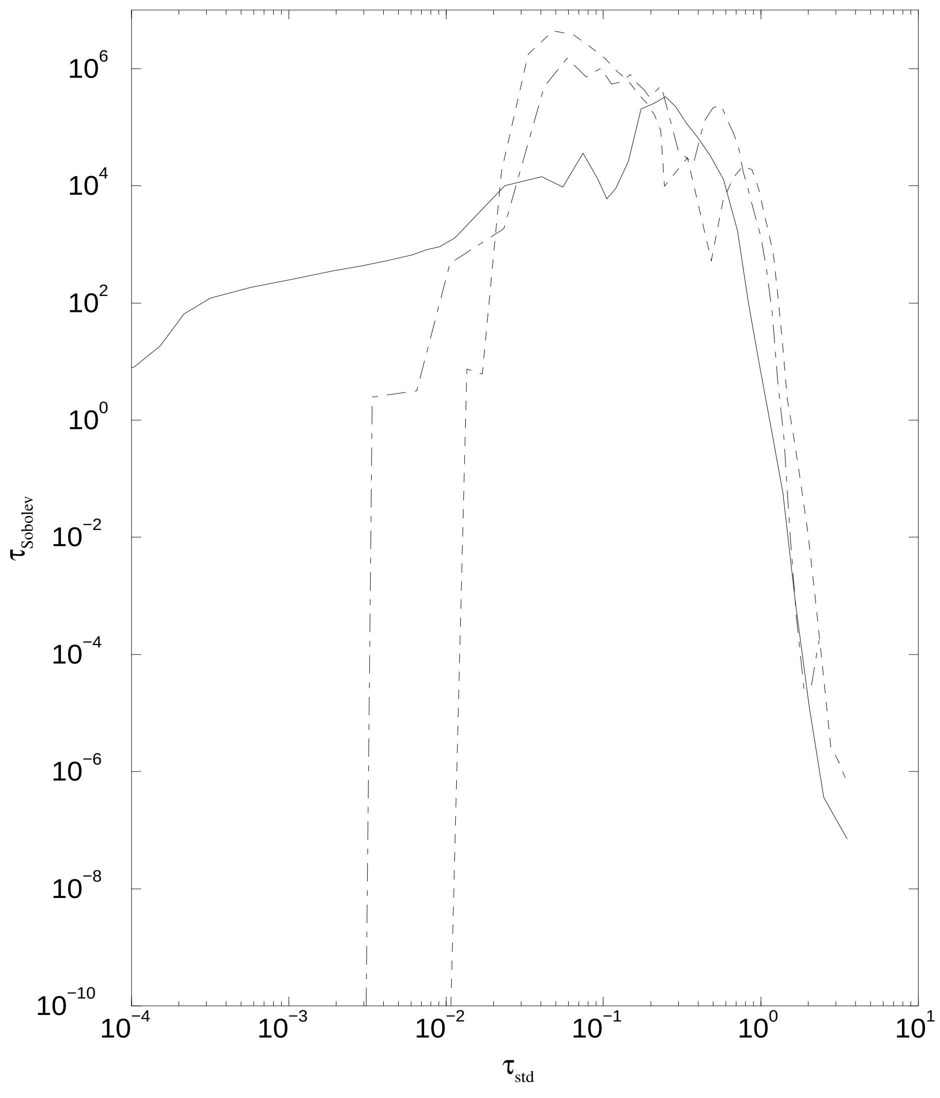

Figure 5.11: The Sobolev optical depth of the Co II $^1D - ^3G^o$ $\lambda 2605.2$ lin as a function of τ_{std} for the 3 models listed in Table 5.3. The solid line denotes the W7 model, the dashed line WW2, and the dot-dashed line LA4. Note that τ_{Sobolev} is a purely local quantity and hence is not necessarily monotonic.

Chapter 6

NLTE vs. LTE

6.1 Abstract

We finish up this thesis with a look at the first word in the title, 'NLTE'. NLTE stands for non-local thermodynamic equilibrium. It basically represents all processes which can effect the level populations of an ionic species which can not be explained by the local temperature through the Saha and Boltzmann equations. This includes both the impinging radiation field and non-thermal ionization. Our focus will be concentrated in two areas. First, how does using an LTE approximation (in contrast with a reasonably full NLTE calculation) effect the resultant model. Second, what do the NLTE calculations tell us about the features in the spectra. In the end we wish to convince the reader of the necessity of performing NLTE calculations and their usefulness in the interpretation of the spectra of SNe Ia near maximum light.

6.2 Differences

To explore the differences between LTE and NLTE calculations we will look no further than the W7 model at 20 days which is seen in Chapter 5. This calculation has (by particle number) the majority of the atmosphere in NLTE. Most importantly it has both Fe II and Co II in NLTE which not only have several strong lines in the spectra of SNe Ia but also have a large number of weaker lines (in the millions) which, taken as a group, control the overall shape of the spectra. This model was calculated with a nebular inner-boundary condition. The two LTE models which we consider do not incorporate this inner-boundary condition. These models also make use of a constant scattering albedo, $\alpha = 0.1$.

Model	$\mathrm{M_{bol}}$	M_U	M_B	M_V	M_R
NLTE	-18.71	-19.12	-18.93	-18.94	-18.83
LTE #1	-18.78	-19.37	-18.92	-18.92	-18.84
LTE #2	-18.38	-18.62	-18.46	-18.69	-18.61

Table 6.1: Magnitudes for the NLTE and LTE models.

In Figure 6.1 we see a plot of the NLTE calculation vs. two LTE models. Table 6.1 lists the UBVRI and bolometric magnitudes for each. What should stick out immediately is how neither LTE model correctly reproduces the colors in the NLTE model, even though they span a large range in absolute bolometric magnitude. Model LTE #1 is clearly to bright in the UV while it matches the optical rather well up to 7000 Å. LTE #2 is a decent match in the far UV (up to 3500 Å) though it is very underluminous in the optical and IR. The reason behind this can be seen in Figure 6.2. Here the percentage temperature difference between each LTE model and the NLTE model is plotted vs. velocity. Bracketing a 5% range in temperature difference one can see that LTE #1 is a better match at lower velocities (5,000 to 12,500 km/s) and LTE #2 matches better at higher velocities (12,500 to 25,000 km/s). Since the UV is optically thick until the very outer regions of the atmosphere, it makes sense that the model which matches temperature structure better in this range, LTE #2, will fit the spectrum better in the UV. Likewise, the optical part of the spectrum (since it becomes thin at much lower velocities) will be

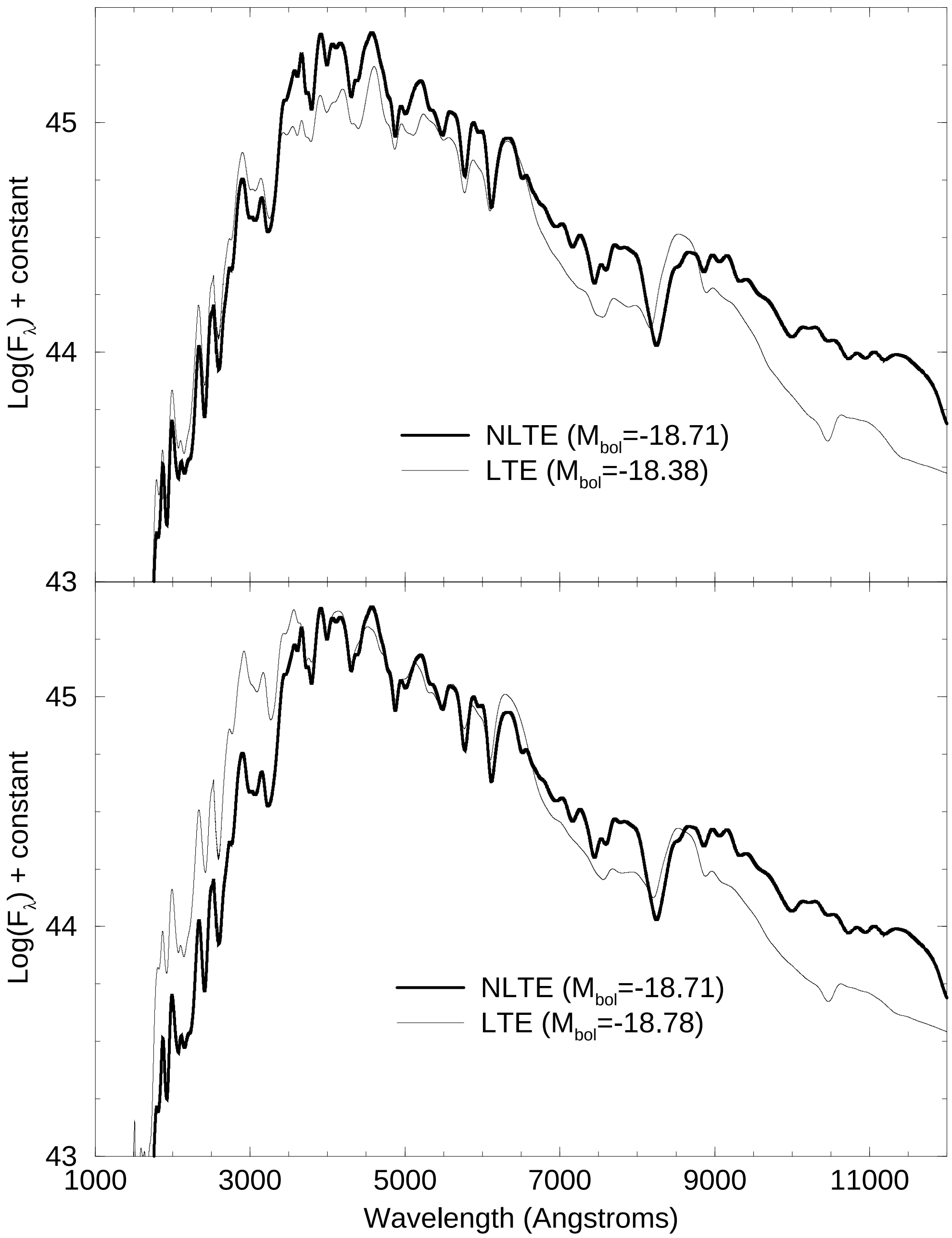

Figure 6.1: A comparison of LTE and NLTE spectra.

better matched by model LTE #1, since it more correctly matches the temperature structure at depth.

In Figure 6.3 we present the b_i's for the strongest lines for each element in the optical region of the spectrum. The transitions considered (labeled by their approximate wavelengths) are as follows: C I – 9100 Å, O I – 7780 Å, Mg II – 4490 Å, S II – 5650 Å, Si II – 6350 Å, Ca II – 3940 Å, Fe II – 5180 Å and Co II – 4170 Å. The b_i's (as we present them here) are the ratio of the NLTE level populations to the LTE level populations given the NLTE ionization. It is quite obvious from this figure that most of the species are far from LTE, even at depth. Of particular note is the O I line which is far from LTE everywhere in the atmosphere and was impossible to fit in our earlier models where we considered it only in LTE (see Nugent et al. (1995a)). One can also see how Si II departs far from LTE (especially at depth). This feature is especially important for SNe Ia since it's spectral signature is used to classify these events.

6.3 Line Identifications

We end the thesis with a brief section on line identification in SNe Ia. While several strong lines are readily apparent in the near maximum light spectra, it will become quite obvious from the next few graphs that, in general, a spectrum's shape and features are controlled by the blending of many thousands (even millions) of weak lines. This is especially true of the iron peak elements.

Figures 6.4 through 6.8 display the sum of the Sobolev optical depths, in 10 Å̃bins, for each ionic species throughout the line forming region. The wavelengths have been blueshifted by 10,000 km/s (roughly the photospheric velocity) in order to match up better with the major features in the synthetic spectra rather than being at the

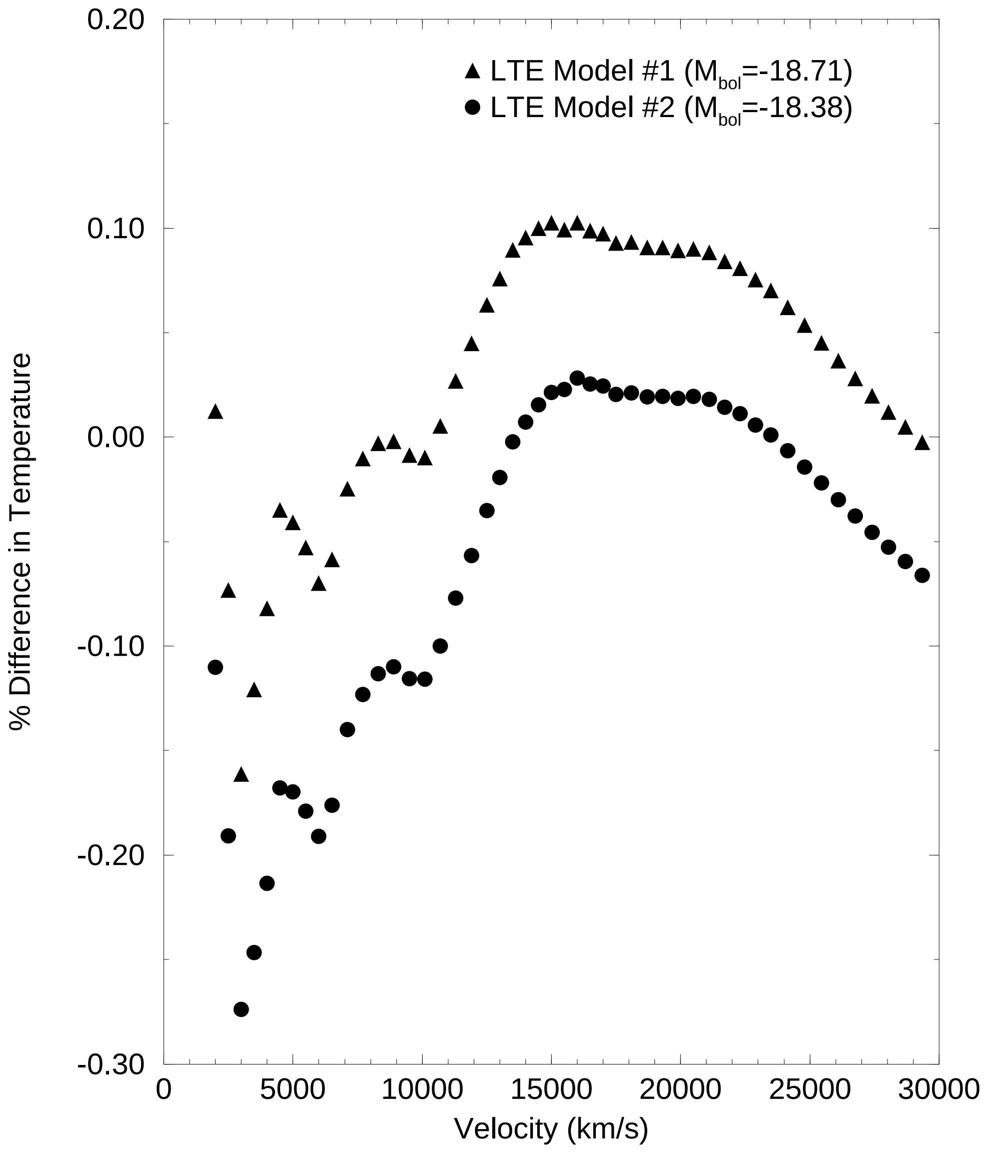

Figure 6.2: The percentage difference in temperature between the NLTE and LTE spectra.

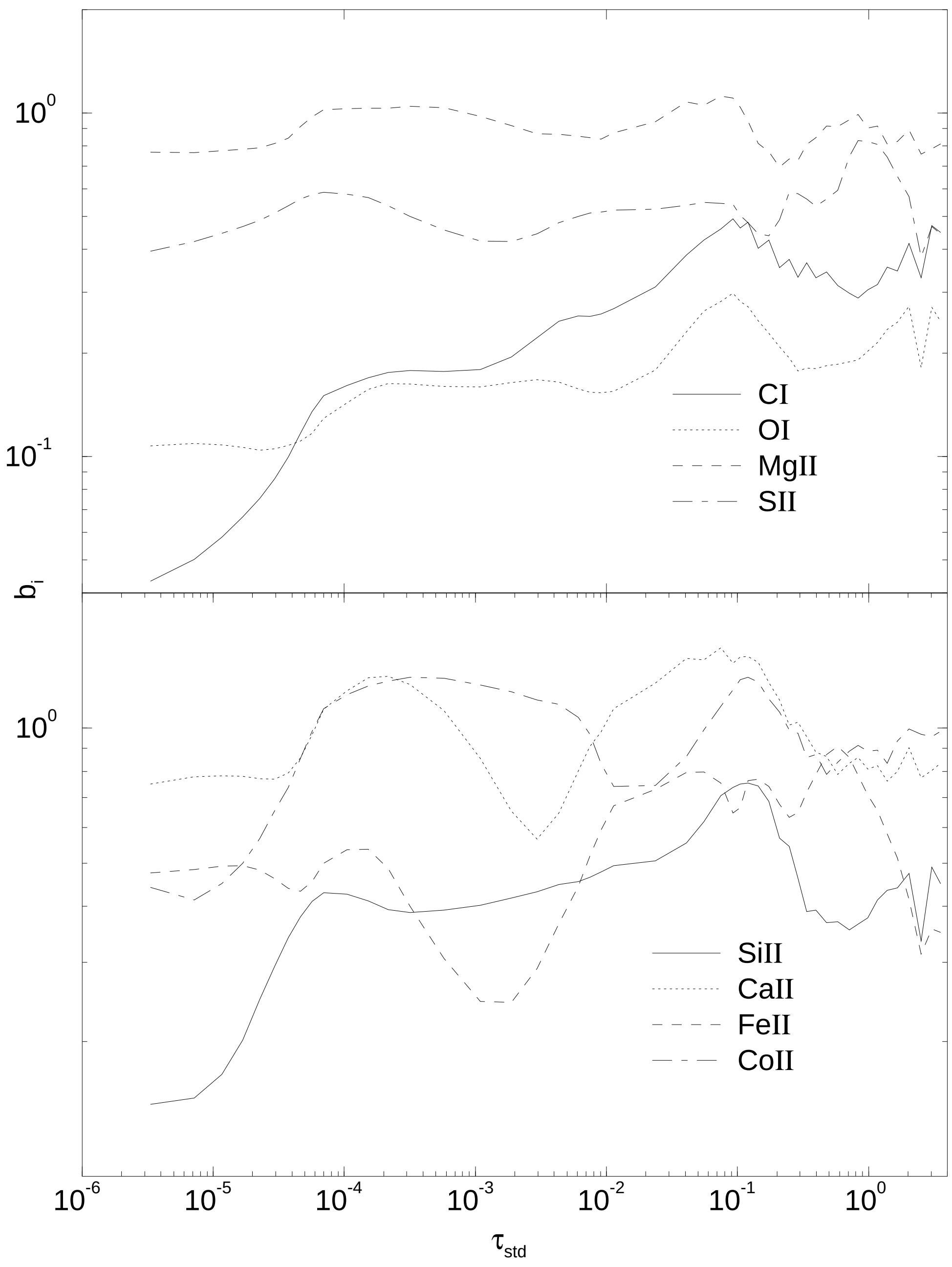

Figure 6.3: The b_i's for the NLTE model. The transitions considered are as follows: C I – 9100 Å, O I – 7780 Å, Mg II – 4490 Å, S II – 5650 Å, Si II – 6350 Å, Ca II – 3940 Å, Fe II – 5180 Åand Co II – 4170 Å.

rest wavelength. All the standard line identifications stick out tremendously having optical depths approaching 10^{6-7}. One can easily match up the strong features associated with the Ca II H&K lines and infrared triplet, the Si II features at either side of 6000 Å (though note how Na I makes its presence known in the bluer of the lines), the S II 'W' feature at 5400 Å and the several strong Mg II features stretching from 2800 Å to the near infrared.

The major players though are Ti II, Fe II and Co II. Their presence in the UV is what directly controls the overall shape of the spectrum. The line blanketing they produce in the UV is what takes a relatively Planckian spectrum in the IR and optical and hacks it off at 4000 Å. In addition, one can see that Fe II is strong throughout the entire spectrum with Sobolev optical depths greater than 10^2 all the way to 1.0 μ. In future work we will examine how the strengths of these features change as a function of time and overall luminosity, paying particular attention to the Ti II lines near 4400 Å which make a much stronger appearance in the dimmer SNe Ia.

In conclusion, we have demonstrated both the necessity and usefulness of performing NLTE spectrum synthesis calculations of SNe Ia. We have shown how these calculations can be used for abundance determinations and line identifications, the acceptance or rejection of a particular model and as an independent (and purely physical-based) way to determine the distance to a supernova. Though the work in this field is far from complete, this thesis has made great strides into the analysis of SNe Ia and has provided a means to tackle many of the remaining questions.

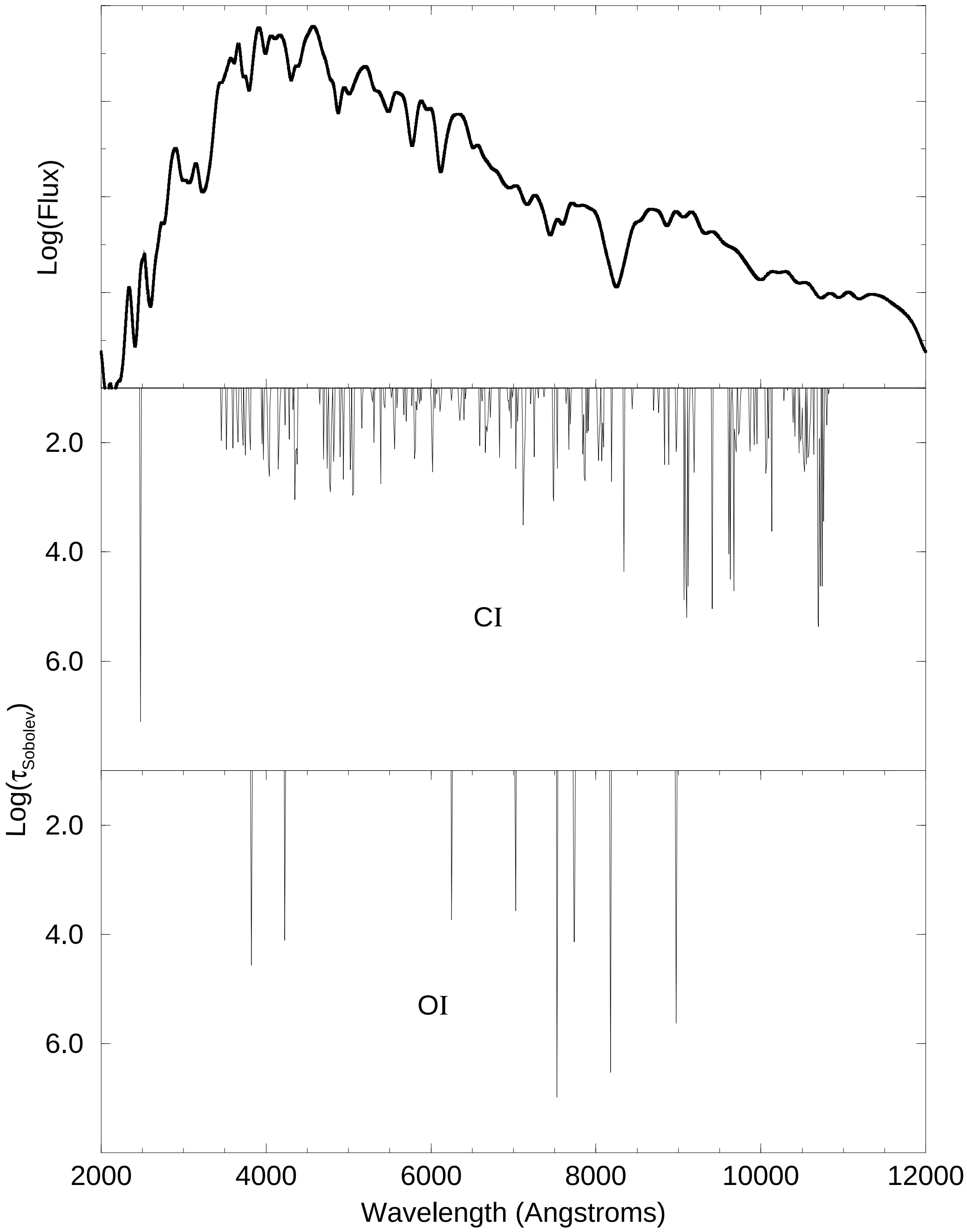

Figure 6.4: The Sobolev optical depths for O I and C I throughout the line forming region in the atmosphere.

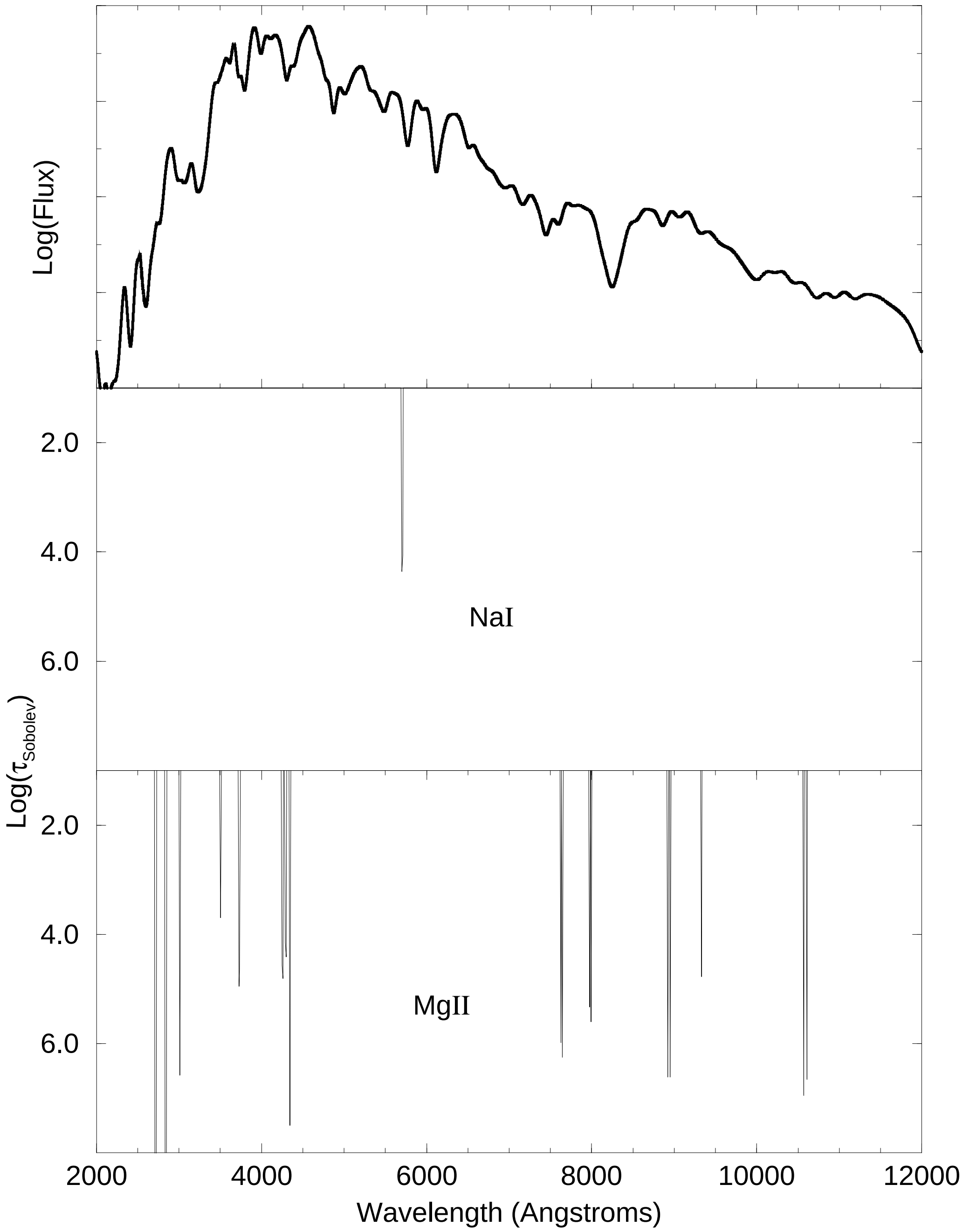

Figure 6.5: The Sobolev optical depths for Na I and Mg II throughout the line forming region in the atmosphere.

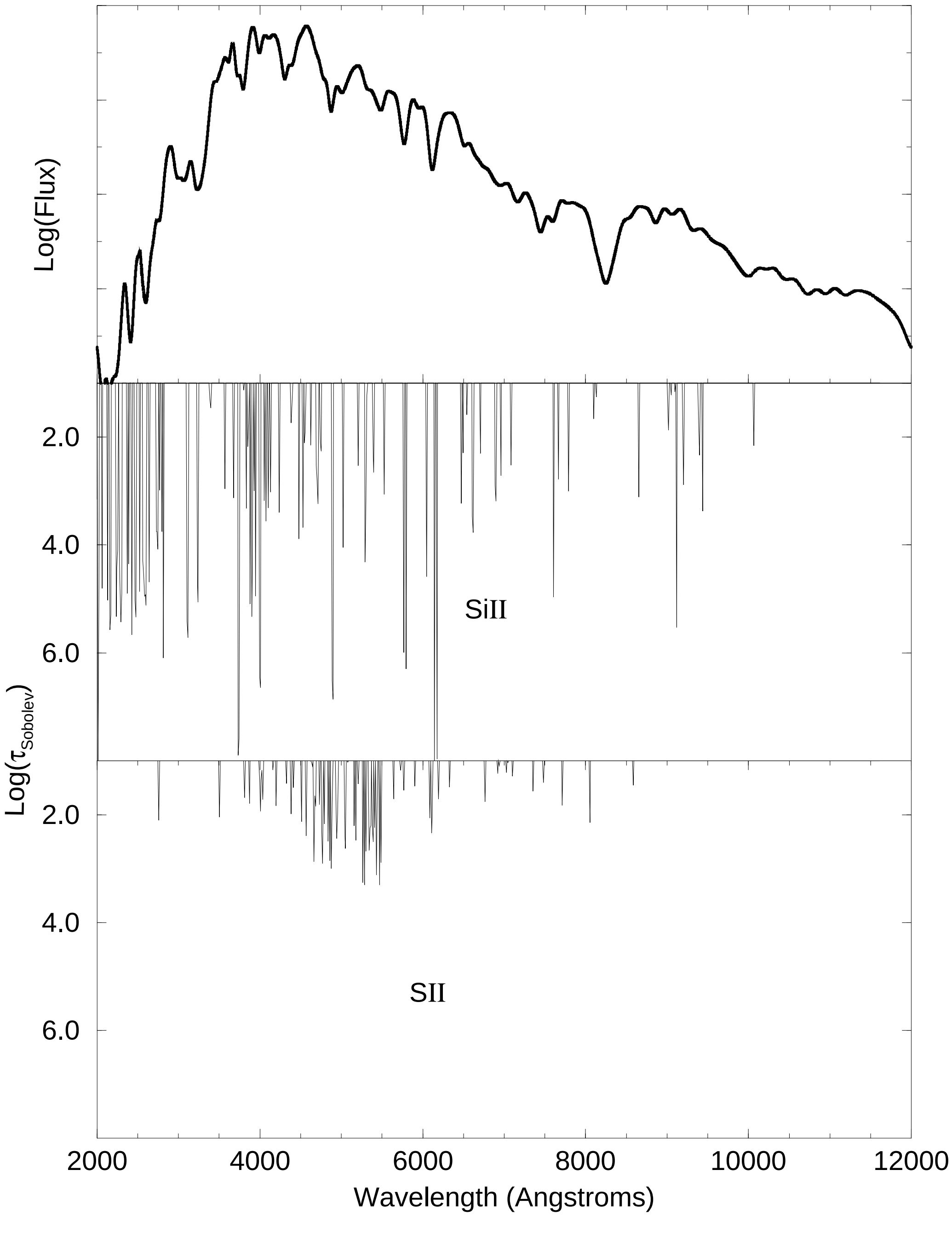

Figure 6.6: The Sobolev optical depths for Si II and S II throughout the line forming region in the atmosphere.

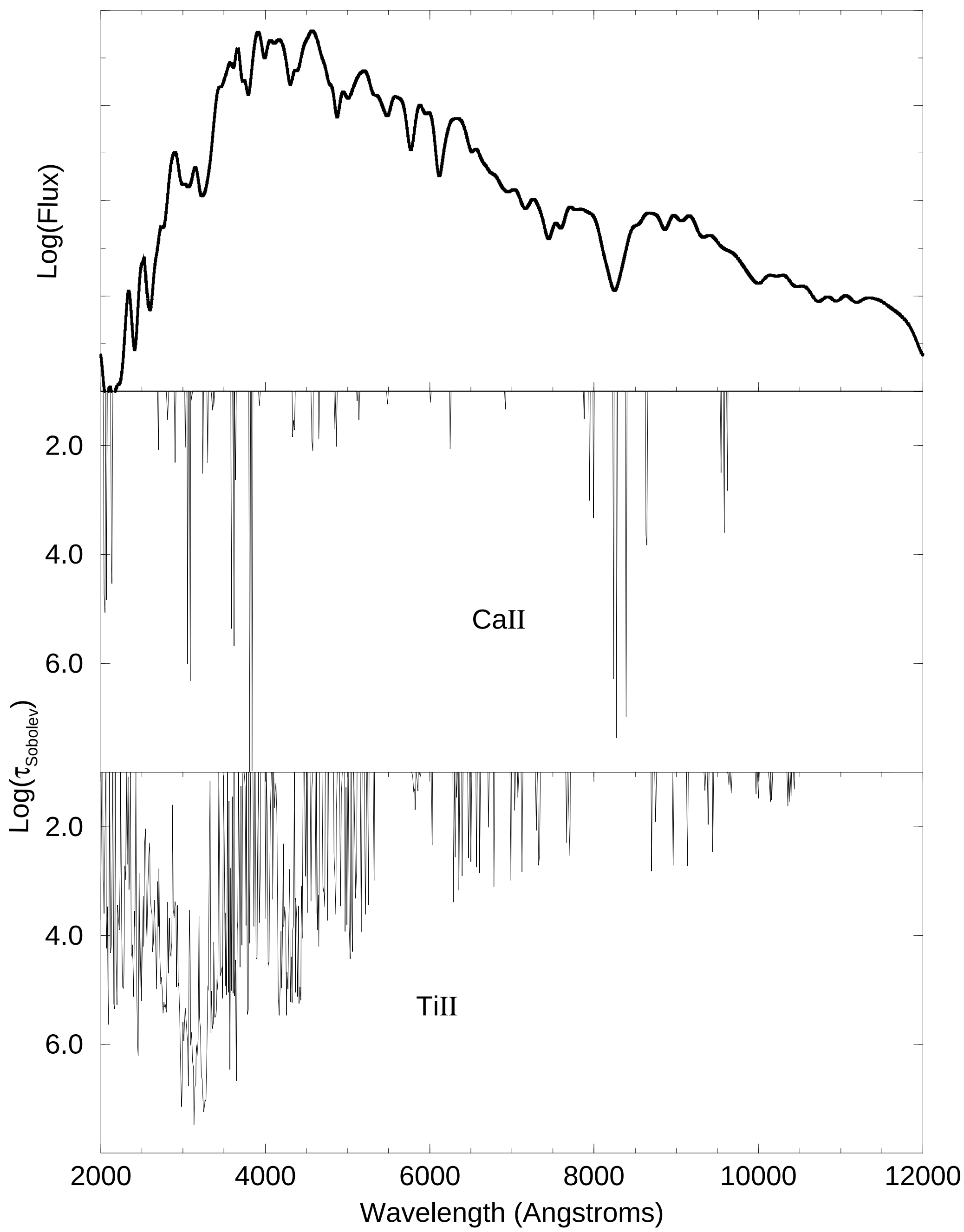

Figure 6.7: The Sobolev optical depths for Ca II and Ti II throughout the line forming region in the atmosphere.

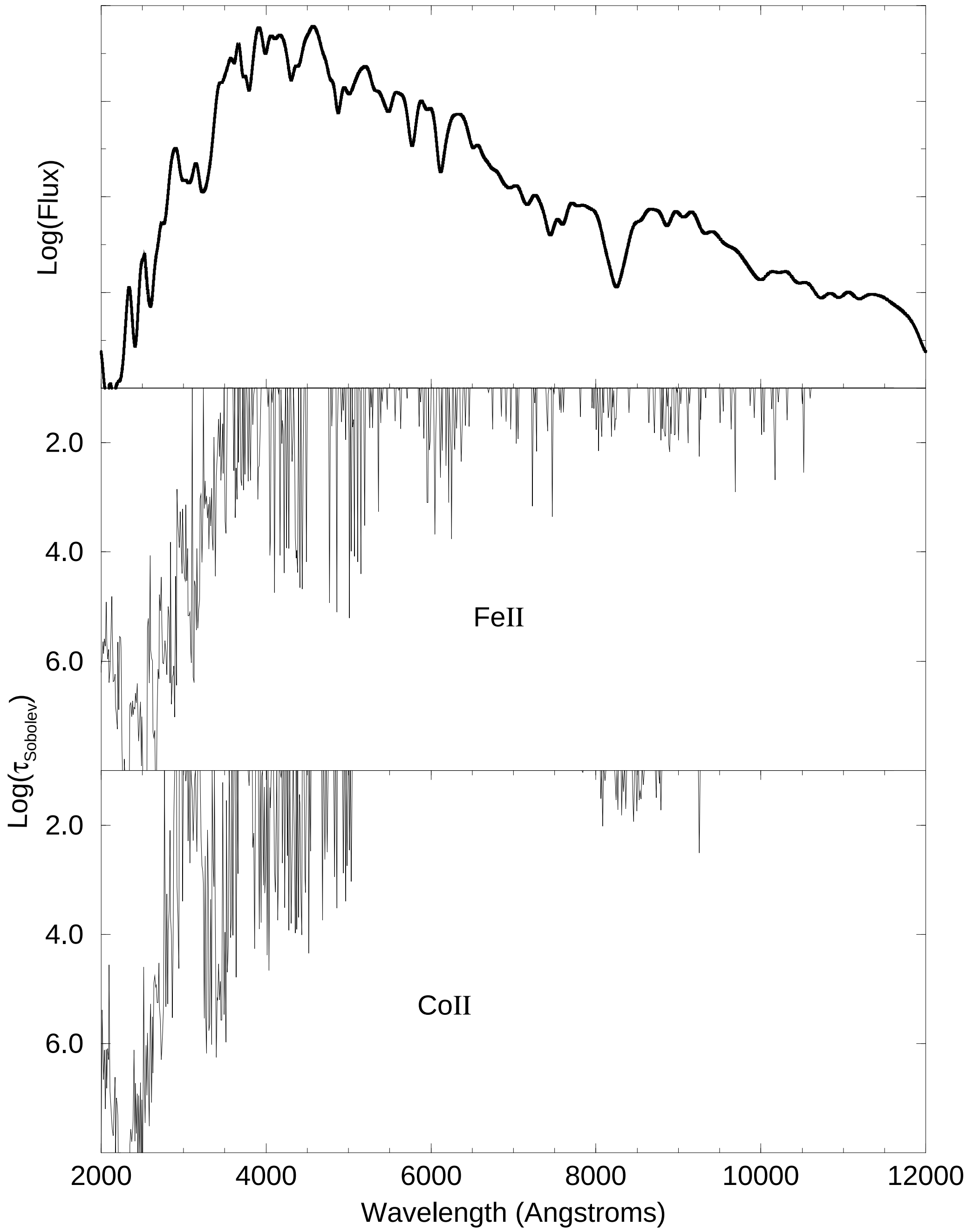

Figure 6.8: The Sobolev optical depths for Fe II and Co II throughout the line forming region in the atmosphere.

Bibliography

Allard, F., Hauschildt, P. H., Miller, S., & Tennyson, J. 1994, apjlet, 426, L39

Arnett, W. D. 1982, ApJ, 253, 785

Arnett, W. D., Branch, D., & Wheeler, J. C. 1985, Nature, 314, 337

Baade, W. 1926, Astr. Nach., 228, 359

Baron, E., Young, T., & Branch, D. 1993, ApJ, 409, 471

Baron, E., Hauschildt, P. H., & Branch, D. 1994, ApJ, 426, 334

Baron, E., Hauschildt, P. H., Branch, D., Austin, S., Garnavich, P., Ann, H. B., Wagner, R. M., Filippenko, A. V., Matheson, T., & Liebert, J. 1995, ApJ, 441, 170

Baron, E., Hauschildt, P. H., Nugent, P., & Branch, D. 1996, MNRAS, in press

Birkinshaw, M., & Hughes, J. P. 1994, ApJ, 420, 33

Branch, D. 1992, ApJ, 392, 35

Branch, D., et al. 1981a, ApJ, 248, 1076

Branch, D., et al. 1983a, ApJ, 270, 123

Branch, D., et al. 1995a, in preparation

Branch, D., & Khokhlov, A. 1995, Phys. Reports, in press

Branch, D., Falk, S. W., McCall, M. L., Rybski, P., Uomoto, A. K., & Wills, B. J. 1981b, ApJ, 244, 780

Branch, D., Lacy, C. H., McCall, M. L., Sutherland, P. G., Uomoto, A., Wheeler, J. C., & Wills, B. J. 1983b, ApJ, 270, 123

Branch, D., Doggett, J., Nomoto, K., & Thielemann, F. 1985, ApJ, 294, 619

Branch, D., Pauldrach, A., Puls, J., Jeffery, D., & Kudritzki, R. 1991. In Proceedings of the ESO/EPIC Workshop on SN 1987A and other Supernovae, I. J. Danziger and K. Kjär, editors, Munich: ESO, page 437

Branch, D., Fisher, A., & Nugent, P. 1993a, AJ, 106, 2383

Branch, D., Fisher, A., & Nugent, P. 1993b, AJ, 106, 2383

Branch, D., Fisher, A., Herczeg, T., Miller, D., & Nugent, P. 1994, ApJ, 421, L87

Branch, D., Livio, M., Youngelson, L., F.Boffi, & Baron, E. 1995b, PASP, 107, 1019

Brent, R. P. 1973. Algorithms for Minimization without Derivatives, Englewood Cliffs, NJ: Prentice Hall

Cappellaro, E., Turatto, M., & Fernley, J. 1995. IUE - ULDA Access Guide No. 6: Supernovae, The Netherlands: ESA

Castor, J. I. 1970, MNRAS, 149, 111

Colgate, S., Petschek, A., & Kriese, J. 1980, ApJ (Letters), 237, L81

Dahle, H., Maddox, S. J., & Lilje, P. B. 1994, ApJ (Letters), 435, L79

Eastman, R., & Kirshner, R. P. 1989, ApJ, 347, 771

Filippenko, A. V., et al. 1992a, AJ, 104, 1543

Filippenko, A. V., et al. 1992b, AJ, 104, 1543

Fisher, A., Branch, D., , Höflich, P., & Khokhlov, A. 1995, ApJ (Letters), 447, L73

Freedman, W. L., et al. 1994, Nature, 371, 757

Garvey, R. H., & Green, A. E. S. 1976, Phys. Rev. A, 14, 946

Hamuy, M., Walker, A. R., Suntzeff, N. B., Gigoux, P., Heathcote, S. R., & Phillips, M. M. 1992, PASP, 104, 533

Hamuy, M., Phillips, M. M., Maza, J., Suntzeff, N. B., Schommer, R. A., & Aviles, R. 1995, AJ, 109, 1

Hamuy, M., Phillips, M. M., Maza, J., Suntzeff, N. B., Schommer, R. A., & Aviles, R. 1996, AJ, in preparation

Harkness, R. 1991a. In Proceedings of the ESO/EPIC Workshop on SN 1987A and other Supernovae, I. J. Danziger and K. Kjär, editors, Munich: ESO, page 447

Harkness, R. 1991b. In Supernovae, S. E. Woosley, editor, New York: Springer-Verlag, page 454

Hauschildt, P. H. 1992a, JQSRT, 47, 433

Hauschildt, P. H. 1992b, ApJ, 398, 224

Hauschildt, P. H. 1993, JQSRT, 50, 301

Hauschildt, P. H., & Baron, E. 1995, JQSRT, 54, 987

Hauschildt, P. H., & Ensman, L. 1994, ApJ, 424, 905

Hauschildt, P. H., Wehrse, R., Starrfield, S., & Shaviv, G. 1992, ApJ, 393, 307

Hauschildt, P. H., Starrfield, S., Austin, S., Wagner, R. M., Shore, S. N., & Sonneborn, G. 1994, ApJ, 422, 831

Hauschildt, P. H., Starrfield, S., Shore, S. N., Allard, F., & Baron, E. 1995, ApJ, 447, 829

Hauschildt, P. H., Baron, E., & Allard, F. 1996, J. Comp. Phys., submitted

Hauschildt, P. H., Baron, E., Starrfield, S., & Allard, F. 1996, ApJ, 462, 386

Höflich, P. 1995, ApJ, 443, 89

Höflich, P., & Khokhlov, A. 1996, ApJ, 457, 500

Höflich, P., Dominik, C., Khokhlov, A., Müller, E., & Wheeler, J. C. 1995, Ann. New York Acad. Sci., in press

Hogan, C. J. 1994, Nature, 371, 374

Jacoby, G. H. 1994, Nature, 371, 741

Jeffery, D., Leibundgut, B., Kirshner, R. P., Benetti, S., Branch, D., & Sonneborn, G. 1992, ApJ, 397, 304

Jones, M., et al. 1993, Nature, 365, 320

Khokhlov, A. 1991a, A&A, 245, 114

Khokhlov, A. 1991b, A&A, 245, L25

Khokhlov, A. 1995, private communication

Khokhlov, A., Müller, E., & Höflich, P. 1992, A&A, 270, 223

Khokhlov, A., Müller, E., & Höflich, P. 1993, A&A, 270, 223

Khokhlov, A., Müller, E., & Höflich, P. 1994, A&A, 270, 223

Kirshner, R., et al. 1993, ApJ, 415, 589

Kirshner, R. P., & Kwan, J. 1974, ApJ, 193, 27

Kurucz, R. 1993, CDROM No. 1 Atomic Data for Opacity Calculations, unpublished

Leibundgut, B., Tammann, G. A., Cadonau, R., & Cerrito, D. 1991, A&AS, 89, 537

Livne, E., & Arnett, W. D. 1995, ApJ, 452, 62

Livne, E., & Glasner, A. S. 1990, ApJ, 361, 244

Livne, E., & Glasner, A. S. 1991, ApJ, 370, 272

Marvin, H., & Perlmutter, S. 1989, IAU Circ. No. 4727

Mazzali, P. A., & Lucy, L. B. 1993, A&A, 279, 447

Mazzali, P. A., Lucy, L. B., Danziger, I. J., Gouiffes, C., Cappellaro, E., & Turatto, M. 1993, A&A, 269, 423

Meikle, W. P. S., et al. 1996a, MNRAS, 281, 263

Meikle, W. P. S., et al. 1996b. In Proceedings of the NATO ASI Conference on Thermonuclear Supernovae, R. Canal, R. Ruiz-Lapuente, and J. Isern, editors, Dordrecht: Kluwer

Mihalas, D. 1978. Stellar Atmospheres, San Francisco: W. H. Freeman and Co., second edition

Miller, D., et al. 1995, ApJ, in preparation

Nomoto, K., Thielemann, F., & Yokoi, K. 1984, ApJ, 286, 644

Nugent, P., Baron, E., Hauschildt, P., & Branch, D. 1995a, ApJ (Letters), 441, L33

Nugent, P., Branch, D., Baron, E., Fisher, A., Vaughan, T., & Hauschildt, P. 1995b, Phys. Rev. Lett., 75, 394

Nugent, P., Branch, D., Baron, E., Fisher, A., Vaughan, T., & Hauschildt, P. 1995c, Phys. Rev. Lett. Erratum, 75, 1874

Nugent, P., Phillips, M., Baron, E., Branch, D., & Hauschildt, P. 1995d, ApJ (Letters), 455, L147

Nugent, P. E. 1996. Ph.D. thesis, University of Oklahoma

Patat, F., et al. 1996, MNRAS, 278, 111

Phillips, M. M. 1993a, ApJ, 413, L105

Phillips, M. M. 1993b, ApJ (Letters), 413, L105

Phillips, M. M., & other 1987, PASP, 99, 592

Phillips, M. M., & other 1992, AJ, 103, 1632

Pierce, M. 1994, ApJ, 430, 53

Pierce, M. J., et al. 1994, Nature, 371, 385

Pistinner, S., Shaviv, G., Hauschildt, P. H., & Starrfield, S. 1995, apj, in preparation

Pskovskii, Y. 1977, Soviet Astron., 21, 675

Pskovskii, Y. 1984, Soviet Astron., 28, 658

Richmond, M. W., et al. 1995, AJ, 109, 2121

Riess, A. G., Press, W. H., & Kirshner, R. P. 1995, ApJ, 438, L17

Saha, A., Labhardt, L., Schwengeler, H., Macchetto, F. D., Panagia, N., Sandage, A., & Tammann, G. 1994, ApJ, 425, 14

Saha, A., Sandage, A., Labhardt, L., Schwengeler, H., Tammann, G., Panagia, N., & Macchetto, F. D. 1995, ApJ, in press

Sandage, A., & Tammann, G. 1995, ApJ, in press

Sandage, A., & Tammann, G. A. 1993, ApJ, 415, 1

Schaefer, B. 1995, ApJ (Letters), 449, L9

Schmidt, B. P., Kirshner, R., & Eastman, R. 1992, ApJ, 395, 366

Suntzeff, N. 1992. In I.A.U. Colloquium 145, Supernovae and Supernova Remnants, R. McCray, editor, Cambridge: Cambridge University Press. in preparation

Sutherland, P., & Wheeler, J. C. 1984, ApJ, 280, 282

Swartz, D. 1991, ApJ, 373, 604

Swartz, D., Sutherland, P., & Harkness, R. 1995, ApJ, 446, 766

Tonry, J. 1994, private communication

Tonry, J. 1996, ApJ, in press

Tutukov, A., Yungelson, L., & Iben, I. 1992, ApJ, 396, 197

Vaughan, T. E., Branch, D., Miller, D. L., & Perlmutter, S. 1995, ApJ, in press

Vaughan, T. E., Branch, D., & Perlmutter, S. 1995, ApJ, in preparation

Wells, L. A., et al. 1994, AJ, 108, 2233

Wheeler, J. C., Swartz, D. A., & Harkness, R. P. 1993, Physics Reports, 227, 113

Wheeler, J. C., Harkness, R., & Khokhlov, A. 1995, Phys. Reports, 256, 211

Woosley, S. E. 1991. In Gamma-Ray Line Astrophysics, P. Durouchoux and N. Prantzos, editors, New York: AIP, page 270

Woosley, S. E., & Weaver, T. A. 1994, ApJ, 423, 371

Young, T. R. 1994. Ph.D. thesis, University of Oklahoma

Young, T. R., Baron, E., & Branch, D. 1993. In First Symposium on Nuclear Physics in the Universe, M. Strayer, editor, Singapore: World Scientific, page 399

Young, T. R., Baron, E., & Branch, D. 1995, ApJ (Letters), 449, L51

Appendix A

γ-ray Transport in Type Ia Supernovae

In order to solve the rate equations in a consistent manner, PHOENIX must include the effects of non-thermal ionization. In Type Ia supernovae the non-thermal ionization is a result of the fast electrons produced when Ni^{56} and Co^{56} emit γ-rays as they decay radioactively and these γ-rays transfer their energy to the electrons in the atmosphere via Compton scattering.

Following in the footsteps of Sutherland & Wheeler (1984), we have developed a γ-ray transport code for SNe Ia. Their method is based on a purely absorptive, gray opacity and has been shown to be accurate to within 10% in the deposition function for a wide variety of supernovae models (up to 1200 days after explosion) when compared to more elaborate Monte Carlo methods. The reason this approach has been taken, as opposed to a Monte Carlo calculation, is for the sole purpose of computational expediency. A typical γ-ray deposition calculation for a SNe Ia requires approximately 15 minutes on an IBM RISC workstation, a comparable Monte Carlo Calculation takes over 24 hours. Since one would like to produce several model atmospheres in one day, this time constraint rules out the Monte Carlo approach.

We can break down the geometry of the problem as follows. Taking an arbitrary point in the atmosphere, of mass $dm = \rho dAdl$ (ρ is the density and $dAdl$ is the volume), the rate of deposition of energy at this point due to the source is

$$ds_{dep} = s(\mathbf{r})\kappa_\gamma \rho dl \frac{dA}{4\pi r^2} e^{-\tau(\mathbf{r})} \tag{A.1}$$

where the source is at $\mathbf{r}$ emitting γ-ray energy at the rate $s(\mathbf{r})$ ergs g^{-1} s^{-1}. κ_γ is the γ-ray absorption opacity and to a very good approximation has been found to be equal to $0.06Y_e$ (where Y_e is the total number of electrons per baryon) from the work of Colgate, Petschek, & Kriese (1980)). $\tau(\mathbf{r})$ is the γ-ray optical depth and is defined as follows:

$$\tau(\mathbf{r}) = \int_0^{\mathbf{r}} \kappa_\gamma \rho(s) ds. \tag{A.2}$$

The source $s(\mathbf{r})$ varies in time in accord with the exponential decay of Ni^{56} and Co^{56} and is defined by:

$$s = 3.90 \times 10^{10} e^{-\gamma_{Ni} t} + 6.78 \times 10^9 (e^{-\gamma_{Co}} - e^{-\gamma_{Ni}}) \tag{A.3}$$

where $\gamma_{Ni} = 1.32 \times 10^{-6}$ s^{-1} and $\gamma_{Co} = 1.02 \times 10^{-7}$ s^{-1} are the decay rates. The dimensionless deposition function is obtained by dividing dm and integrating over the radioactive source region:

$$d = \frac{\kappa_\gamma}{4\pi} \int d^3 r \frac{1}{r^2} e^{-\tau(\mathbf{r})} \rho(\mathbf{r}). \tag{A.4}$$

Fig. A.1 is a rough schematic breakdown of how the atmosphere is set up for the absorption calculation. The supernova is divided into approximately 500 radial zones and 100 angular zones. The number of zones are picked so that the “optically thin” nature of this treatment (as seen eqn. A.1) is preserved. Given the abundances and time since explosion, the sources are calculated at each point and the emitted γ-rays are followed throughout the atmosphere in accordance with the above equations on equally spaced lines in μ.

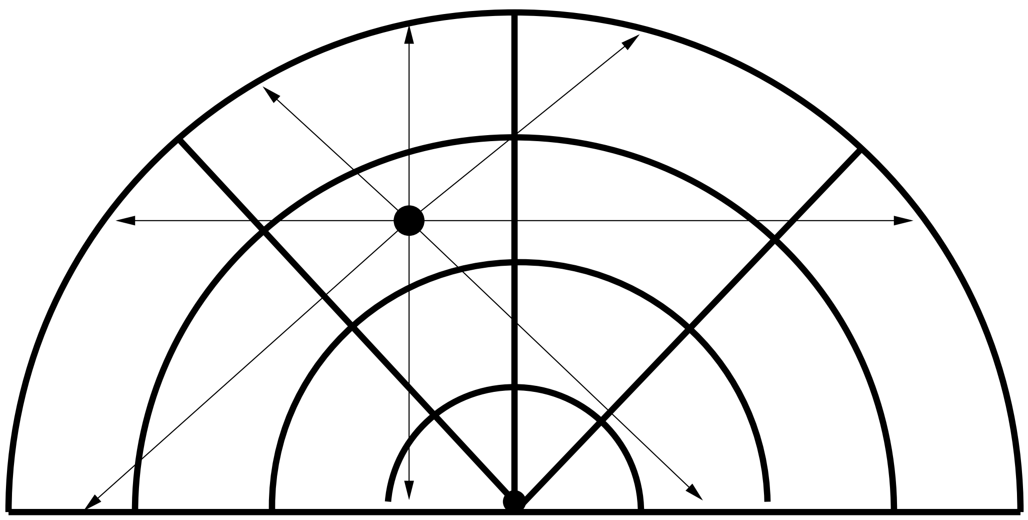

Figure A.1: Geometric lay-out for the γ-ray deposition calculation.

As a test of this method we can compare the results of the above treatment to the semi-analytic one found in Sutherland & Wheeler (1984). Here it was shown that for an atmosphere in which all the radioactive sources are located within a spherical volume $r < r_c$ then:

$$d(a) = \frac{1}{2}\int_{-1}^{\mu_{max}} d\mu[e^{-\tau_{min}} - e^{-\tau_{max}}] \tag{A.5}$$

Here, $\mu = cos(\theta)$ and tau_{min} and tau_{max} are the total optical depths to the near and far side of the radioactive core along the ray specified by $theta$ as seen in Fig. A.2. In Fig. A.3 we see how well our calculation compares to the semi-analytic result derived in Equation A.5. Note that the only discrepancy occurs in the first zone for the late time model when the analytic and numerical results differ by $\approx 5\%$.

Finally, we present the results of our deposition calculations for the three hydrodynamic explosion models for SNe Ia considered in this thesis. In Fig. A.4 we see a plot of the deposition function versus the mass fraction for models W7, WW2 and LA4 all at 20 days after explosion. Note the large differences between the C/O deflagration model W7 and the helium-igniter models WW2 and LA4.

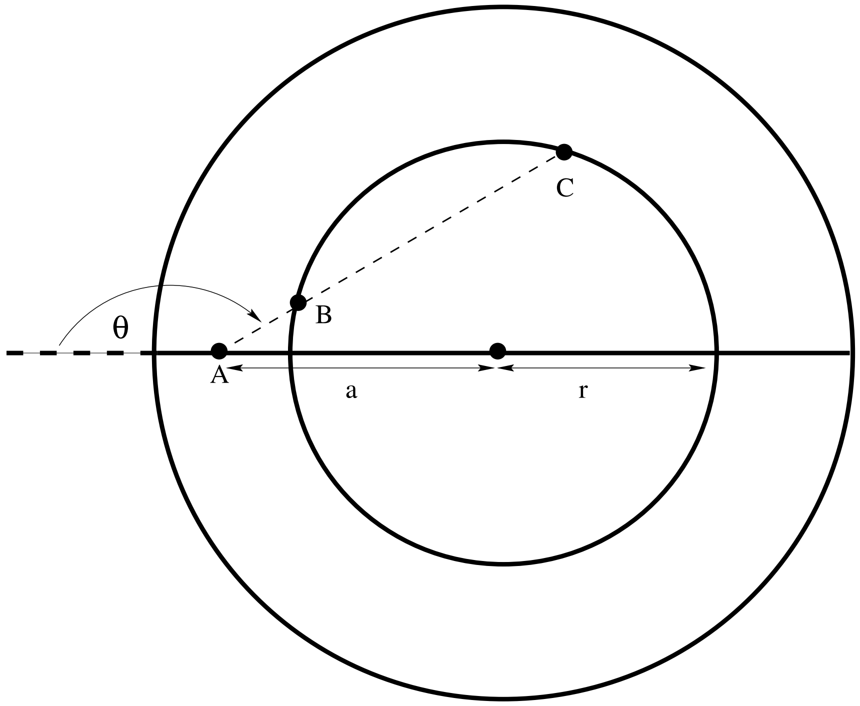

Figure A.2: The deposition is being calculated at point A (at a distance a from the center) and r is the radius of the radioactive core.

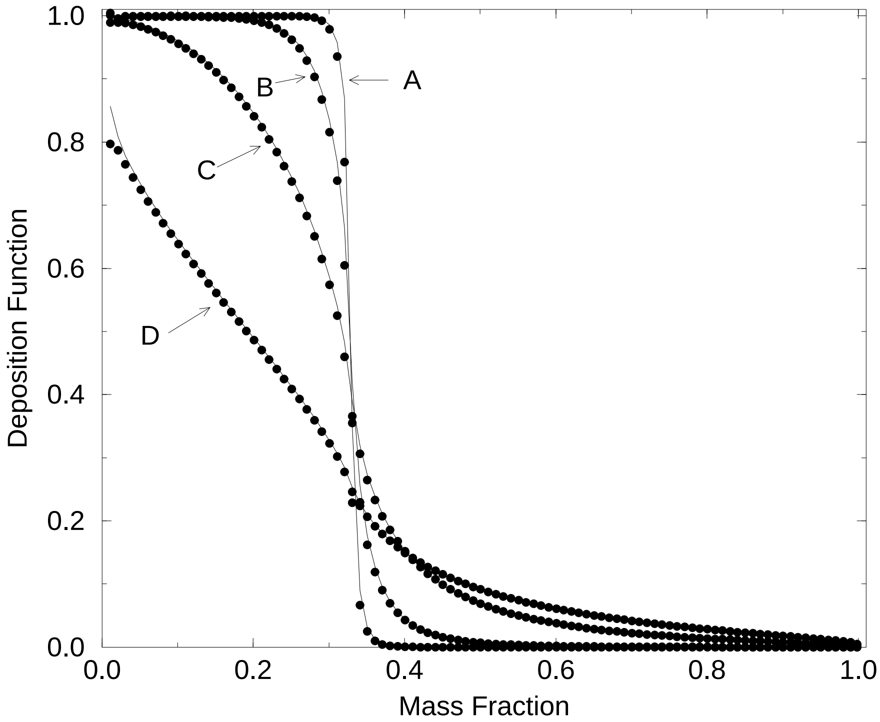

Figure A.3: A Graph of the semi-analytic deposition function (lines) vs. the numerical absorption calculation (filled circles). Curves A, B, C and D represent $t_6 = 0.5$, 1, 2 and 4 (in units of 10^6 s) respectively.

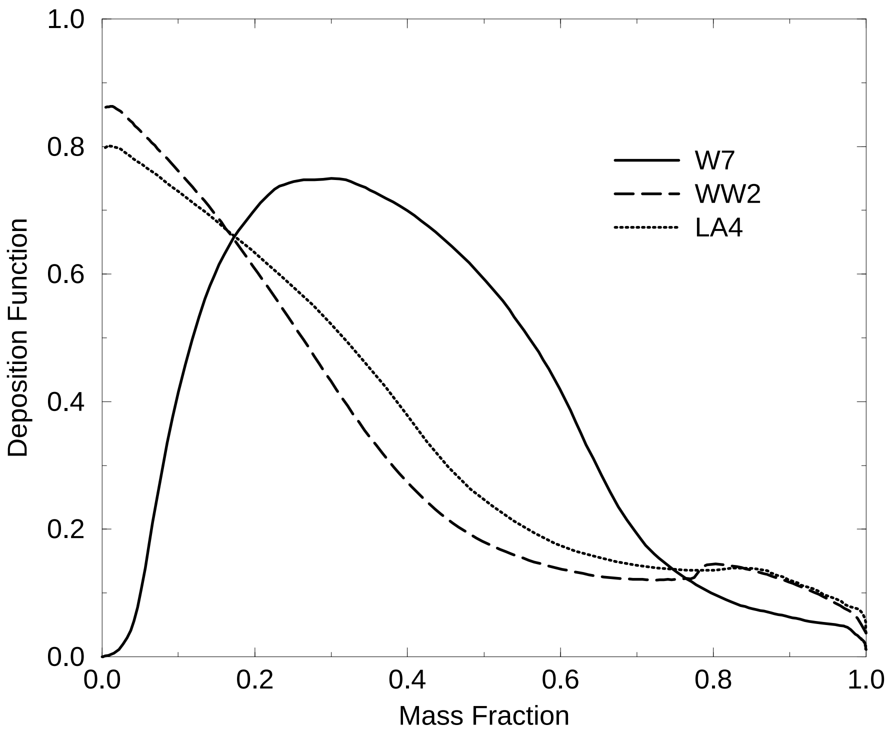

Figure A.4: The 20 day deposition functions of models W7, WW2 and LA4.

Appendix B

α — The Thermalization Parameter

In addition to the NLTE lines, the models include, self consistently, line blanketing of the metal lines selected from the latest atomic and ionic line list of Kurucz. The source function for these lines can be written as follows (Mihalas, 1978):

$$S_l = \frac{\int \Phi_\nu J_\nu d\nu + \epsilon' B_\nu(T_e) + \eta B^*(T_r)}{1 + \epsilon' + \eta} \tag{B.1}$$

The first term of the numerator is represents the scattering reservoir, the second the thermal source (photons created by collisional excitation followed by radiative de-excitation) and the third term are those photons created by recombination from the continuum to the upper level followed by a radiative de-excitation. In the denominator, ϵ represents those photons destroyed by collisional de-excitation and η is a sink term proportional to the total rate of ionization from the upper state times the fractional recombination rate to the lower level. $B_\nu(T_e)$ is the Planck function based on the local electron temperature, T_e, and $B^*(T_r)$ resembles the Planck function for a characteristic radiation temperature, T_r.

The following is a derivation of ϵ based on the work of Castor (1970).

$$\epsilon = \frac{\epsilon'}{1+\epsilon'} \tag{B.2}$$

$$\epsilon' = \frac{C_{ul}(1-exp(-u))}{A_{ul}} \tag{B.3}$$

Where $u = \frac{h\nu}{kT}$ and $E_o = h\nu$.

with $C_{ul} = (\frac{n_l}{n_u})^* C_{lu}$ and $\frac{g_l}{g_u} = (\frac{n_l}{n_u})^* exp(-u)$

Given

$$C_{lu} = C_o n_e T^{\frac{1}{2}} \left[14.5 f_{lu} \left(\frac{I_H}{E_o} \right)^2 \right] uexp(-u)\Gamma(u) \tag{B.4}$$

and

$$A_{ul} = \frac{64\pi^4\nu^3}{3hc^3 g_u} \frac{g_l f_{lu} 3he^2}{8\pi^2 m_e \nu} \tag{B.5}$$

with

$$C_o = \pi a_o^2 (\frac{8k}{m_e \pi})^{\frac{1}{2}} \tag{B.6}$$

then ϵ' can be rewritten as:

$$\epsilon' = \frac{C_o [14.5(\frac{I_H}{E_o})^2] u\Gamma(u)(1-exp(-u)) m_e c^3 n_e T^{\frac{1}{2}}}{8\pi^2\nu^2 e^2} \tag{B.7}$$

$$\epsilon' = \frac{a_o^2 [14.5 I_H^2] m_e^{\frac{1}{2}} c^3}{\sqrt{8}\pi^{\frac{3}{2}} e^2 h k^{\frac{1}{2}}} \frac{n_e}{T^{\frac{1}{2}}\nu^3} \Gamma(u)(1-exp(-u)) \tag{B.8}$$

$$\epsilon' = 20 \frac{\lambda^3 n_e}{T^{\frac{1}{2}}} \Gamma(u)(1-exp(-u)) \tag{B.9}$$

$$\epsilon' = 20\frac{\lambda_\mu^3 n_{e_{10}}}{T_5^{\frac{1}{2}}}\Gamma(u)(1 - exp(-u)) \tag{B.10}$$

$\Gamma(u)$ is defined as follows $\Gamma(u) = max[\bar{g}, 0.276exp(u)E_1(u)]$, with $\bar{g} = 0.2$ for $n'l' \rightarrow nl$ and $\bar{g} = 0.7$ for $nl' \rightarrow nl$. In Fig. B.1 we can see a plot of ϵ as a function of optical depth and velocity. Note that ϵ is low over much of the atmosphere except at depth.

The the third term in the numerator, η, is defined as follows:

$$\eta = \frac{(R_{u\kappa} + C_{u\kappa})n_l^*(R_{\kappa l} + C_{l\kappa}) - g_l(R_{l\kappa} + C_{l\kappa})n_u^*(R_{\kappa u} + C_{u\kappa})/g_u}{A_{ul}[n_l^*(R_{\kappa l} + C_{l\kappa}) + n_u^*(R_{\kappa u} + C_{u\kappa})]} \tag{B.11}$$

with

$$B^* = \left(\frac{2h\nu^3}{c^2}\right)\left\{\left(\frac{n_l^* g_u}{n_u^* g_l}\right)\left[\frac{(R_{u\kappa} + C_{u\kappa})(R_{\kappa l} + C_{l\kappa})}{(R_{l\kappa} + C_{l\kappa})(R_{\kappa u} + C_{u\kappa})}\right] - 1\right\}^{-1} \tag{B.12}$$

It's clear from observation of eqn. B.12 that B^* is very similar to the Planck function and can be thought of as having a characteristic radiation temperature of T_r which is set by the photoionization and recombination rates. At depth, $R_{l\kappa} \rightarrow R_{\kappa l}$ and $R_{u\kappa} \rightarrow R_{\kappa u}$ so that $B^* \rightarrow B_\nu(T_e)$. However, in optically thin regions the results are quite different. In a SN Ia's outer atmosphere collisions are near negligible and $R_{l\kappa} > R_{\kappa l}$ and $R_{\kappa u} > R_{u\kappa}$. This is the case of a relatively *cool* medium being irradiated by a *hot* radiation field. Therefore, $B^* > B_\nu$ and S_l will be larger than the S_l determined by only the coupling to the thermal pool. Thus η increases the overall 'thermalization' in the atmosphere. For simplicity and computational expediency, we now rewrite eqn. B.1 as:

$$S_l \approx (1 - \alpha)\int \Phi_\nu J_\nu d\nu + \alpha B_\nu(T) \tag{B.13}$$

$$\text{assuming} \quad B^* \approx B_\nu(T) \tag{B.14}$$

where α now represents both the effects of ϵ and η. Since the calculation of α would require a full NLTE treatment of all lines and continua, which is beyond our present ability to acquire atomic data, we adopt an average value for α for all the metal lines in LTE. Due to the velocity gradients in SNe Ia the shape of the lines does not depend heavily on α, however, α does have an effect on the overall color of the spectrum. Therefore, it is necessary to treat α as a parameter to fit in concert with the temperature.

In Fig. B.2 and Fig. B.3 we examine the effect of α on the synthetic spectra for models which are purely in LTE. Of importance to us is how much the color and absolute magnitude are effected by varying α, since increasing α causes more thermalization and thus reddens the spectrum. In Fig. B.2 we see a very good fit to the spectrum of SN 1992A at 5 days after maximum light using an $\alpha = 0.1$. Fig. B.3 shows two unacceptable fits to the spectrum with $\alpha = 0.3$ and $\alpha = 0.01$. In Table B.1 we display the results of this parameterized study. Of particular note is the fact that the range of acceptable fits spans only $\pm$ 0.05 in color and $\pm$ 0.17 in M_V. These can be thought of as limits to our accuracy in determining the characteristics of a particular model due to the effects of α.

Model	α	T_{eff}	$B - V$	$M_V - M_V(361)$	*Grade*
355	0.01	8000	-0.08	0.65	D
353	0.05	8500	0.14	0.19	B
361	0.10	8900	0.19	0.00	A
321	0.20	9250	0.25	-0.14	B
341	0.30	9400	0.30	-0.21	D

Table B.1: The color and magnitude differences for a set of models with different values of α.

Figure B.4 compares the spectra for $\alpha = (10^{-4}, 0.05, 0.1, 1.0)$ for the W7 model considered in Chapter 4. This is a model which has almost all of the major species treated in NLTE. The UV (where most lines are treated in NLTE) is rather insensitive to the choice of α; however, in the optical, redward of 5000 Å there is a strong dependence on α. Based on these results and the LTE comparisons we choose $\alpha = 0.05 - 0.1$ as our range for SNe Ia.

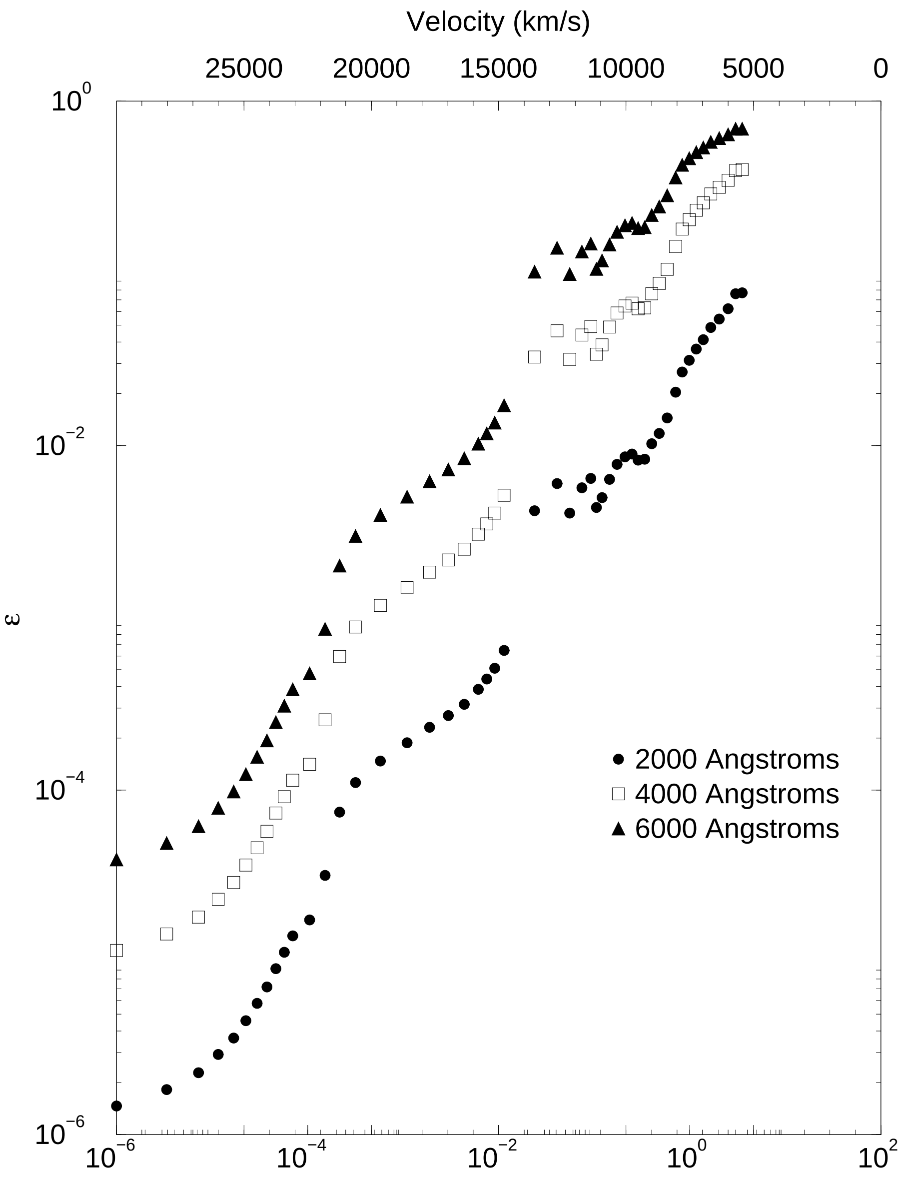

Figure B.1: ϵ as a function of wavelength for W7 at 20 days after explosion.

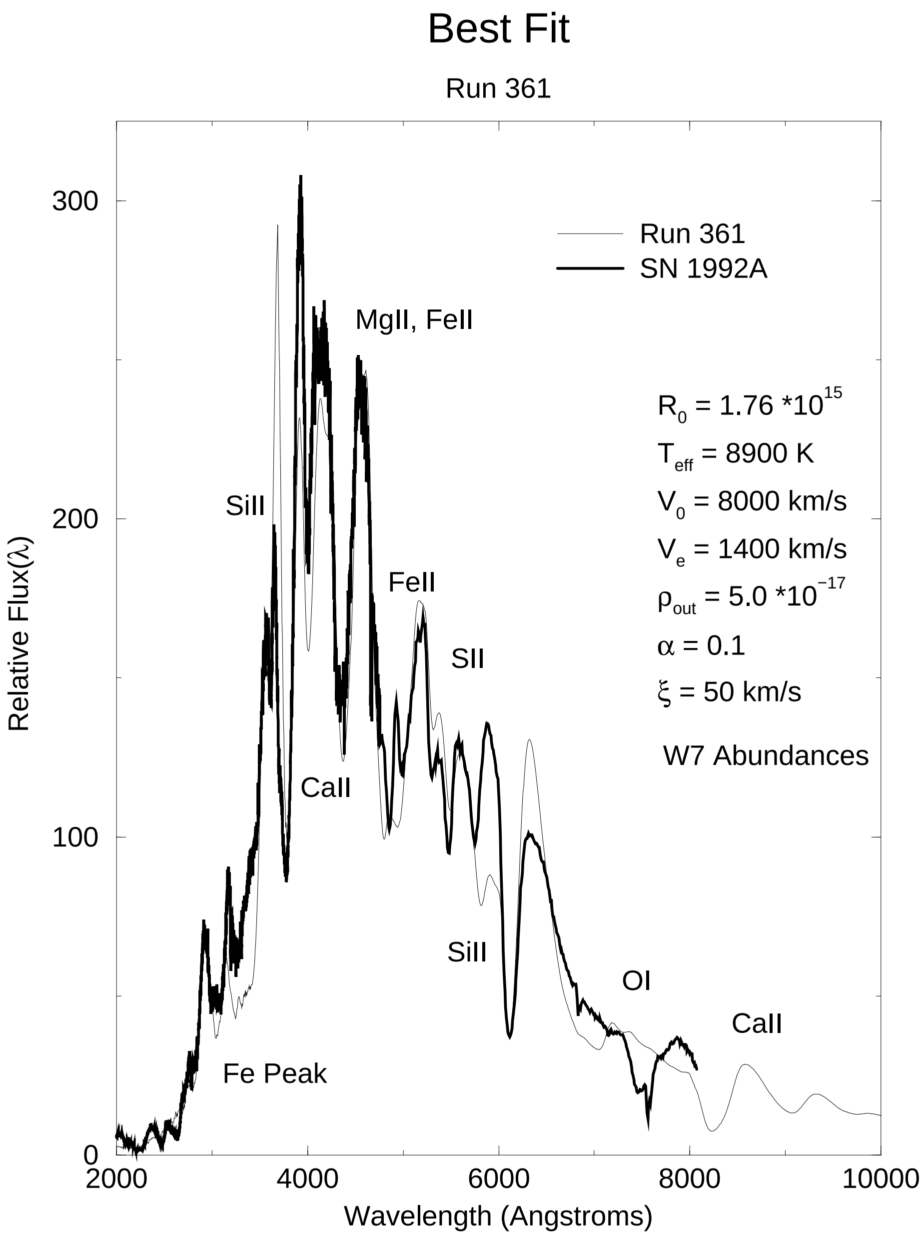

Figure B.2: A good fit to the spectrum of SN 1992A for $\alpha = 0.1$.

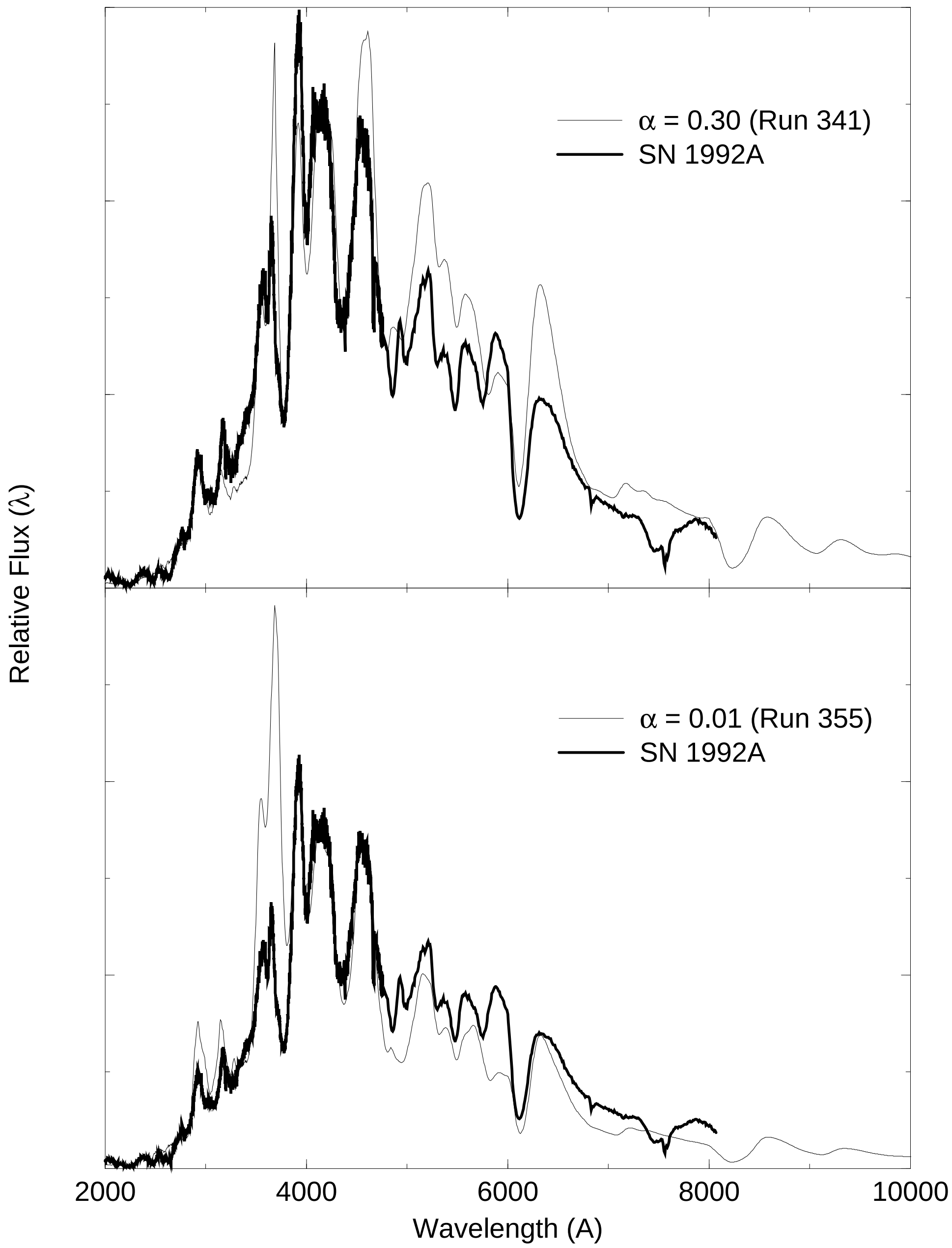

Figure B.3: Unacceptable fits to the spectrum of SN 1992A for $\alpha = 0.01$ and 0.3.

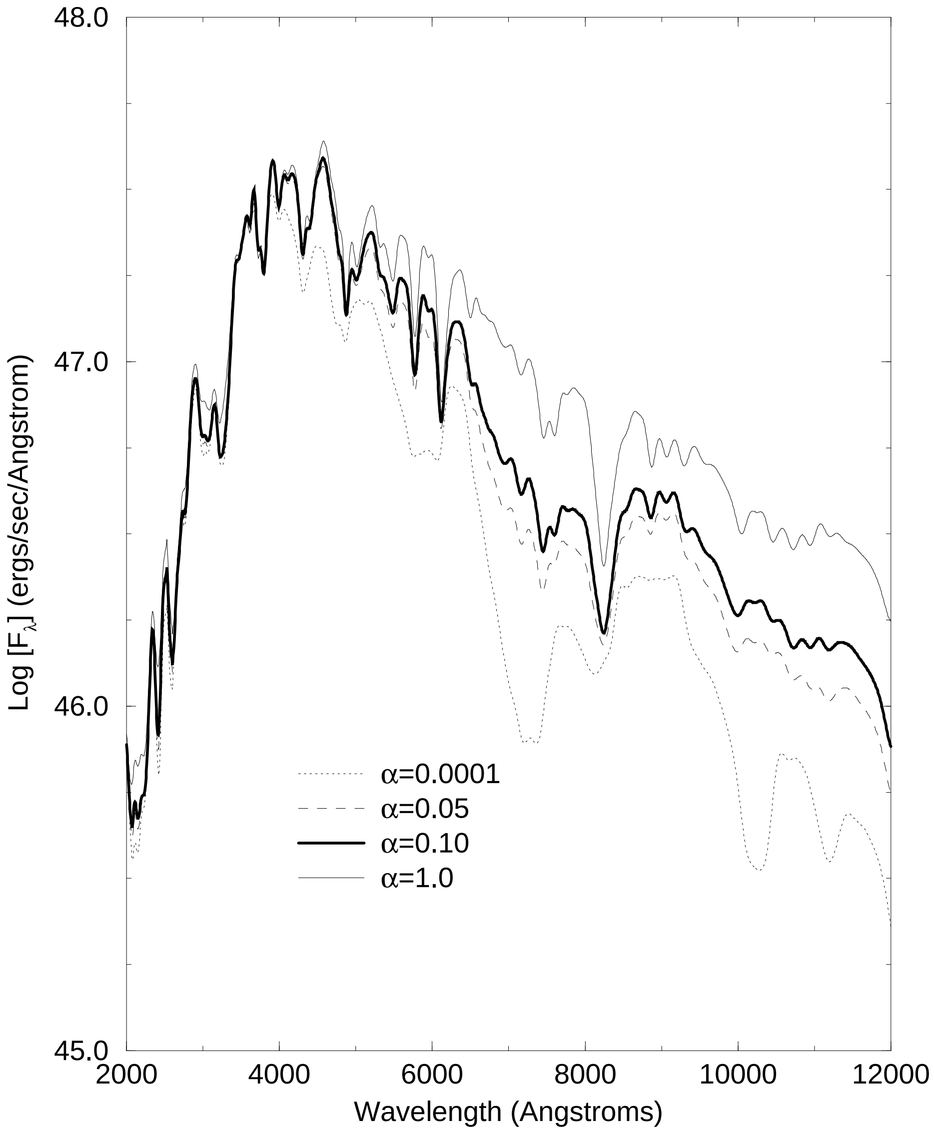

Figure B.4: The synthetic spectrum for the W7 model at 23 d past explosion for four choices of α. The model with $\alpha = 0.10$ is in radiative equilibrium and the temperature structure has been held fixed at that structure for all the models displayed.